β-γ spectroscopy of neutron-rich nucleus ^{195}Os

Md. Murad Ahmed

February 2019

β-γ spectroscopy of neutron-rich nucleus ^{195}Os

Md. Murad Ahmed
Doctoral Program in Physics

Submitted to the Graduate School of
Pure and Applied Sciences
in Partial Fulfilment of the Requirements
for the Degree of Doctor of Philosophy in
Science

at the
University of Tsukuba

Contents

List of Figures

List of tables

Abstract

One of the fundamental problems of astrophysics is an origin of chemical elements. Observed abundance of the elements in the universe is a fingerprint to trace back pathways of nucleosyntheses in terms of astrophysical parameters. A reliable description underlying astrophysical scenarios depends crucially on the knowledge of the nuclear properties. Approximately a half of the nuclei in nature beyond the iron is considered to be synthesized in the rapid neutron capture process (r-process). The astrophysical environment of the r-process is characterized by a neutron density higher than 10^{20} cm^{-3} and a temperature higher than 10^{9} K. The r-process proceeds through a region of very neutron-rich nuclei under such explosive environment. The 3rd peak at the mass number of 195 on the solar r-abundance distribution is considered to be originated from waiting point nuclei with neutron number (N) of 126 on the r-process path. Understanding of the 3rd peak formation is a key issue to elucidate the astrophysical environment of the r-process and to reveal its astronomical site. For the sake, nuclear properties of the waiting point nuclei such as β-decay half-lives, neutron separation energies and β-delayed neutron emission probabilities are necessary. However, the waiting point nuclei for the 3rd peak are too far from the β-stability line to experimentally access them, remaining the stellar environment for the 3rd peak formation still unknown. In the current r-process calculations, nuclear properties of waiting point nuclei for the 3rd peak are based on the theoretical predictions. The region of neutron-rich nuclei with $N = 126$ is, particularly, predicted as a competitive region of the first-forbidden (FF) and allowed Gamow-Teller β-decays. Such competition makes it difficult to predict lifetimes of the waiting point nuclei, giving large deviations of the input parameters for the r-process calculations from model to model.

The experimental investigation of nuclear structures for the neutron-rich nuclei around $N = 126$ is quite important. It would provide crucial inputs to a theoretical model to improve its predictability for the β-decay half-lives of the waiting point nuclei at $N = 126$. In this work, we have performed the β-γ spectroscopy of ^{195}Os as one of such nuclei around $N = 126$, whose β-decay schemes are unknown. The radioactive isotopes around $N = 126$ were produced by the multi-nucleon transfer reactions of ^{136}Xe beams and ^{198}Pt target. The isotope of interest is separated and extracted using the KEK isotope separation system (KISS), which is an argon-gas-cell based laser ion source with a mass separator. Those extracted isotopes are implanted into an aluminized Mylar tape,

which is surrounded by the Multi-Segmented Proportional Gas Counter (MSPGC) and four Super Clover High-Purity Germanium (SC-HPGe) detectors for measurements of the β-γ spectroscopy. Twenty-eight γ-ray peaks were observed in coincidence with β-rays, internal conversion electrons and X-rays detected by the MSPGC.

Twenty-two of them were identified as β-delayed γ-rays of the ^{195}Os ground state, where the energies of twenty γ-ray peaks agree with the literature values of observed transitions in ^{194}Ir(n, γ) reactions and two γ-ray peaks were newly found. Two γ-ray peaks were identified as β-delayed γ-rays of the ^{195}Ir ground state. Four γ-ray peaks were associated with the half-life of 47(3) s, which is shorter than the half-life of the ^{195}Os ground state. The cascade transitions among those four γ-rays and the characteristic K X-rays of osmium were found in all γ-γ coincidence spectra, indicating that those transitions belong to a previously unknown isomeric state of ^{195}Os.

The β-decay branching ratios of the ^{195}Os ground state were deduced from the β-γ spectroscopy data. The range of obtained log *ft* values is from 5.98(4) to 7.63(26), indicating all β-transitions are the first forbidden ones. Systematically assumed spin-parity of ^{195}Os ground state, $3/2^-$, is consistent with an expected one based on the observed log *ft* values and spin-parities of the β-decay final states. The β-decay half-life of the ^{195}Os ground state was evaluated to be 6.5(4) minutes, which agrees well to the previously known value 6.5(11) minutes. The experimental half-lives of the osmium isotopes including this work are compared with several theoretical predictions. It is found that the systematic trend of the half-lives of the osmium isotopes is not reproduced by any single model. It encourages the improvement of the treatment for FF transitions in any model to reproduce the experimental trend of the Os ground state lifetimes.

1 Introduction

1.1 Astrophysical nucleosynthesis

One of the fundamental problems of astrophysics is an origin of chemical elements. It has been known that the light elements such as hydrogen, helium and lithium were created in three minutes after the Big Bang. Two heavier elements, beryllium and boron are synthesized in interstellar space by collisions between cosmic rays and dust nuclei [1]. The other elements in nature are formed by nuclear reactions inside stars. Observed abundance of the elements in the universe is a fingerprint to trace back pathways of nucleosyntheses in terms of astrophysical parameters. A reliable description of underlying astrophysical scenarios depends crucially on the knowledge of nuclear properties. Exothermic nuclear fusion reactions inside the stellar cores release sufficient energy that powers stars and protects them against gravitational contraction. As the binding energy per nucleon is the maximum at iron, fusion reactions after iron become endothermic. The Coulomb barriers with large atomic numbers suppress all nuclear reactions induced by charged particles at the stellar temperatures. On the other hand, neutron-capture processes are free from the Coulomb barrier. Therefore, the elements beyond iron are mainly formed in nuclear neutron-capture processes.

There are two main neutron-capture processes, a slow neutron-capture process (s-process) and a rapid neutron-capture process (r-process).

- s-process: A neutron-capture rate is much slower than β-decay rate. This process goes more or less along the line of the β-stability until ^{208}Pb and ^{209}Bi. Because any further capture of neutrons leads immediately to α-decay, it does not go beyond ^{209}Bi. The s-process is believed to occur in the Asymptotic Giant Branch (AGB) stars [2].

- r-process: A very rapid neutron-capture process can occur under an explosive condition of a temperature higher than 10^9 K and a neutron density higher than 10^{20} cm^{-3} [3]. The reaction path involving neutron captures, photo-disintegrations and β-decays moves up along a line somewhere between the β-stability and the neutron drip line, because a neutron capture rate is very high compared with β-decay rate. The r-process requires a synthesis time of the order of seconds to form heavy elements such as thorium and uranium.

1.2 r-process nucleosynthesis

The r-process is considered to be responsible for the synthesis of approximately a half of isotopes in nature beyond iron [1, 4]. The astrophysical environment of the r-process is characterized by a neutron density higher than 10^{20} cm^{-3} and a temperature higher than 10^9 K. The most probable candidates of the astronomical sites for the r-process are core collapse supernovae and neutron star mergers. A supernova is a stellar explosion which is considered to result in the creation of a proto-neutron star, ejecting star's outer layers into space as an enormous cloud of gas and dust. The high neutron density in the explosive environment produces more and more neutron-rich nuclei through successive neutron capture, (n, γ), by the seed nuclei. The high temperature on the other hand generates a high flux of photon that can disintegrate these neutron-rich nuclei via (γ, n) reactions. An equilibration of the reaction rates between the neutron capture and the photo-disintegration results in a certain pattern of the isotopic distribution of the corresponding elements, waiting until a β^--decay occurs. The β^--decay opens a path to the next region of heavier elements. Particularly, due to the relatively small neutron separation energies (S_n) such as a few MeV [5, 6] in nuclei with neutron numbers of $N_{magic} + 1$, where N_{magic} is a neutron magic number (50, 82 and 126), the neutron capture process easily equilibrates to the photo-disintegration (waiting points). The red boxes in FIG. 1.1 indicate the expected r-process path. The β^--decay lifetimes of the waiting point nuclei govern a process time in the region of waiting point nuclei and finally determine a dynamical time scale of the r-process (duration-time), after which the created neutron-rich isotopes (r-process progenitors) decay back to the β-stability line to yield the observed solar r-abundance distribution. The peaks found at the mass numbers of 80, 130 and 195 in the distribution are considered to correspond to the waiting regions characterized by neutron magic numbers of 50, 82 and 126, respectively.

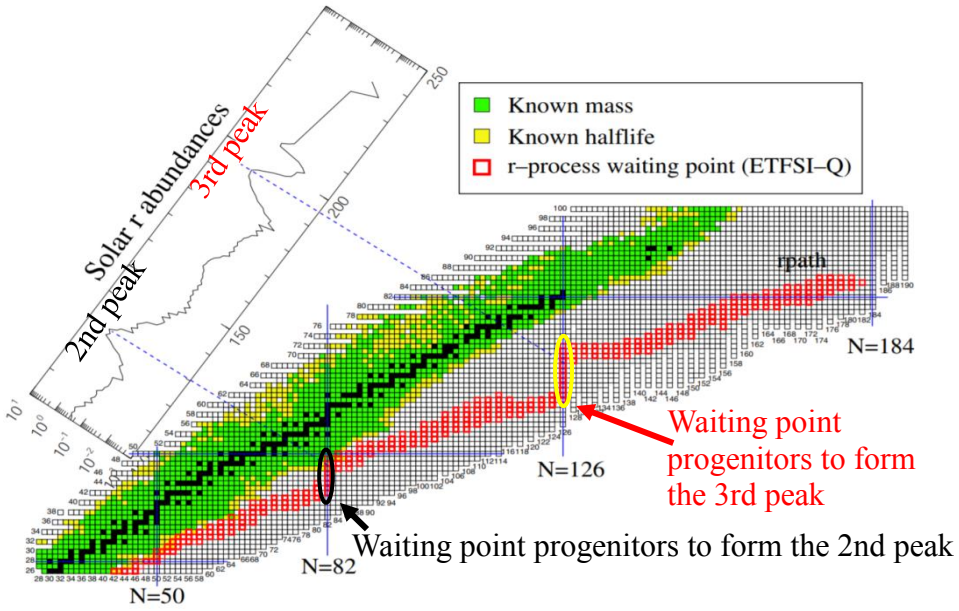

FIG.1.1 Expected r-process path (red boxes) plotted in the nuclear chart. After β-decays to the stable isotopes (filled black boxes), the r-process progenitors produce the observed solar r-abundance distribution. The r-process path runs through the neutron-rich nuclei having unknown masses and lifetimes. In this simulation, mass formula based on the Extended Tomas Fermi plus Strutinsky Integral (ETFSI) model and special treatment of shell quenching was adopted [5, 7].

1.2.1 r-process waiting point nuclei for the 2nd peak

The first experimental data of the lifetime for the waiting point nucleus ^{130}Cd, the progenitor nucleus of ^{130}Te, was reported by Kratz *et al.* [3]. Using the experimental result together with improved shell-model predictions of β-decay properties as shown in FIG. 1.2, they have demonstrated that the "waiting point" nuclei can be directly related to the observed r-abundances and that a constraint on the stellar condition between the temperature (T) and the neutron number density (n_n) can be evaluated. This kind of analysis is called "waiting point" analysis.

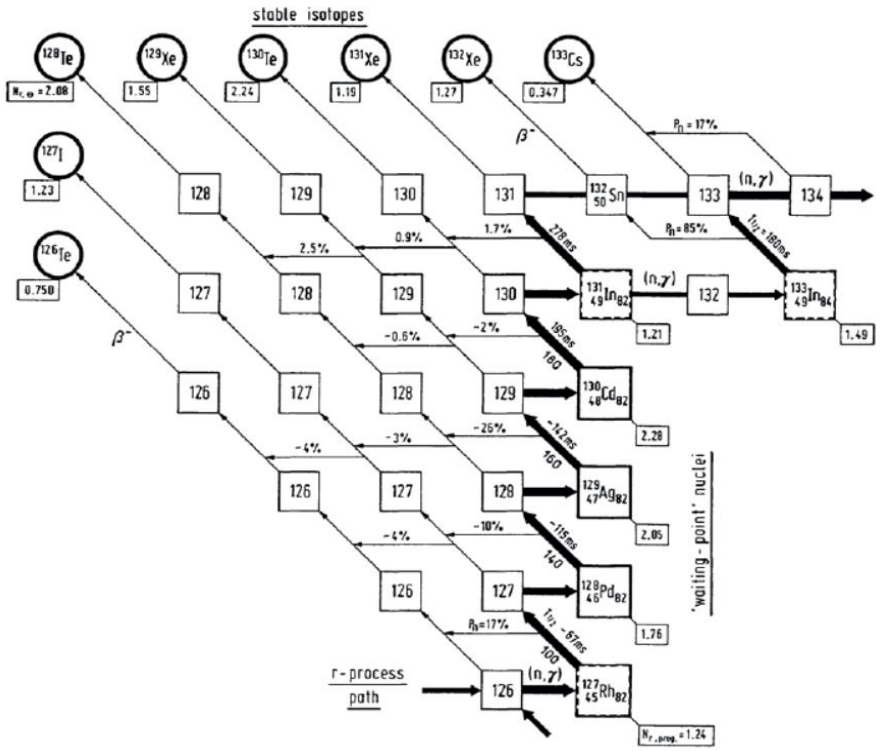

FIG.1.2 Schematic view of the r-abundance and the β-decay properties of nuclei in the "waiting point" region of $A \sim 130$ with $N = 82$. The β-decay half-lives ($T_{1/2}$) and branching ratios for β-delayed neutron emission (P_n) are experimental values or predicted values of the random phase approximation (RPA) model [3].

1.2.2 r-process waiting point nuclei for the 3rd peak

To understand the 3rd peak formation, the ground state properties of the waiting point nuclei such as β-decay half-lives, neutron separation energies and β-delayed neutron emission probabilities are necessary to constrain the temperature, the neutron density and the timescale of the r-process. However, the waiting point nuclei for the 3rd peak such as ^{195}Tm and the break through pairs, ^{196}Yb and ^{198}Yb, are too far from the β-stability line to experimentally access them.

In the current r-process calculations, nuclear properties of waiting point nuclei for the 3rd peak are based on theoretical predictions with large deviations in those input values from model to model. This situation cannot be avoided for such extremely neutron-rich nuclei. The experimental investigation of nuclear properties of the neutron-rich nuclei around $N = 126$ is important for selection and improvement of reliable theoretical models.

1.3 β-decays of neutron-rich nuclei near the 3rd waiting region

In the case of the 2nd peak, allowed Gamow-Teller (GT) transitions are dominant decay channels for all nuclei with the shell closure of N = 82 on the r-process path [9]. However, the region of neutron-rich nuclei with N = 126 is predicted as a competitive region of the first-forbidden (FF) and allowed GT β-decays. Such competition makes it difficult to predict lifetimes of the waiting point nuclei concerning the 3rd peak. FIG. 1.3 shows a schematic view of single-particle states for the neutron-rich nuclei around N = 126. The black (brown) and gray (blue) horizontal lines indicate the odd- and even-parity states, respectively, for neutron (proton) orbits. The red and blue arrows indicate possible GT and FF transitions, respectively. According to this simple picture, FF transitions seem to dominate to GT transitions.

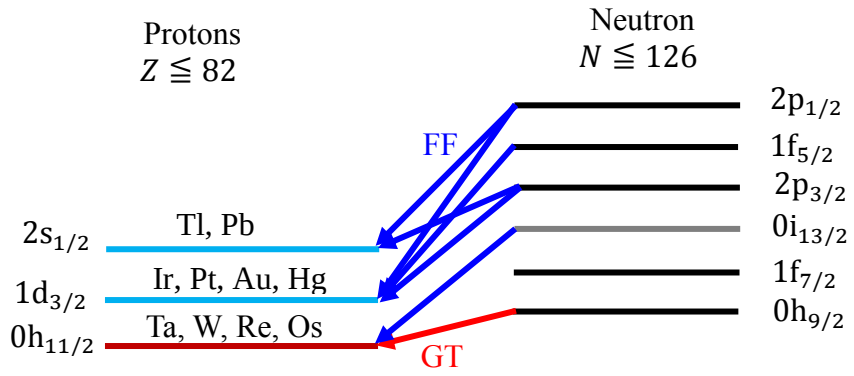

FIG. 1.3 Schematic view of single particle states in the region of $65 \leq Z \leq 82$ and $83 \leq N \leq 126$.

FIG. 1.4 shows the half-life systematics for the N = 126 nuclei by different theoretical model predictions including some experimental data. The KTUY model [10], finite-range droplet model (FRDM) [11], shell model (SM) [12], the generalized energy-density functional method with continuum quasi-particle random phase approximation (DF3) model [9, 13] are cited. The SM results taking with and without contributions of FF transitions are shown by open square and hexagonal markers, respectively, indicating shorter half-lives for GT + FF compared with the pure GT transitions. All other theoretical model calculations include both the GT and the FF transitions. The predicted half-lives are deviated from a factor of three to more than one order of magnitude among different theoretical models. Such deviation of predicted lifetimes strongly affect the final r-abundances [15]. The experimental data of Pt, Au and Hg, which are indicated by red closed circles in FIG. 1.4, are well reproduced by the

DF3 model. However, there are no experimental data for the nuclei with $Z \leq 77$. The experimental investigation of lifetimes for the nuclei with $Z \approx 70 - 80$ and $N \approx 114 - 126$ is quite important to study nuclear structure of neutron-rich nuclei toward to $N = 126$ neutron-rich nuclei.

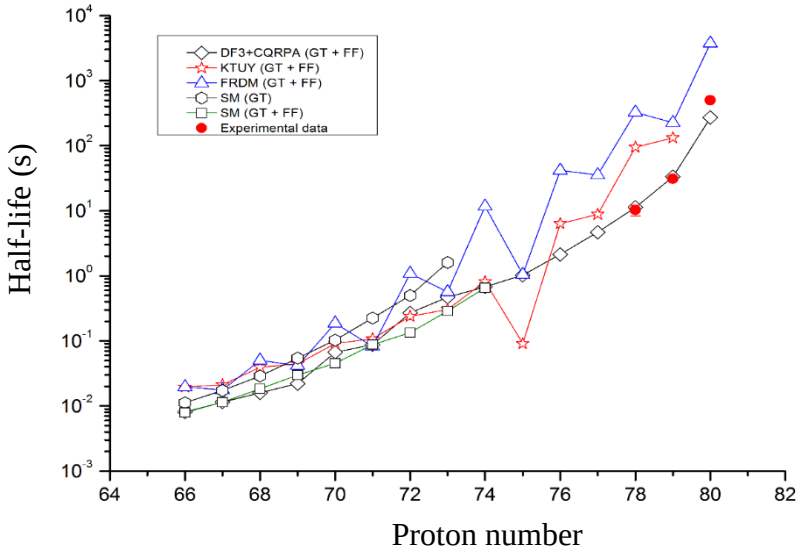

FIG. 1.4 Predicted half-lives of $N = 126$ nuclei by various theoretical models. Experimental results of Pt ($Z = 78$), Au ($Z = 79$) and Hg ($Z = 80$) are indicated by red closed circles [14].

1.4 Isotope to be studied: ^{195}Os

The experimental spectroscopic information that includes β-delayed γ-rays, β-decay branching ratios and isomeric states of ^{195}Os can be used to study nuclear structure of neutron-rich nuclei around $N = 126$ for improvement of the theoretical prediction of their β-decay half-lives. FIG. 1.5 shows the neutron-rich nuclei around the neutron magic number $N = 126$. The waiting point nuclei for the 3rd peak such as ^{195}Tm and ^{196}Yb are too far from the β-stability line. Boxes file in black indicate the stable nuclei. The β-decay flows from the waiting point nuclei are indicated by red arrows. Dotted blue boxes indicate isotopes whose β-decay properties were studied so far. Red square box indicates the nucleus, ^{195}Os, which is studied in the present work. It is clear that decay properties of ^{195}Os are also important to investigate decay flow estimation from progenitor nuclei of $A = 195$, ^{195}Tm.

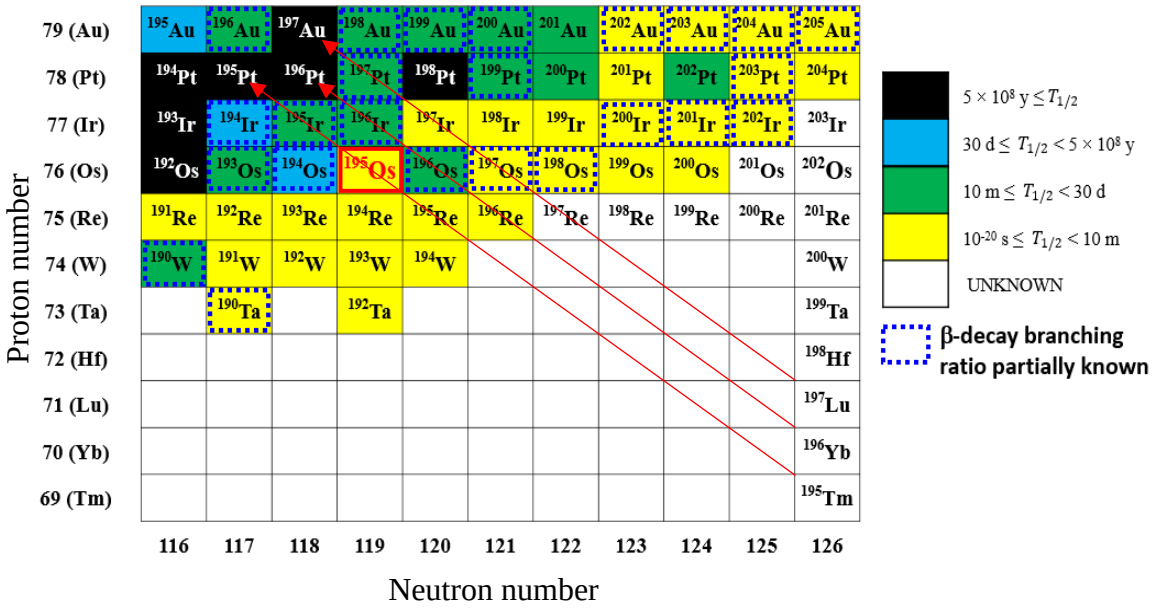

FIG. 1.5 Part of the nuclear chart around the neutron magic number $N = 126$. Boxes filled in black indicate the stable nuclei. The β-decay flows from the waiting point nuclei are indicated by red arrows. Dotted blue boxes indicate the isotopes whose β-decay properties were studied so far.

1.4.1 Previous studies

Rey and Baro firstly measured the half-life of ^{195}Os as 6.5 minutes using the reactions of ^{198}Pt(n,α)^{195}Os [16]. M. Birch *et al.* reanalyzed their data and deduced 6.5(11) minutes for the half-life of the ^{195}Os ground state [28]. M. W. Reed *et al.* assumed the spin and the parity of the ^{195}Os ground state as $3/2^-$ [20]. Recently two isomeric states with half-lives of 26(4) ns [17, 18, 19] and > 9 minutes [20] were reported from decay spectroscopy at GSI fragment separator (FRS) and time-of-flight measurements at GSI experimental storage ring (ESR), respectively. It is noted that ^{195}Os isotopes were produced through high-energy projectile-like fragmentation reactions of ^{209}Pb-beams for both cases.

1.5 Outline of the present work

KEK isotope separation system (KISS) is an experimental device specialized for the precise nuclear spectroscopy of neutron-rich nuclei produced by the multi-nucleon transfer (MNT) reactions. In this work, element-selected and mass-separated nuclei of ^{195}Os, which were produced by MNT reactions of

^{136}Xe and ^{198}Pt, were transported to and were measured at the KISS β-γ detector station. Details of the experimental facility and experimental setup will be discussed in Chapter 2. The analysis and results will be focused in Chapter 3. The experimental results are discussed in Chapter 4, including the comparison of experimental half-lives of osmium isotopes with theoretical models. The measurements and the results will be summarized in Chapter 5.

2 Experiment

2.1 Production of neutron-rich nuclei around N = 126

To study the nuclear properties of neutron-rich nuclei around N = 126, it is necessary to produce them artificially via nuclear reactions, because they are unstable and do not exist in nature. There are several approaches to produce them, such as projectile-fragmentation reactions and multi-nucleon transfer (MNT) reactions.

In projectile-fragmentation reactions, the neutron-rich nuclei are produced as projectile-like fragments (PLF's) from the collisions between heavy projectile such as ^{238}U or ^{208}Pb with relativistic energy higher than 100 MeV/nucleon and light target nucleus such as ^{9}Be. The PLF's with nearly the same velocity of the projectile are separated by using a so-called in-flight separator. The mass number (A) and the atomic number (Z) of the fragments are separated by $B\rho - \Delta E - B\rho$ method, where firstly the magnetic rigidity ($B\rho$) is selected by the electromagnetic dipole field for covering a certain mass range and secondly the $B\rho$ is selected to separate a certain momentum range after the energy loss (ΔE) in the energy degrader. The wedge-shaped energy degrader at the dispersive focal plane is used to match momentum dispersions at both sides of upstream and downstream of the degrader. The identification of the fragments is performed by TOF $- B\rho - \Delta E$ method, where the time-of-flight (TOF) and ΔE are measured by charged-particle detectors such as plastic scintillators, multi-sampling ionization chambers and multi-wire proportional chambers, and $B\rho$ is determined by the magnetic dipole field. The high-energy PLF's in the in-flight separator makes it possible to separate Z clearly because all the ions are fully stripped due to the high velocities and the simple relation $A/q \sim A/Z$, where q is the ionic charge, can be used to perform the particle identification in terms of A and Z accurately. This method is applied in the facilities of the BigRIPS at RIKEN and the FRS at GSI [30, 31]. The ^{238}U beam (350 MeV/nucleon) and ^{9}Be target (5 mm in thickness) can be used in the BigRIPS, and the ^{208}Pb beam (1 GeV/nucleon) and ^{9}Be target (14 mm in thickness) can be used in FRS [30, 31]. In the BigRIPS, the charge state distribution of PLF's becomes broad because of the relatively low-velocity fragments, therefore, the particle identification becomes difficult due to the insufficient Z separation [30].

The MNT reaction is an alternative tool for the production of the neutron-rich nuclei around N = 126, where some neutrons and protons are transferred between the beam and the target nuclei (FIG. 2.1 (a)). They are governed by the quasi-elastic and deep-inelastic processes, which compete with each other depending on the reaction properties such as the combination of the colliding

nuclei, the incident projectile energy and the impact parameter. The first precise investigation for the production mechanism of neutron rich-nuclei around $N = 126$ by the MNT reactions with the ^{136}Xe beam (8 MeV/nucleon) and the ^{198}Pt target (1.3 mg/cm^2 in thickness) were performed at GANIL [32]. The production cross sections of the target-like fragments (TLF's) were evaluated from the measured cross sections of the PLF's. In this evaluation, binary processes of the MNT reactions are assumed with the particle evaporation from both fragments. FIG. 2.1 (b) shows a comparison of the production cross sections for $N = 126$ isotones between the MNT reactions and the fragmentation reactions of ^{208}Pb (1 GeV/nucleon) with the Be target [33]. The advantage of using MNT reactions can be seen clearly.

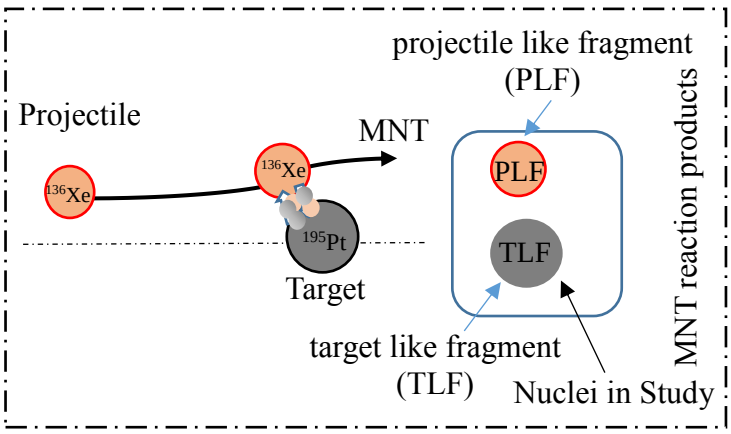

FIG. 2.1 (a) Schematic view of the multi-nucleon transfer reactions.

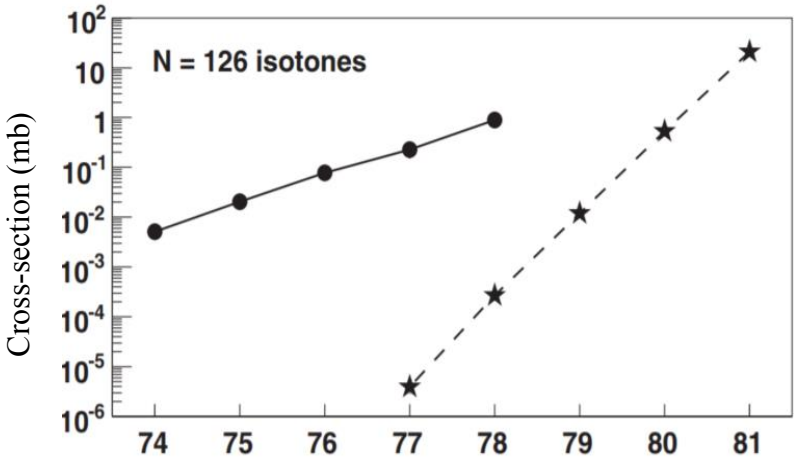

FIG. 2.1 (b) Experimentally deduced cross sections for the production of the $N = 126$ isotones as a function of the atomic number. Filled circles indicate the MNT reactions of ^{136}Xe (8 MeV/nucleon) + ^{198}Pt and filled stars indicate the projectile fragmentation of ^{208}Pb (1 GeV/nucleon) + ^{9}Be. Uncertainties for the expected cross sections are within the symbols. Solid and dashed lines are to guide the eyes (adopted from [32]).

2.1.1 Expected kinematical properties of ^{195}Os

The isotope ^{195}Os is produced by using the MNT reactions of ^{136}Xe + ^{198}Pt. FIG. 2.1.1 (a) shows an estimated distribution of TLF's cross sections via MNT reactions of ^{136}Xe (9.00 MeV/nucleon) + ^{198}Pt that is evaluated by the GRAZING calculations [34, 35, 36]. Various kinds of nuclei are produced by different transfer channels of protons and neutrons. The red box indicates the location of ^{195}Os, which should be separated from other nuclides for the precise β-γ spectroscopy.

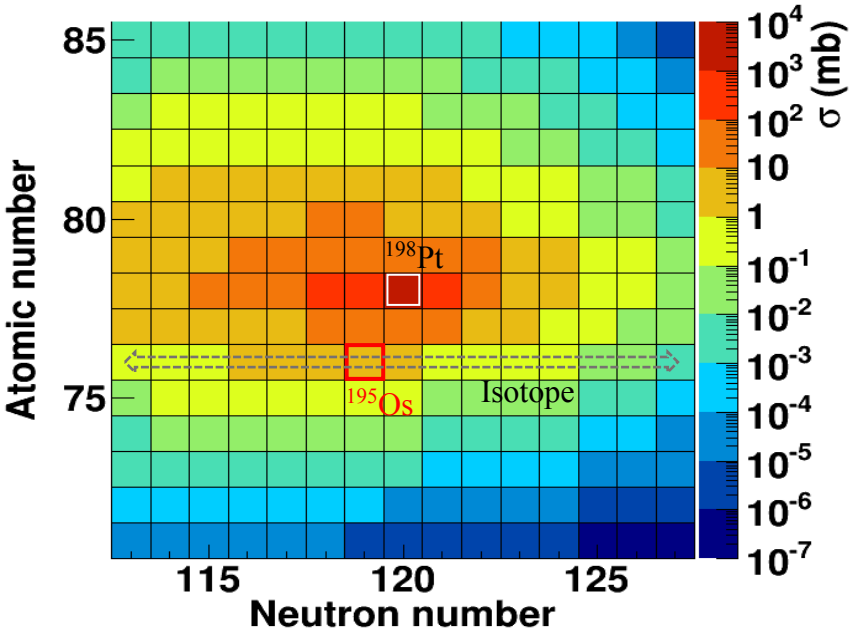

FIG 2.1.1 (a) Distribution of cross sections for TLF's produced via MNT reactions of ^{136}Xe (9.00 MeV/nucleon) + ^{198}Pt evaluated by the GRAZING calculations. The ^{195}Os nucleus is indicated by the red box.

FIG. 2.1.1 (b) and (c) show the expected angular and energy distributions of ^{195}Os ejected from the target in the reactions with the beam energy of 9.4 MeV/nucleon and the target thickness of 12.5 mg/cm^2, respectively. The ^{195}Os nuclei are emitted with large azimuthal angles around 63° ± 5° with respect to the primary beam axis in the laboratory frame due to the reactions around the grazing angles. The kinetic energies of ^{195}Os are distributed from zero to 1.6 MeV/nucleon. The broaden recoil energies are induced by excitation of reaction products and energy losses of ^{195}Os in the target material depending on the reaction positions in the target and the recoil angles. FIG. 2.1.1 (d) shows the correlation between the angles and the kinetic energies of the ejected ^{195}Os

from the target. For efficient measurements of the β-γ spectroscopy, the ^{195}Os nuclei with such energy and angular distributions should be collected effectively.

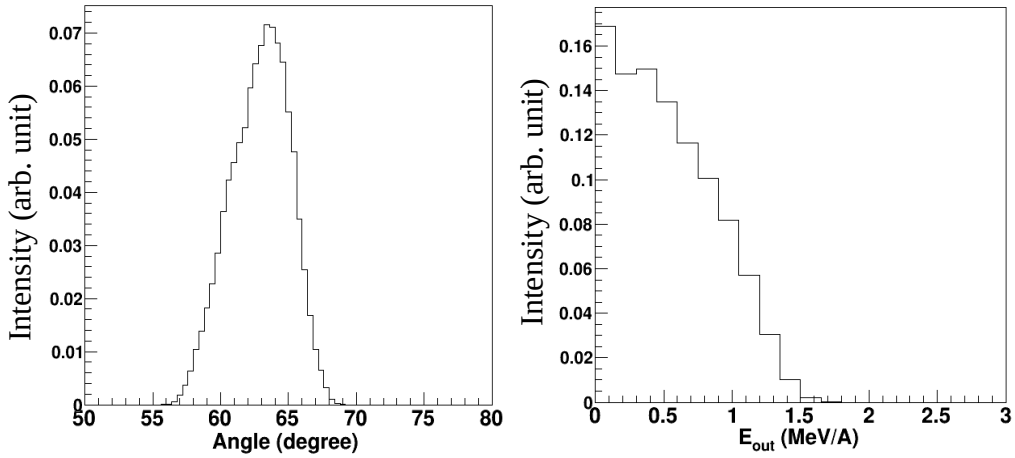

FIG. 2.1.1 (b) Angular and (c) energy distributions of ^{195}Os ejected from the target in the MNT reactions of ^{136}Xe (9.4 MeV/nucleon) + ^{198}Pt (12.5 mg/cm^2).

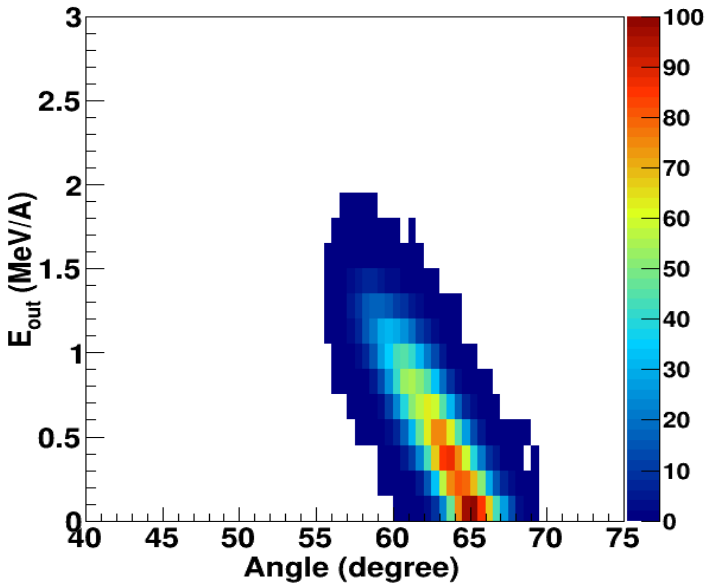

FIG. 2.1.1 (d) Correlation between the angles and the kinetic energies of ^{195}Os from the target in the MNT reactions of ^{136}Xe (9.4 MeV/nucleon) + ^{198}Pt (12.5 mg/cm^2).

2.2 KEK Isotope Separation System

It is required to collect and separate single nuclide, ^{195}Os with high efficiency in order to perform the precise nuclear spectroscopy. The KEK Isotope Separation System (KISS) was used for our measurements. FIG. 2.2 shows a schematic view of KISS, which consists of a gas cell system combined with a mass separator.

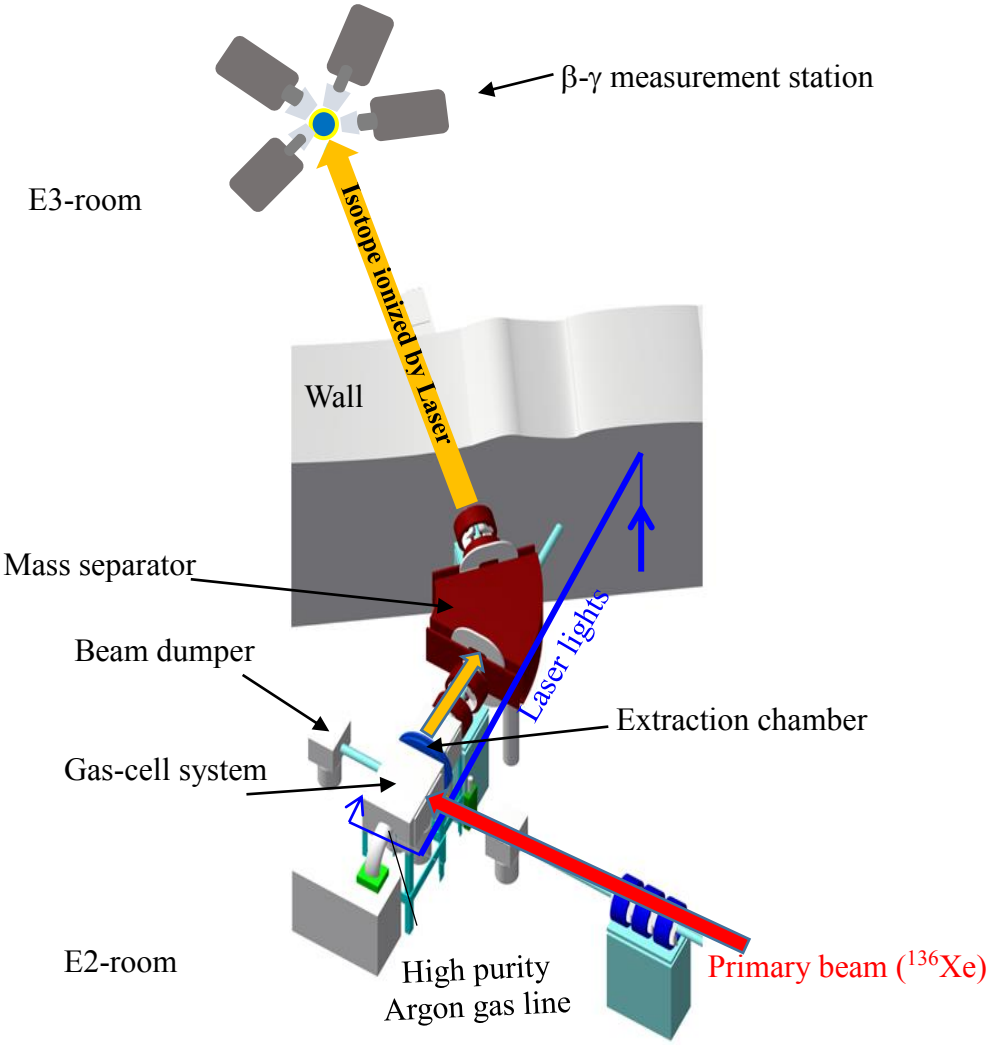

FIG. 2.2 Schematic view of KISS.

2.2.1 Gas cell system

The production and collection of TLF's, the laser resonance ionization, and the ion beam extraction are performed in the gas cell system. FIG. 2.2.1 (a) shows a schematic view of the gas cell system [37]. Primary beam of ^{136}Xe (10.75 MeV/nucleon), which is provided from RIKEN Ring Cyclotron, impinges on the energy degrader consisting of three titanium foils with a thickness of 3 μm (9 μm in total) to tune the injection beam energy on the target by reducing it to 9.4 MeV/nucleon.

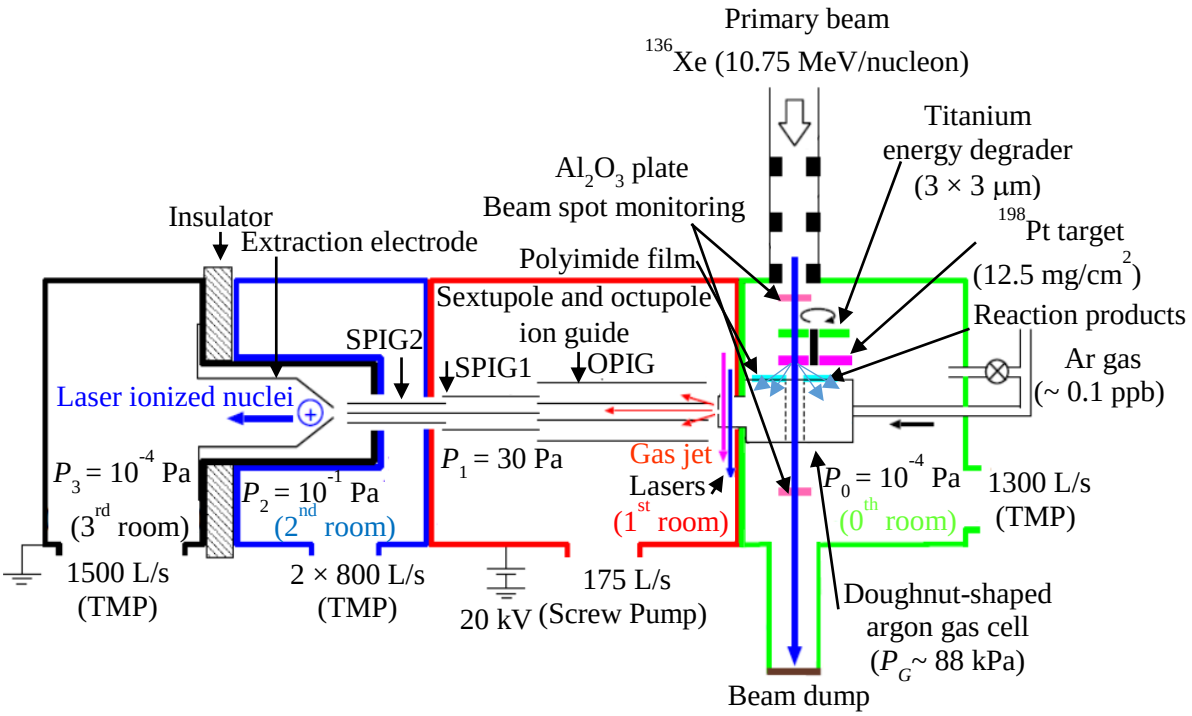

FIG. 2.2.1 (a) Schematic view of the gas cell system [37]. The boundaries of the first, the second and the third rooms for a differential pumping are indicated by red, blue and black lines, respectively.

After the energy degradation, the beam impinges on a ^{198}Pt target. FIG. 2.2.1 (b) indicates the injection beam energy dependence of the relative yields of ^{195}Os ejected from the target. It is evaluated by the GRAZING calculations. The injection energy of 9.4 MeV/nucleon is near the peak of the yields. The TLF's recoils from the target are implanted into the argon gas filled in a gas cell at the pressure of several tens kPa.

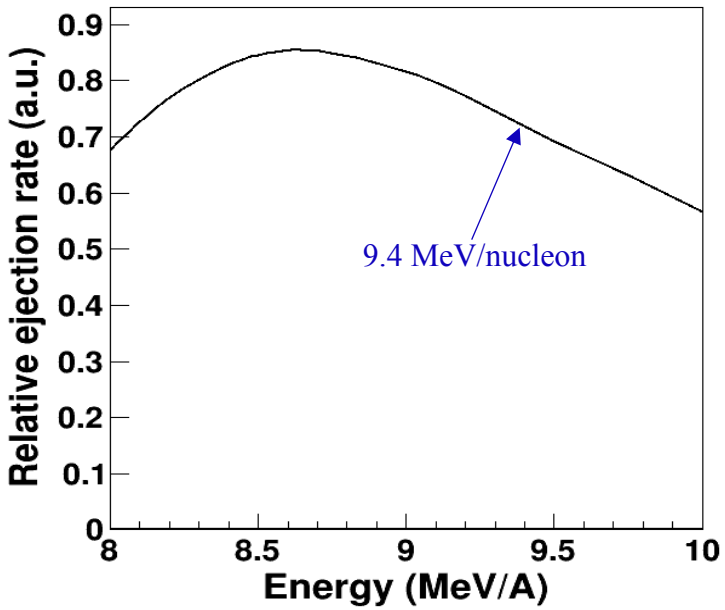

FIG. 2.2.1 (b) ^{136}Xe beam energy dependence of relative yields of ^{195}Os ejected from the ^{198}Pt target. It is evaluated by the GRAZING calculations.

They are neutralized in the gas, and then are transported to the exit of the gas cell by the laminar gas flow. Those neutral atoms are ionized by using an element-selective laser ionization technique just before the exit, and those ions are extracted from a gas cell exit-orifice with 1 mm in diameter and transported through Multi-RF Ion Guides (MRFIG's) toward an acceleration electrode with the acceleration voltage of 20 kV. In order to keep the high vacuum around 10^{-4} Pa at the acceleration area, a differential pumping system is used from the gas-cell exit to the acceleration electrode as shown in FIG. 2.2.1 (a).

For the primary beam tuning, two aluminum oxide (Al_2O_3) plates are placed at upstream and downstream of the gas cell. The effective area of the Al_2O_3 plate is 20 × 20 mm^2 and thickness is 1 mm. The beam position and size are adjusted by monitoring the fluorescence emitted from the upstream Al_2O_3 plate by a camera. Then, the beam transport passing through the gas cell is confirmed by using the downstream Al_2O_3 plate.

2.2.2 Rotating energy-degrader and target

The energy-degrader, Al_2O_3 plate and the production target are set at five rotating wheels (three for the degrader, one for the Al_2O_3 plate and another for the target) to reduce the thermal damage by the energy deposit in those materials [37]. FIG. 2.2.2 (a) shows a front view of the wheel. The width and center diameter of the wheels are 10 mm and 60 mm, respectively. The area was segmented to eight parts by wheel spokes which have 3 mm width, which makes a dead fraction of 13%. A top view of the assembled wheels is shown in the FIG. 2.2.2 (b). The red arrow indicates the primary beam. The wheels are rotated in the speed of 1000 rpm. The motor is cooled by a water-cooled copper block, which also plays a role of a collimator for the primary beam with a diameter of 10 mm and a length of 35 mm.

To prevent the primary beam from hitting the wheel spokes, the primary beam is chopped. Each wheel has eight ID tags of the wheel spokes as shown in FIG. 2.2.2 (a). A photo-sensor is installed to identify those ID tag positions for the first wheel to ensure the beam chopping timing [38]. The spokes of the first wheel are covered by eight Al_2O_3 plates. Timing and duration of beam-chopping were adjusted by monitoring the fluorescence emitted from the Al_2O_3 plates by a camera. The timing signals for the beam chopping are sent to the chopper of the ion source of the accelerator facility.

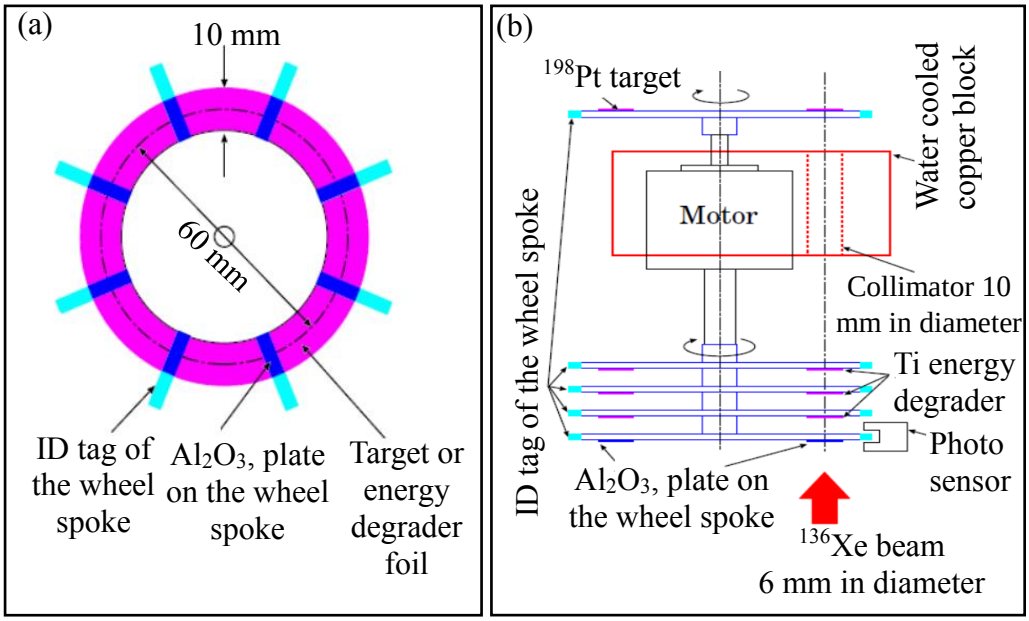

FIG. 2.2.2 Schematic views of (a) a rotating wheel (front view) and (b) a cross sectional view, indicating an assembly of the target and energy-degrader, a photo-sensor and a water-cooled copper collimator.

2.2.3 Doughnut-shaped gas cell

The TLF's produced by the MNT reactions are thermalized and neutralized in the argon gas cell for the laser resonance ionization. FIG. 2.2.3 shows a schematic cross-sectional view of the doughnut-shaped gas cell with the rotating target mentioned in the previous subsection. The primary beam impinges on the rotating energy degraders and target, and then goes through a vacuum pipe with an aperture with a diameter of 15 mm of the gas-cell without entering it.

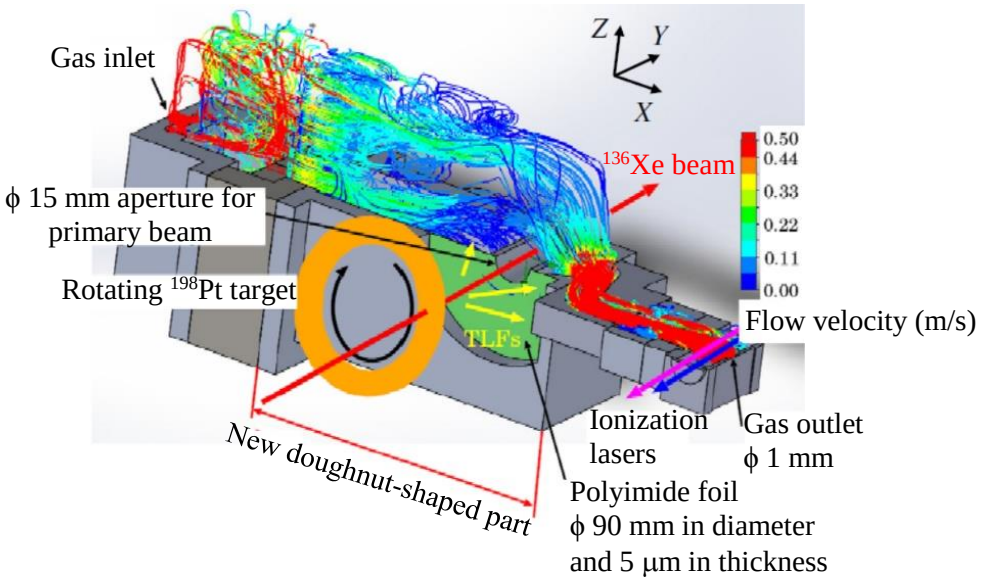

FIG. 2.2.3 Schematic view of the doughnut-shaped gas cell [37].

It suppresses the plasma induced by the primary beam in the gas, which would cause re-neutralizations of the laser resonance ions of interest to reduce its extraction efficiency. The beam was finally stopped at a water-cooled beam dump as shown in FIG. 2.2.1 (a). The TLF's and the elastically scattered beam particles are implanted in the gas cell by penetrating a thin polyimide film of 90 mm in diameter and 5 μm in thickness. The angular acceptance of the window is designed to be $48^{\circ}-79^{\circ}$, which enables a full coverage of the ^{195}Os emission angles of $63^{\circ} \pm 5^{\circ}$ in the laboratory frame [39]. Both surfaces of the polyimide film are coated with a 10-nm layer of gold to avoid charge up on the surfaces. A stainless-steel honey comb grid [40] with 92.5% transparency and a thickness of 0.5 mm covers the polyimide film to maintain the argon gas pressure up to 88 kPa, which is used in the measurements. The colored lines in the FIG. 2.2.3 indicate the calculated argon gas velocities along with flow trajectories to the gas cell outlet [37]. The measured mean transport time of the TLF's from their stopping region to the gas cell exit is 455 ms. Thus, it is enough fast to extract ^{195}Os.

2.2.4 Laser resonance ionization

The neutralized TLF's are element-selectively just before the gas cell exit by the two-color two-step laser resonance ionization technique. FIG. 2.2.4 (a) shows the schematic view of the laser resonance ionization for the ^{195}Os isotope. The neutral atoms are excited by photo-absorptions of a laser light having certain wavelength λ_1. The value of λ_1 (247.7583 nm) corresponds to the excitation energy of the excited state, which is characteristic to the element. This value has been estimated by taking account the isotope shifts from known values of stable isotopes, ^{188,190,192}Os. The atomic continuum state above the ionization potential is populated from the excited state by photon-absorptions of subsequent lasers with a wavelength λ_2 (307.9 nm). Thus, the only a specific element can be ionized in this scheme.

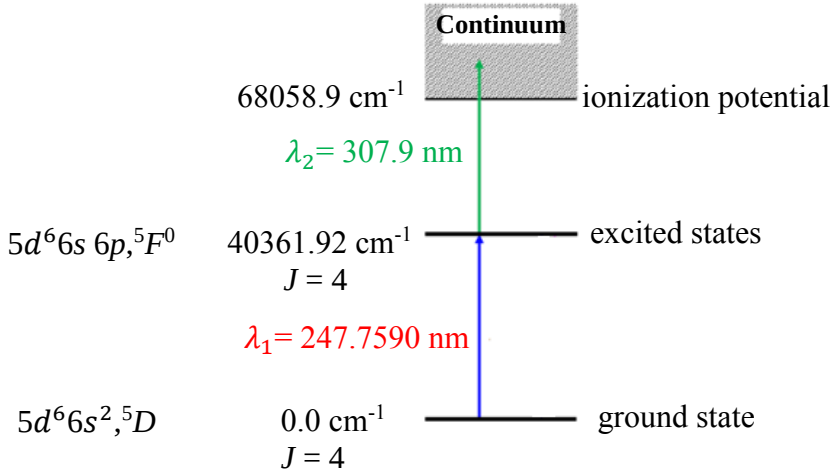

FIG. 2.2.4 (a) Schematic view of the two-color two-step laser resonance ionization scheme for the ^{195}Os isotope.

FIG. 2.2.4 (b) shows a setup of the KISS laser system. There are two excimer lasers (XeCl, Lambda Physik, LPX240i, 307.9 nm) triggered by a function generator (Tektronics, Inc., AFG1022) with a repetition rate of 100 Hz. One is used directly to populate the continuum state above the ionization potential, referred as ionization laser and the other pumps a dye laser (Radiant Dyes, NarrowScan), which generates an excitation laser light with the wavelength of 247.7590 nm by using the dye of Coumarin 500 (C500) and a second harmonic generator (SHG). The paths of the excitation and ionization lasers are indicated by the blue and green lines, respectively. The spacial overlap of two lasers at the gas cell are adjusted by using mirrors with actuators to maximize the ion yields during the experiment. Parts of the excitation and the ionization lasers are irradiated in photo diodes (Electro-Optics Technology Inc., ET3020) to

monitor the timing of those lasers with an oscilloscope. The time difference between two lasers are adjusted to keep the maximum ion yields during the experiment.

(b)

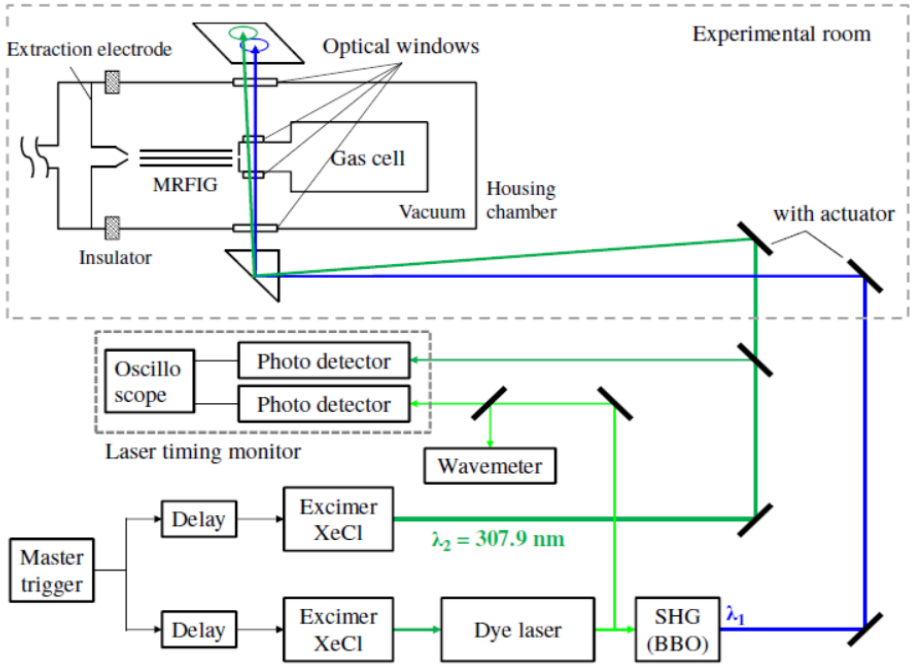

FIG. 2.2.4 (b) Schematic view of the laser system.

2.2.5 Beam transport system

The element selected ion beams with the energy of 20 keV are analyzed by their masses by a dipole magnetic field and then transported to a detector station. FIG. 2.2.5 shows an ion optical configuration of KISS beam line. It is EIN-ES-EQD-MD-MQD-F1-EQT-ES-F2-F3, where EIN, ES, EQD, MD, MQD and EQT denote an Einzel lens, two sets of electric horizontal and vertical steerers, an electric quadrupole doublet, a magnetic dipole, a magnetic quadrupole doublet and an electric quadrupole triplet, respectively. F1, F2 and F3 indicate the first, the second and the third focal planes. One of vertical steerers at the first ES is also used to chop the beam for the decay measurements that are described later. The mass is selected by the dipole magnetic field in the MD. The mass resolving power measured at F1 is $M/\Delta M$ = 900, which is high enough to separate isotopes in the mass region of $A \sim 200$. The horizontal slit at F1 ensures only the beam particles with a certain mass number to be transported to the downstream. A movable two-dimensional beam-profile detector using a shevelon-type Multi-Chanel Plate (MCP) is located at F2. It has an active area of 40 mm in diameter. The KISS beam impinges on a surface of the MCP and

the secondary electrons are accelerated and multiplied by the voltages applied to the front (-1900 V) and the back (+50 V) side of the MCP. The multiplied electrons are collected by anode wires strained to horizontal and vertical directions, respectively, with 1-mm pitch, which are set at the potential of +300 V. There is a movable Chanel Electron Multiplier (CEM) at F3, which is used to tune the beam position for its transportation to the aluminized Mylar tape located downstream where the β-γ spectroscopy is performed.

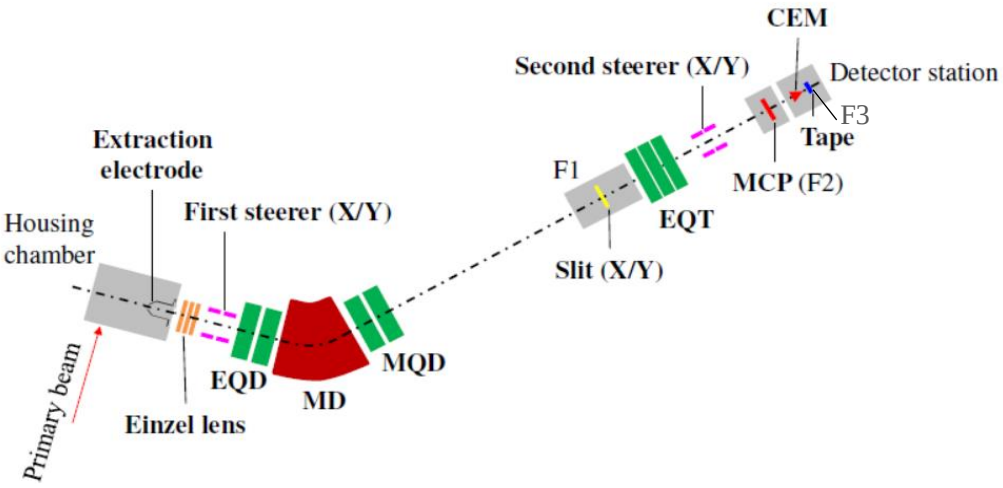

FIG. 2.2.5 Schematic view of the KISS beam line.

2.2.6 Beam transport of ^{195}Os

To transport the radioactive isotope beam of ^{195}Os, the beam transport system was tuned by using $^{198}Pt^{+}$ beam at first. Stable isotope, ^{198}Pt is recoiling out from the target due to an elastic scattering of the primary beam. Its intensity is enough high for the beam line tuning. The wavelength of λ_1= 248.7922 nm was used with the repetition rate of 50 Hz for the excitation laser of ^{198}Pt. FIG. 2.2.6 (a) shows the mass distribution measured with the MCP by sweeping the magnetic field of the MD. The blue and red lines correspond to the mass distributions measured with and without the excitation laser, respectively. The peak corresponding to the $^{198}Pt^{+}$ is clearly seen in the mass distribution with the excitation laser. The $^{198}Pt^{+}$ beam was selected by adjusting the magnetic field of the MD and was transported to the MCP at F2. The ion-optical parameters of the beam line were tuned to make the $^{198}Pt^{+}$ beam being centered and focused on the MCP. FIG. 2.2.6 (b) shows the obtained beam profile measured by the MCP. The beam spot had a distribution of ~2 mm in the Full Width of the Half Maximum (FWHM) both vertically and horizontally. It was focused enough to be transported to the detector station. Finally, the $^{198}Pt^{+}$ beam was transported to the CEM just before the detection station. The second steerer and the EQT

were tuned to maximize the count rate of $^{198}Pt^{+}$ at the CEM. The parameters of the beam transport system were set for the $^{195}Os^{+}$ beam based on the parameters for the $^{198}Pt^{+}$ beam. The magnetic rigidity and electric rigidities ($B\rho$ and $E\rho$) of a singly charged ions can be evaluated by the following relations,

$$B\rho = \sqrt{2\,M_u\,E_k},\ E\rho = 2\,E_k.$$

where M_u is the atomic mass unit and E_k is the kinetic energy of the ion. It is noted that the electric rigidity is independent from mass number. To set the ion-optical parameters for ions of the A = 195 based on the parameters set for the A = 198, only the parameters of magnetic devices should be changed by multiplying a ratio, R (198 to 195), defined as,

$$R\ (198\ \text{to}\ 195) = \sqrt{(195/198)}$$

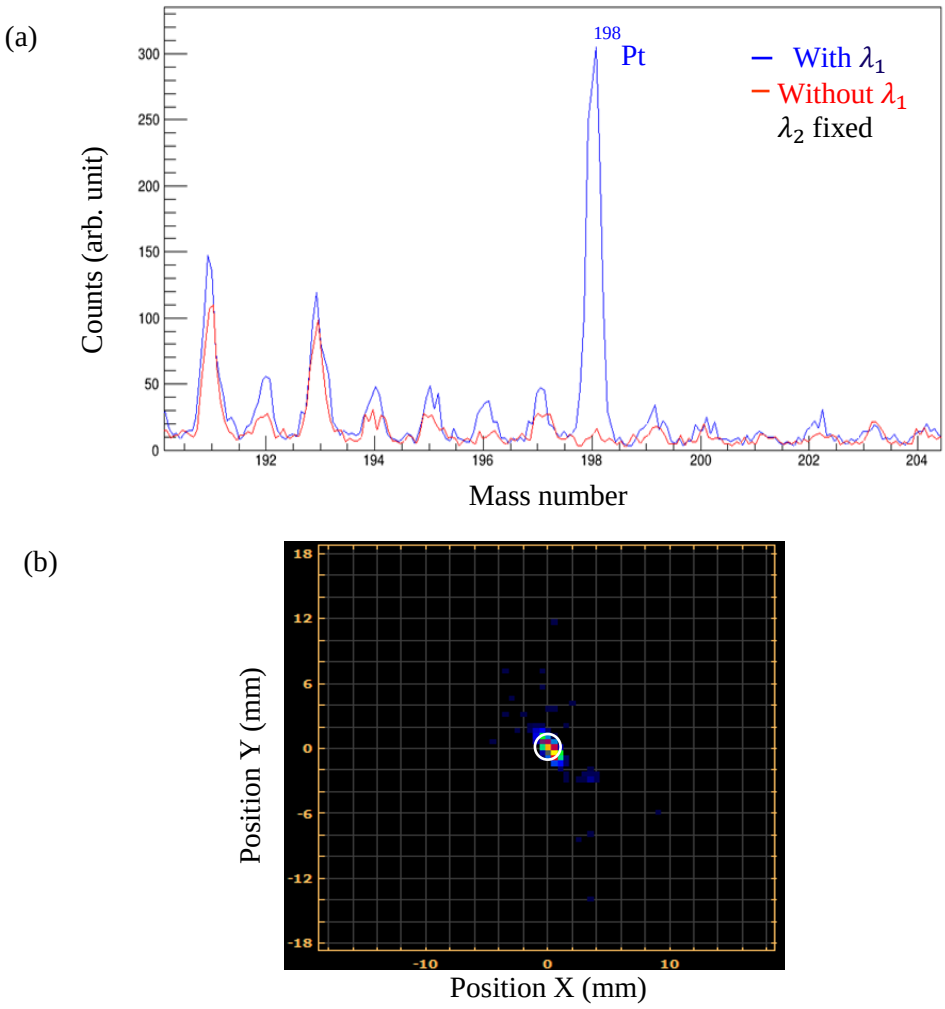

FIG. 2.2.6 (a) Mass distribution measured with the MCP by sweeping the magnetic field of the MD with (blue) and without (red) the excitation laser. (b) Beam profile measured by the MCP.

2.3 Detectors for the β-γ spectroscopy

The detector system consists of a tape transport system, a β-ray detector and γ-ray detectors with veto counters for cosmic-rays and lead shields for environmental background γ-rays. FIG. 2.3 (a) and (b) show an overview and a photo of the KISS detector station, respectively. The extracted ions from the KISS gas cell are implanted on the tape in a vacuum chamber. The tape was made of an aluminized Mylar with a thickness of 12.5 μm and a width of 12.5 mm. The tape was driven by a pair of tape winding devices placed at the top and the bottom of the detector station.

(a)

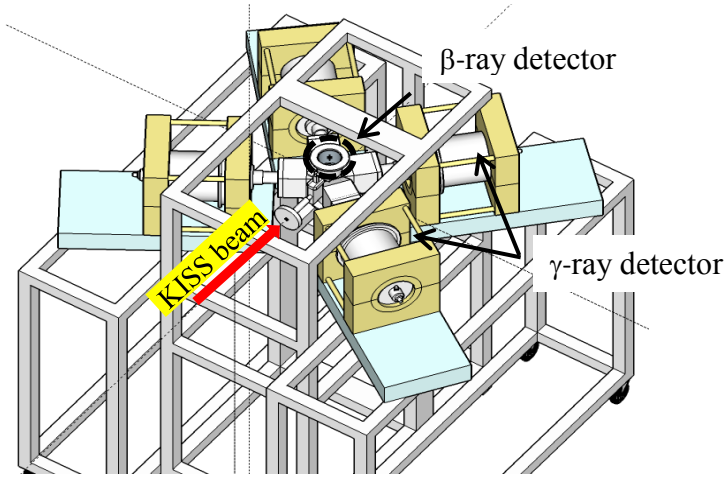

(b)

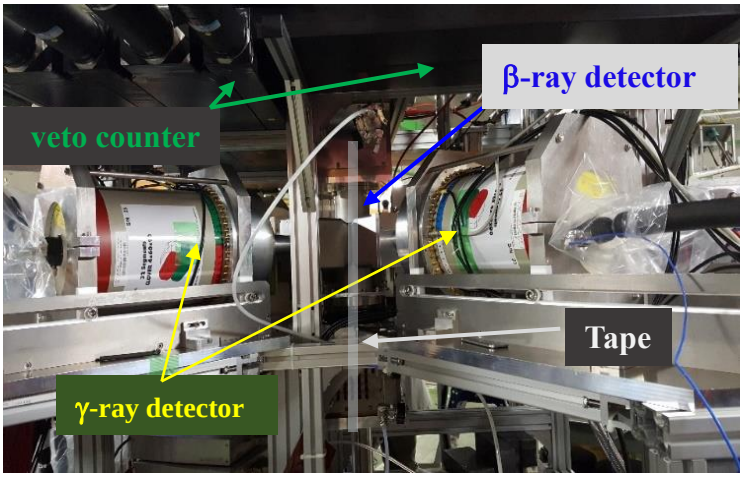

FIG. 2.3 Overview (a) and photo (b) of the KISS detector station.

The β-ray detector is placed in the vacuum chamber to cover the implantation point on the tape. Four clover-type germanium detectors are placed outside of the vacuum chamber. The plastic scintillators are used as veto counters of

cosmic-rays for the β-ray detector. The veto counters consist of 10 wide plastic scintillator bars (BICRON BC408, 5 (H) × 15 (W) × 135 (L) cm^3) and 4 narrow plastic scintillator bars (BC408, 5 (H) × 5 (W) × 135 (L) cm^3) with photomultiplier tubes (HAMAMATSU Photonics K.K., H7195, hereafter PMT's). About 100 lead blocks (typical size of 20 × 10 × 5 cm^3) surrounds the vacuum chamber and the clover-type germanium detectors as a shield to reduce the background events induced by the Compton scattering of environmental γ-rays.

2.3.1 β-ray detector

The multi-segmented proportional gas counter (MSPGC) was developed for the precise β-decay spectroscopy at KISS [44]. The MSPGC consists of 32 narrow and long proportional gas counters. The β-ray events can be distinguished from the background events originated from the cosmic-rays and the Compton scattering of the environmental background γ-rays by analyzing the hit pattern of the counters. The detector gas is Ar (90%) + CH_4 (10%) at the pressure of 1 atm. FIG. 2.3.1 (a) shows a cross-sectional view of the MSPGC. The region between the inner and the outer windows indicated by the orange lines are filled with the gas. The thick blue lines indicate 32 individual gas counter segments, each of which has an anode wire surrounded by the trapezoidal cathode planes. 16 two-layered telescopes are arranged cylindrically around the tape. The anode wires are made of Be-Cu with a diameter of 100 μm. The cathode planes are made of aluminized Mylar films with a thickness of 25 μm. The active length of the gas counter along the tape is 200 mm. The total solid angle of the detector is 80% of 4π. The threshold energies of the β-rays which fire one inner segment and one telescope are around 70 keV and 100 keV, respectively. The MSPGC is located in an aluminum cylindrical vacuum chamber with the outer diameter of 96 mm and the thickness 1 mm. The events detected by counters are analyzed using their hit patterns of 32 segments. The hit pattern is termed as "$M = 1$" when only one inner segment is fired, as "$M \geq 1$" when one inner segment is fired at least, as "$M = 2$" when one telescope is fired, and as "$M = 3$" when one-telescope is fired with another fired outer segment adjacent to it. FIG. 2.3.1 (b) indicates the hit patterns of "$M = 1$", "$M = 2$" and "$M = 3$". FIG. 2.3.1 (c) shows the Q-value dependence of the absolute detection efficiencies of the MSPGC for β-rays with different hit patterns, which were evaluated by the GEANT4 simulation.

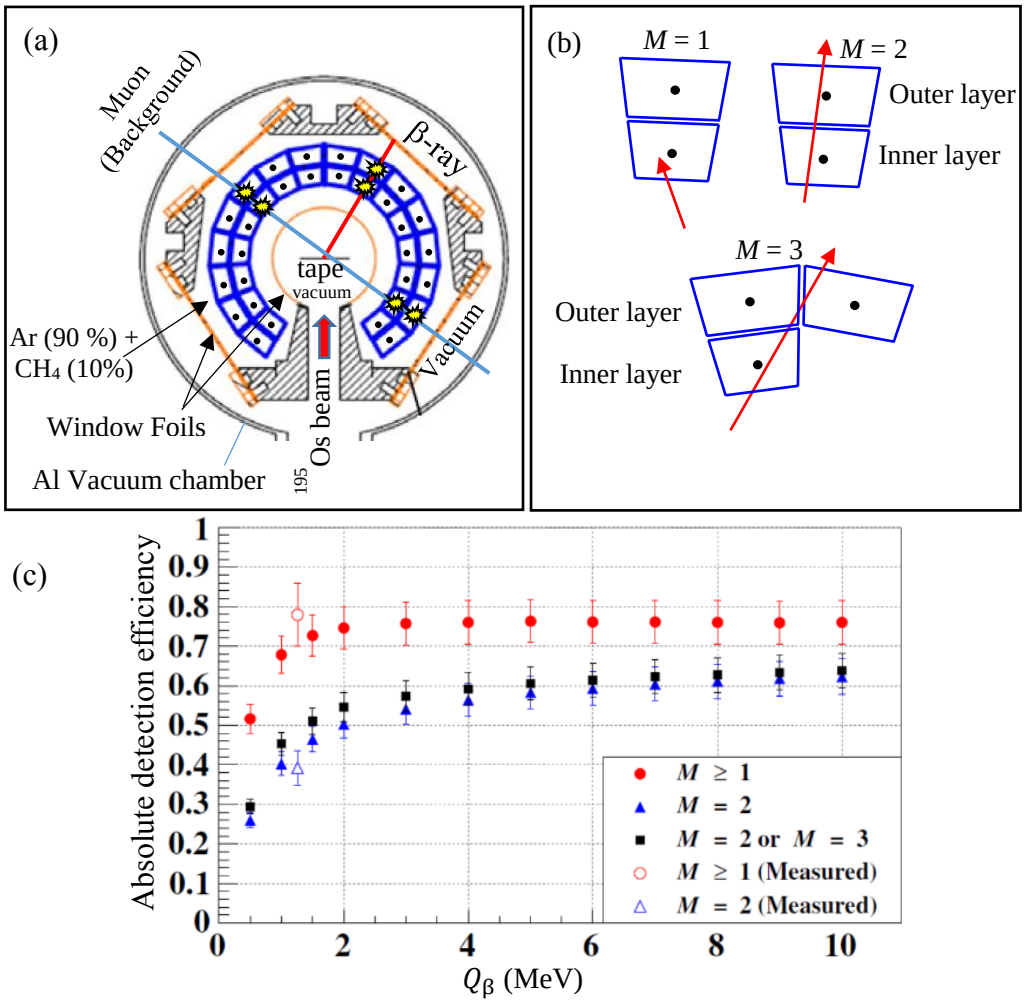

FIG. 2.3.1 (a) A cross-sectional view of the MSPGC. (b) Schematic view of hit patterns. (c) Absolute detection efficiencies of the MSPGC with different hit patterns as functions of Q-values of the β-decay (Q_β) estimated by the GEANT4 simulation (adopted from [44]).

The low background rates of the MSPGC is critical for the β-decay measurements of rarely produced radioactive isotopes. Table 2.3.1 shows the measured background rates for different hit patterns. The β-decay measurements with the hit pattern "M = 2" would be feasible for radioactivities of relatively small intensity around 0.1 cps.

Table 2.3.1 Measured background event rates of the MSPGC for different hit patterns [44].

Hit pattern	"$M \geq 1$"	"$M = 2$"	"$M = 2$" or "$M = 3$"
Background rate	0.6 cps	0.09 cps	0.11 cps

The MSPGC is also sensitive to low-energy photons such as X-rays with energies of around 10 keV, although their detection efficiencies are as low as around 1% [44]. Those X-ray events concentrate on the hit pattern "M = 1", because the energies of the emitted electrons in the interaction between the X-rays and the material such as cathode films are too low to fire one telescope. On the other hand, the β-ray events concentrate on the hit pattern "M = 2" due to their energies higher than 100 keV. Using the hit pattern "M = 1", low-efficient X-ray events can be efficiently selected by reducing the β-ray events. Such feature is useful to search isomeric decays in the coincidence measurements between the γ-ray detectors and the MSPGC, because the characteristic X-rays are emitted following the internal conversion of excited states in cascade transitions from isomeric states. Therefore, it is possible to identify the γ-rays originating from isomeric state decays.

2.3.2 γ-ray detector

Four Super Clover High-Purity Germanium (SC-HPGe) detectors surround the vacuum chamber as shown in FIG. 2.3 (a). They are identified by the serial number SC-HPGe-23, SC-HPGe-24, SC-HPGe-26 and SC-HPGe-27. Each detector has four n-type high-purity germanium crystals with the diameter of 60 mm and the length of 90 mm. FIG. 2.3.2 (a) shows the configuration of four crystals in one detector. They are named as A, B, C and D, and all SC-HPGe detectors were placed as the crystal A and B are located at the upper position in the experimental setup. Each crystal has one anode and eight segmented cathodes as shown in FIG. 2.3.2 (b), and it provides eight segmented signals from those outer cathodes and one-full volume (FV) signal from the inner anode as shown in FIG. 2.3.2 (c). The eight segmented signals can be used for the location information of the γ-ray interactions and the FV signal can be used for the high-resolution measurements of the total energy deposited by the γ-rays in each crystal. Only FV signals of all SC-HPGe detectors are used in our measurements of γ-ray energies. All crystals are cooled down at the temperature of approximately 95 K by liquid nitrogen for an operation with bias voltage of 3500 V. The noise level is less than 2 mV with respect to the typical pulse height around 65 mV for 662-keV γ-rays from a ^{137}Cs source. The rise and decay times of the FV signals are around 100 ns and around 50 μs, respectively.

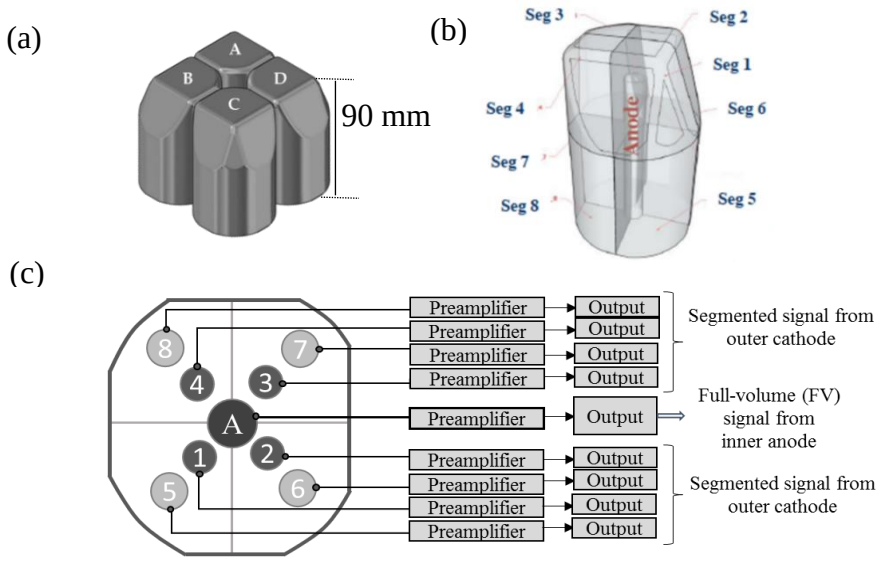

FIG. 2.3.2 (a) Configuration of four crystals in SC-HPGe detector. (b) Anode and segmented cathodes of the crystal. (c) Signals of eight segmented cathodes and one anode from the crystal.

2.4 Time sequence of β-γ spectroscopy

To measure a growth and decay nature of ^{195}Os radioactivity, the beam of ^{195}Os is chopped by the vertical steerer of the KISS beam transport line to make a pulsed beam. The KISS beam is implanted to the tape during a beam-on period (T_{on}) and the implantation is suspended during the following beam-off period (T_{off}) to measure a decay of radioactivity implanted on the tape. Several cycles of the beam-on and the beam-off are repeated in one measurement run. The tape is moved by around 30 cm at the beginning of each cycle to avoid unwanted activities from the remaining radioactive ions and their daughter nuclei on the tape. The time information of the MSPGC and the SC-HPGe detectors as well as the beam chopping are taken to measure the lifetimes of decays.

2.5 Data acquisition system

There exists a CAMAC-based data acquisition (DAQ) system for β-decay measurements at KISS. We have newly introduced TIGRESS DAQ system for γ-ray measurements and combine it to the existing CAMAC-based DAQ system. FIG. 2.5 (a) shows a diagram of the combined DAQ system, and FIG. 2.5 (b) indicates a timing chart of signals to control the DAQ system. When a run-start command enters to the MIDAS DAQ software in the Personal Computer (PC),

it issues a corresponding signal to a Pulse Generator (PG) after the reset of the CAMAC-based DAQ system and the TIGRESS DAQ system. The PG issues a signal to move the tape to the tape device controller. After one second, which is long enough for the actual tape movement of 30 cm, the PG issues a beam-on signal to the beam-chopper and other signals simultaneously to the CAMAC-based DAQ system and the TIGRESS DAQ system. The logical OR of 16 logic signals from discriminators of inner segmented counters of the MSPGC gives a trigger to the CAMAC-based DAQ system. The analog signals from 32 segments of the MSPGC are digitized by Analog-to-Digital Convertors (ADC's) (Hoshin C008) for taking pulse height information and the Time-to-Digital Converters (TDC's) (Hoshin C021) for taking timing information. The TIGRESS DAQ system is employed for SC-HPGe detector signal processing. The trigger signal to the CAMAC-based DAQ system is also fed to the TIGRESS DAQ system for taking timing information of the MSPGC event. The signal corresponding to the beam-on is fed both to the TIGRESS and CAMAC-based DAQ systems. Thus, the consistent timing information is obtained among the MSPGC, SC-HPGe detectors and the beam-on. The accumulated data on the CAMAC-based DAQ system and the TIGRESS DAQ system are transferred to the MIDAS DAQ system and combined there.

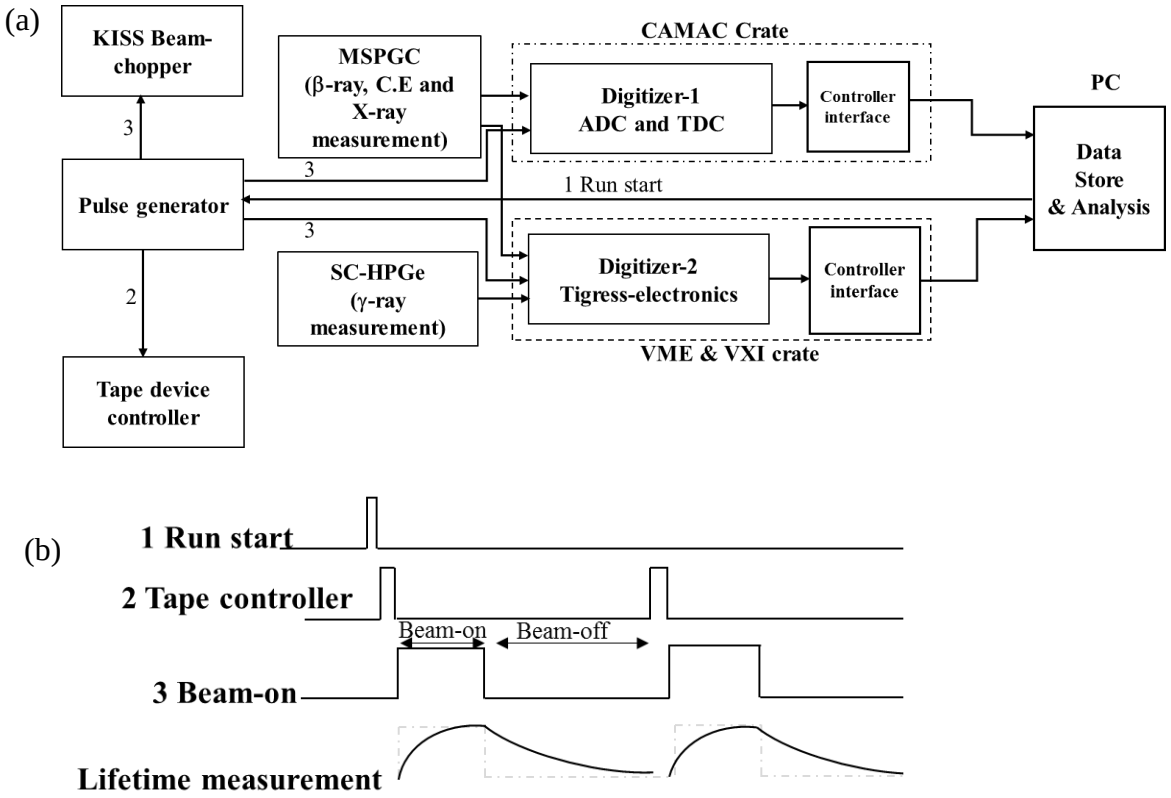

FIG. 2.5 (a) Diagram of the flow of signals in the combined DAQ system. (b) Timing chart of the signals to control the combined DAQ system.

2.5.1 TIGRESS DAQ system

The TIGRRESS DAQ system consists of six 100 MHz sampling digitizer (TIG10) modules of VXI and four collectors (TIG-C) modules of VME. The FV signals from the SC-HPGe detectors are fed to the four TIG10 modules. FIG. 2.5.1 (a) shows a photo of the TIG10 module. It has 10 input channels. One module is used for one SC-HPGe detector. The sampled data are processed by the Field Programmable Gate Array (FPGA) in the TIG10 module to evaluate the pulse height and its timing. FIG. 2.5.1 (b) shows the procedure to process signals in the TIG10 module. A continuous flow of the digitized signal samples from the ADC is directed first to the signal deconvolution logic, which transforms the exponentially decaying pulse into a sequence of rectangular pulses of the duration L in the unit of data sampling [45]. In this process, low frequency part of the noise is attenuated. The n^{th} point in the transformed sequence of the data, F_n, is given by the relation,

$$F_n = D_n - D_{(n-L)} + \frac{1}{\tau}\sum_{i=1}^{L} D_{(n-i)}, \quad \text{.....(2.5)}$$

where D_i represents the i^{th} point in the digitized ADC signal samples and τ is the decay constant of the input signal in the unit of data sampling. It corresponds to the differentiation of the analog signal with a differential time of L. The timing of the input signal is provided by applying the digital implementation of the Constant-Fraction Discriminator (CFD) to the sequence of the data, F_n, which also issues the hit signal for the corresponding crystal.

Another filtering process is applied to attenuate high frequency part of the noise from the deconvoluted signals by a boxcar filter. The n^{th} point in the resulting sequence of data, G_n, is given by the relation,

$$G_n = \frac{1}{K}\sum_{i=0}^{K-1} F_{(n-i)}, \text{ .....(2.6)}$$

where K is an integration time in the unit of data sampling. The resulting sequence of the data has a flat top during the interval of $L - K$. the pulse height of the input signal is evaluated as a value at the flat top region.

FIG. 2.5.1 (c) indicates a diagram of the data flow in the TIGRESS DAQ system. Two TIG10 modules for two SC-HPGe detectors are connected to one slave TIG-C module. Two slave TIG-C modules for four SC-HPGe detectors are connected to the master TIG-C module. One input channel of another TIG10 module is used for the beam-on timing signal, which is connected to one of the slave TIG-C modules. Another slave TIG-C module connected to the master TIG-C module is used for a TIG10 module, one input channel of which is used

for timing signals from the MSPGC. Those channels of TIG10 modules are specially arranged to process the logic signals for the timing.

Signals from any TIG10 modules are transferred to the master TIG-C module through the corresponding slave TIG-C modules. The master TIG-C module issues a trigger signal to all slave TIG-C modules and all TIG10 modules. The slave TIG-C modules accumulate the data of pulse heights and timings from the corresponding TIG10 modules, waiting for a data transfer to the MIDAS DAQ system.

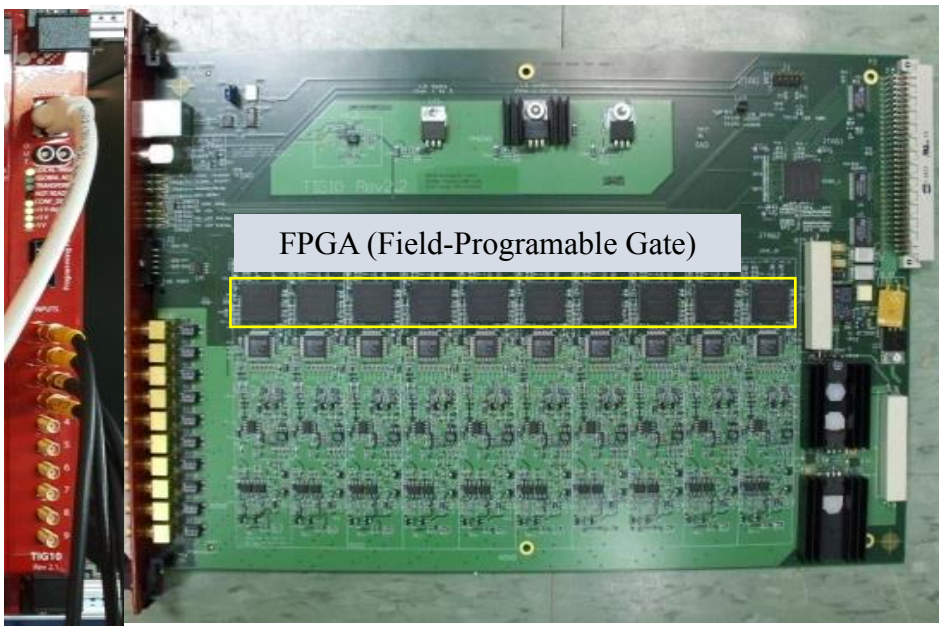

FIG. 2.5.1 (a) Photo of TIG10 module. Each TIG10 module has 10 input channels.

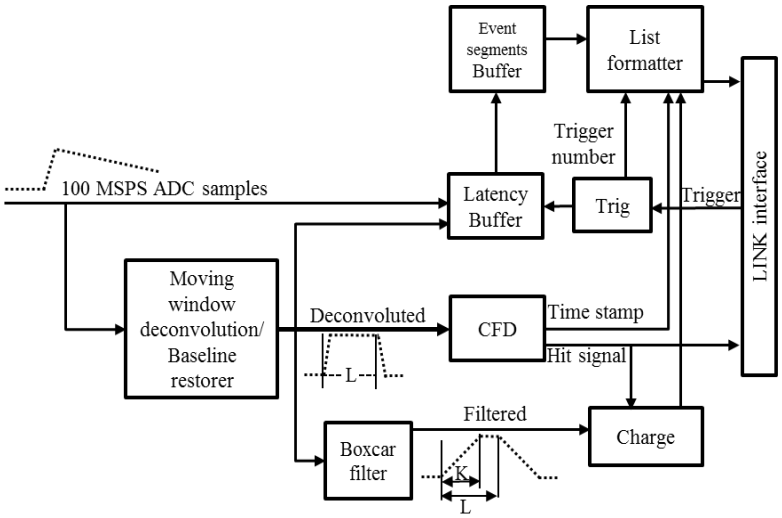

FIG. 2.5.1 (b) Diagram of signal processing in the TIG10 module.

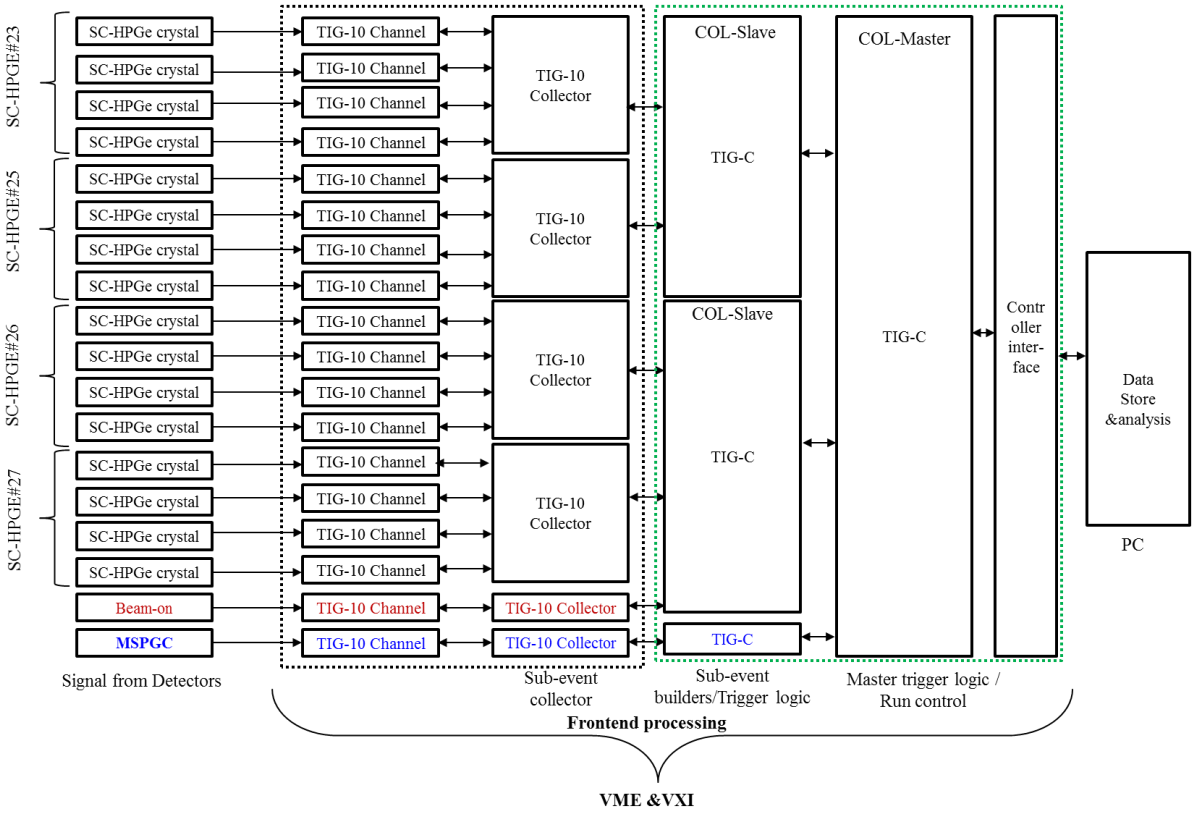

FIG. 2.5.1 (c) Diagram of the data flow in the TIGRESS DAQ system.

2.5.2 Parameter optimization of the TIGRESS DAQ system

The values of L and K were investigated to get better energy resolutions for the SC-HPGe detectors. A γ-ray source of ^{152}Eu was placed at 5 cm from the detector surface of the SC-HPGe-27. The peak profile of 122-keV γ-transition was analyzed for the crystal B by changing the values of L and K. FIG. 2.5.2 (a) shows photopeak energy resolutions (FWHM's) of 122-keV γ-transition as functions of $L - K$ for different K values. The larger K values result in the better energy resolutions. When the value of $L - K$ increases, the resolution becomes better and reach a constant value for $L - K \geq 300$ ns. It indicates that the maximum charge collection time of the SC-HPGe crystal is around 300 ns. FIG. 2.5.2 (b) indicates the detection rates as functions of $L - K$ for different K values. The detection rates reduce at the $L - K$ value between 700 ns and 800 ns. It is due to the limitation of the L value in the TIGRESS electronic system, its maximum is ~10 μs. Considering such limitations of L and K values, we selected K = 8 μs and $L - K$ = 400 ns in our measurements for the best energy resolution. FIG. 2.5.2 (c) shows the energy resolutions of different energy γ-rays with different K and L values before and after the optimization. We achieved the

energy resolutions of 1.50(2) keV for 121.78-keV γ-rays and 2.35(2) keV for 1.33-MeV γ-rays in the FWHM, respectively, being almost close to the guaranteed values (1.35 keV and 2.35 keV).

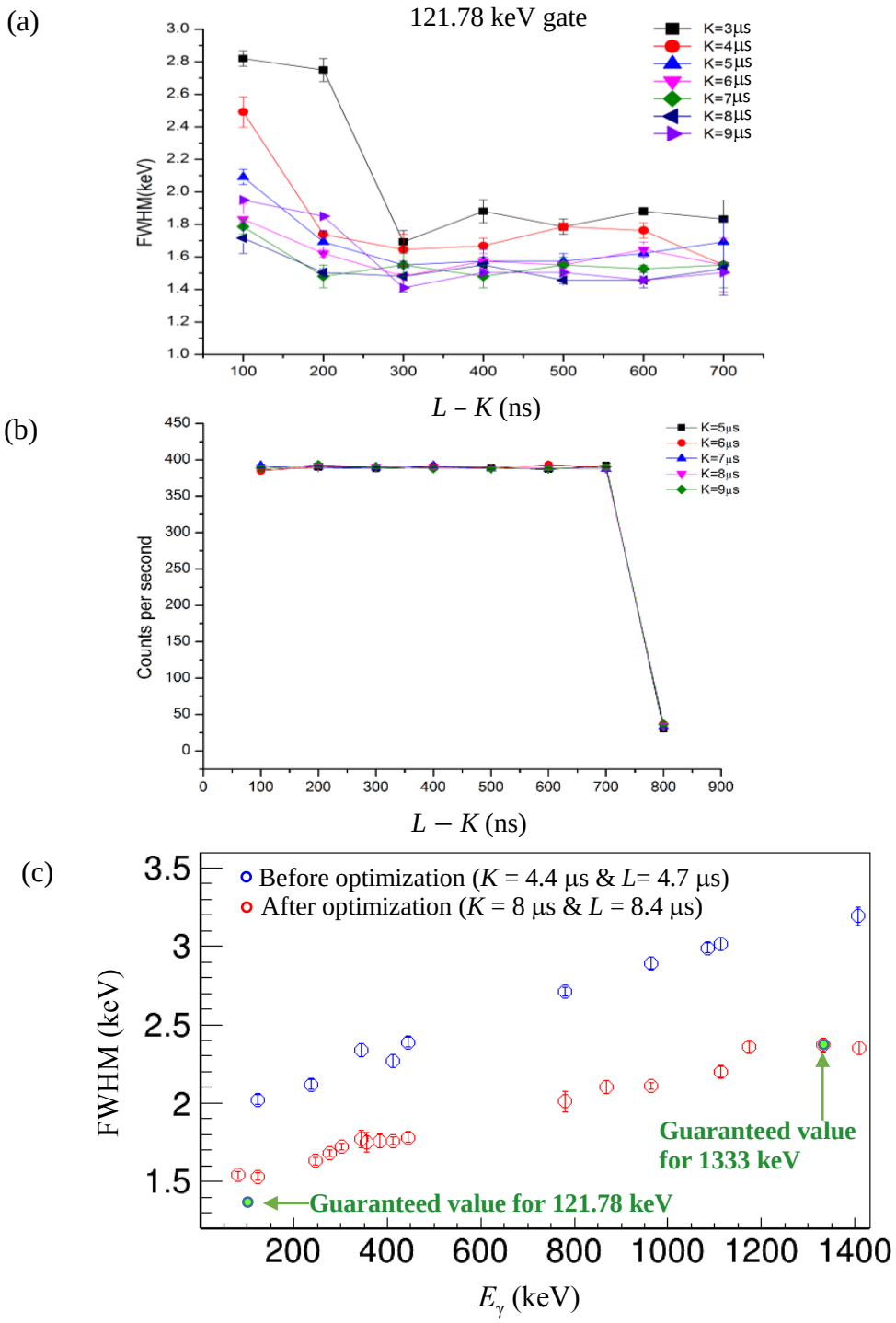

FIG. 2.5.2 (a) Energy resolution for 122-keV γ-rays in terms of the FWHM as functions of $L - K$ for different K values. (b) Detection rate as functions of $L - K$ for different K values. (c) Energy resolutions for different γ-ray energies in two sets of K and L values.

2.6 Chopping conditions of ^{195}Os beams

For the β-γ spectroscopy of ^{195}Os ground state, the T_{on} and T_{off} in the beam chopping cycle were set to be 1.5 times and 4 times larger than its known half-life, 390(66) s, respectively. Two cycles were repeated in the measurement run, which we will refer as "Long run" here after.

The on-line analysis during the experiment indicated an existence of a shorter-lived isomeric state. To investigate this possible isomeric state, we have performed another measurement run with shorter values of T_{on} and T_{off} to avoid the γ-ray contamination from the ^{195}Os ground state decay. The T_{on} and T_{off} were set 120 s and 240 s, respectively. 22 cycles were repeated in the measurement run, which we will refer as "Short run" here after.

Table 2.6 summarizes the measurement runs with their conditions of the beam-on period, the beam-off period, the cycle period and the number of cycles.

Table 2.6 Measurement runs with different beam-on and beam-off periods.

Run	**Beam-on period (T_{on})**	**Beam-off period (T_{off})**	**Cycle period (T_{on} + T_{off})**	**Number of cycles**
Long run	585 s	1560 s	2145 s	2
Short run	120 s	240 s	360 s	22

3 Analysis and Results

3.1 Data obtained by SC-HPGe detectors

3.1.1 Energy calibration

Energy calibration of the SC-HPGe detectors was carried out before the experiments by using two standard sources ^{152}Eu (14.9 kBq) and ^{133}Ba (12.8 kBq) placed at the position where the ^{195}Os ions are implanted. The γ-rays with energies ranging from 81 keV to 1.4 MeV were employed for the energy calibration. The calibration function for each crystal was obtained by the chi-square fitting to a correlation between γ-energies (E_γ) and centroids of γ-ray peaks (P_{ch}) in the pulse height spectrum with a linear function including an offset channel (b) in the measured spectrum,

$$E_\gamma = a \times (P_{ch} - b).$$

FIG. 3.1.1 (a) shows a sample of the obtained energy spectra with the ^{152}Eu source after the energy calibration for a single crystal of SC-HPGe-27. FIG. 3.1.1 (b) shows the deviation of the calibrated energies from the known energies for the ^{152}Eu source. Calibrated values agree to the reported ones within 0.2 keV.

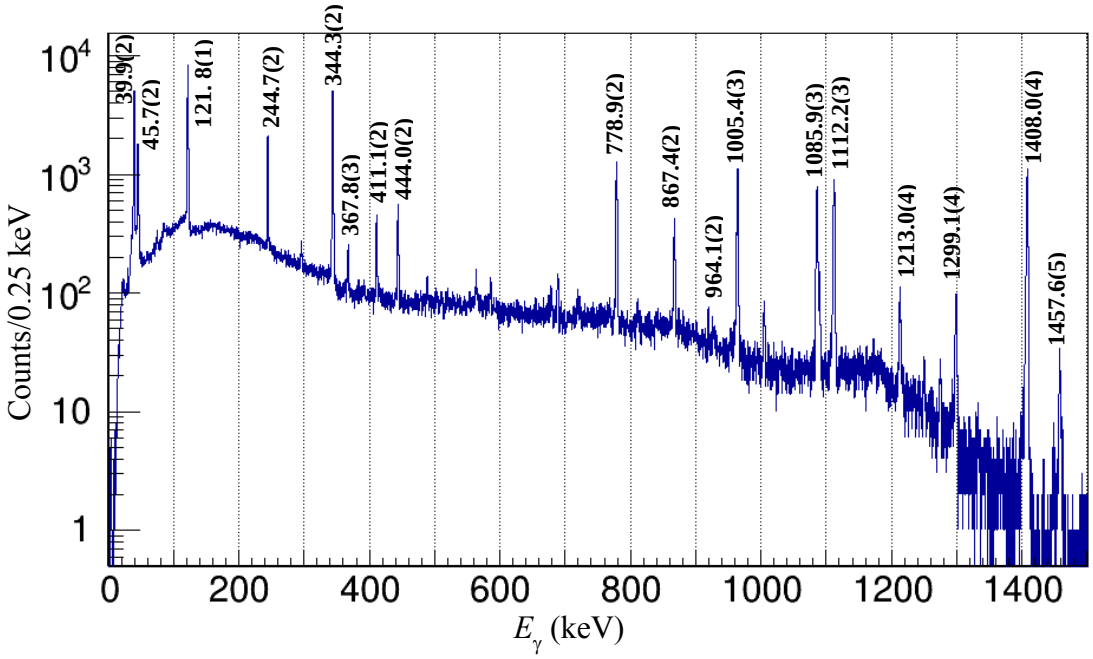

FIG. 3.1.1 (a) A sample of energy spectra with ^{152}Eu source after the energy calibration.

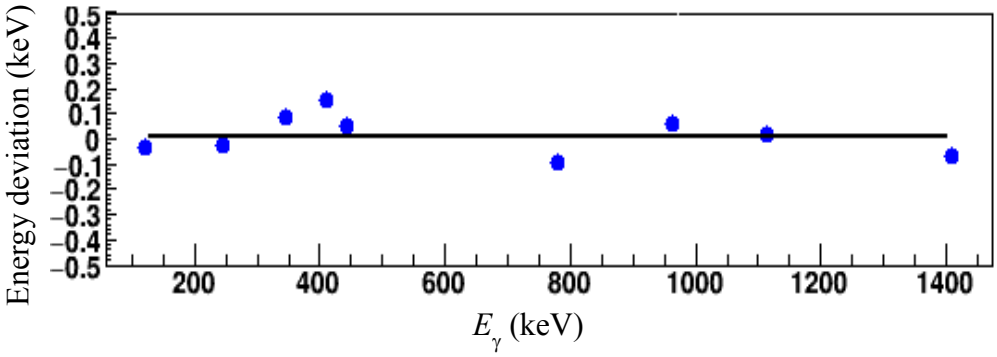

FIG. 3.1.1 (b) The differences of the calibrated energies from the referred γ-ray energies of ^{152}Eu. Determination uncertainties for centroid positions of γ-ray peaks are within the blue marks.

3.1.2 Add-back

The SC-HPGe detector has four crystals in a close-compact arrangement as shown in FIG. 3.1.2 (a). The Compton scattering, which is the dominant interaction process for γ-rays of ~0.2 to 7 MeV in germanium material [46], can deposit a part of its energy in one crystal and then enter a neighboring crystal to deposit a portion or the remainder of its energy in one detector. Since a full energy peak of γ-ray corresponds to the transition energy, the Compton-scattered events with its energy deposit in several crystals should be added back to reconstruct the original energy of the γ-ray as shown in FIG. 3.1.2 (a). Energies of all crystals in a detector within a time window of 200 ns were assumed to be a Compton-scattered event and summed to one energy. FIG. 3.1.2 (b) shows a comparison of energy spectra with the ^{152}Eu source between for the add-back mode (red) and for the sum of single spectra of four crystals (blue). Thanks to the add-back procedure, the background events by Compton scatterings, especially mainly appeared in low energy region are reduced by a factor of almost 2. The insets in FIG. 3.1.2 (b) show an enlargement of the 344-keV and 1.4-MeV full energy photo-peaks. The photo-peak height of 1.4 MeV transition increased by a factor 1.5 with the add-back treatment. Hereafter, the add-back spectra are adopted for any γ-ray analyses.

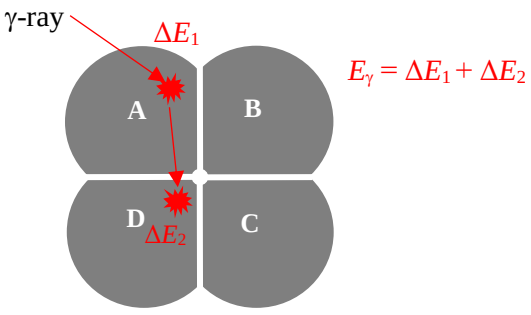

FIG. 3.1.2 (a) Schematic view of the add-back mode for crystals in one SC-HPGe detector.

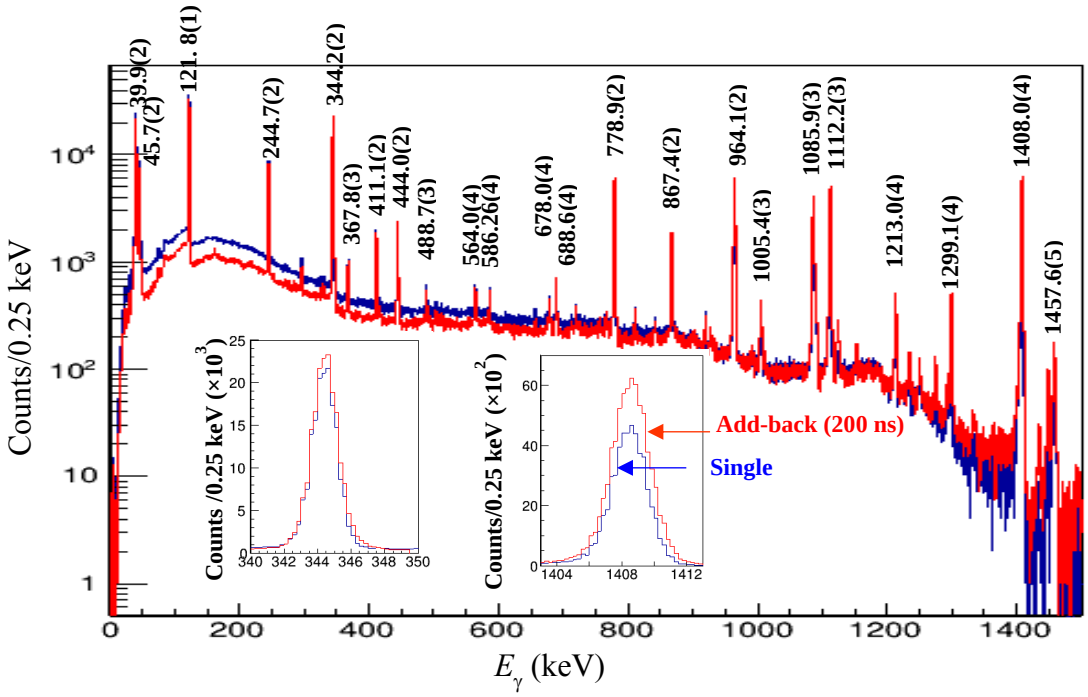

FIG. 3.1.2 (b) γ-ray energy spectra with ^{152}Eu source for add-back mode (red) and sum of single crystals (blue). The insets show enlargements of the 344-keV and 1.4-MeV full-energy photo-peaks.

3.1.3 Efficiency calibration

An efficiency of detecting γ-rays as photo-peaks depends on their energies. The efficiency curve for various photo-peaks in the add-back mode was deduced by the same setup of the measurements. The detection efficiency of a γ-ray photo-peak (ε_γ) has been obtained by using the following relation,

$$\varepsilon_\gamma = \frac{N_\gamma}{I_\gamma \times T_{\text{live}}}, \qquad \text{.....(3.10)}$$

where N_γ is the integrated counts of the measured γ-ray photo-peak, I_γ is the absolute emission rate of the γ-ray, T_{live} is a live time of the measurement. I_γ has 10% error owing to the uncertainty of the activity for standard γ-ray sources, ^{152}Eu and ^{133}Ba. T_{live} is obtained in the relation,

$$T_{\text{live}} = T_{\text{real}} \times \frac{N_{\text{acc}}}{N_{\text{req}}},$$

where T_{real} is a real time of the measurement, and N_{acc} and N_{req} are numbers of accepted and requested triggers in the TIGRESS DAQ system, respectively. T_{real}, N_{acc} and N_{req} are obtained in the TIGRESS DAQ data.

To get the integrated counts of photo-peaks, a function (3.11) was used to fit them in γ-ray energy spectra,

$$y(x) = a_0 + a_1 \times x + a_2 \times x^2 + \frac{a_3 \times a_4}{\sqrt{2\pi}\, a_5} \exp\left(\frac{(x-a_6)^2}{2a_5^2}\right) \quad \text{.....(3.11)}$$

It represents a Gaussian function for the peak and a quadratic function for the background events. The parameter a_2 was fixed to zero for most of the peak fitting. The parameter a_4 corresponds to the width of a bin of the histogram. In this peak fitting function, the parameter a_3 directly gives the integrated counts of the peak.

To obtain the efficiency curve, a polynomial logarithmic function was adopted from the reference [48],

$$\log_e \varepsilon(E_\gamma) = \sum_{i=0}^{5} p_i \left(\log_e\left(\frac{E_\gamma}{E_0}\right)\right)^i, \quad \text{.....(3.12)}$$

where $\varepsilon(E_\gamma)$ is the efficiency of the γ-ray photo-peak with the energy of E_γ, E_0 is a constant value of energy, being fixed at 1 MeV, and $p_i (i = 0 \sim 5)$ are free parameters of fitting. FIG. 3.1.3 shows an energy dependence of a γ-ray detection efficiency summed over four SC-HPGe detectors. The red and blue lines indicate the fitted curves for the add-back mode and for the sum of single spectra of independent crystals, respectively. The absolute detection efficiency was improved by 30% for the γ-rays with the energy of 1 MeV by using the add-back mode compared to the single crystals.

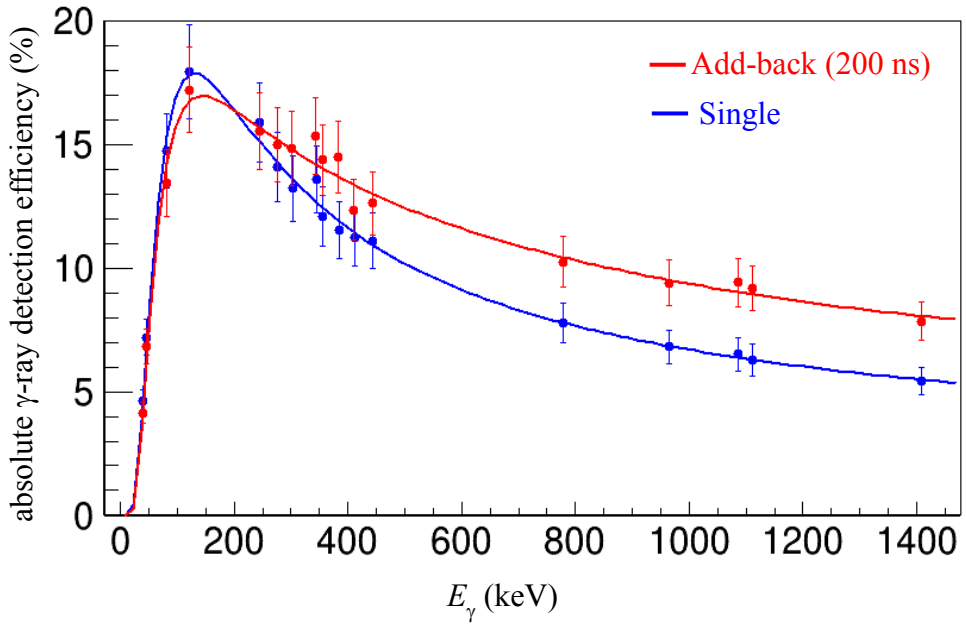

FIG. 3.1.3 Energy dependence of a γ-ray detection efficiency summed over four SC-HPGe detectors. The red and blue lines indicate the fitting curves for the add-back mode and the sum of single crystals, respectively.

3.1.4 γ-γ coincidence

The analysis of γ-γ coincidence events is important to investigate a correlation of relevant γ-transitions. Coincident hits of crystals in one detector are added-back to reconstruct a full energy peak as described in Section 3.1.2. On the other hand, coincident hits of different detectors are considered as events with multiple γ-ray emission. We have analyzed a time correlation between a detected event with single detector and ones with other three detectors for the Long run measurement as shown in FIG. 3.1.4, where coincident event with narrow time width can be found. We have adopted 500 ns as a time window in the γ-γ coincident analysis.

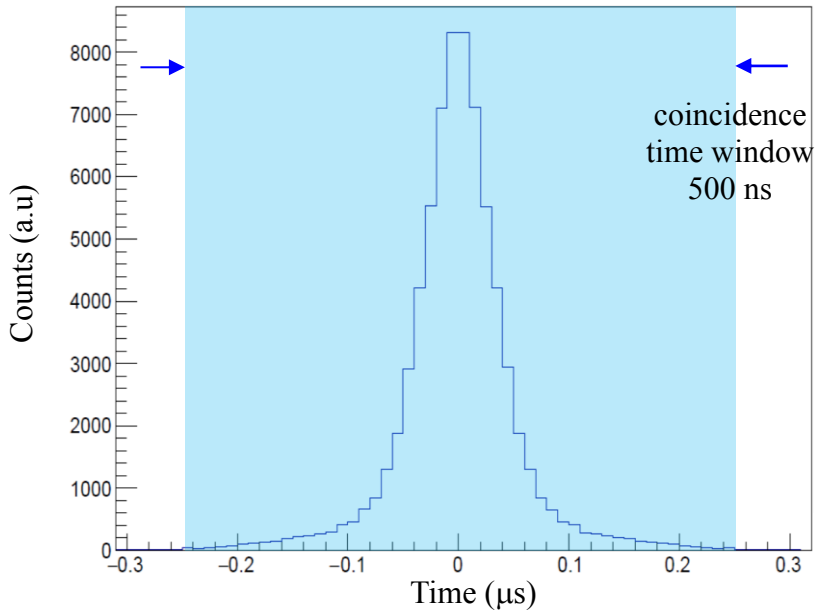

FIG. 3.1.4 Time difference between the events detected with different SC-HPGe detectors measured in the Long run. The γ-γ coincidence time window was set to 500 ns.

3.2 Coincidence between SC-HPGe event and MSPGC events

The analysis of a time correlation between the SC-HPGe event and the MSPGC event is important to investigate β-delayed γ-transitions and γ-transitions from an isomeric state. The timing signal of the MSPGC is fed to the TIGRESS DAQ system to keep a consistent time information between the SC-HPGe- and the MSPGC-events as described in Section 2.5. FIG. 3.2 shows a time difference between the SC-HPGe event and the MSPGC events for the Long run measurement. It is found that the time distribution for coincident events is wider than one for the γ-γ coincidence described in Section 3.1.4. It is due to a slow

time response of the MSPGC, which is mainly caused by an electron drift time from an electron generated point in the counter to the anode wire. The time difference window was set 1 μs for the coincidence analysis between the SC-HPGe event and the MSPGC events.

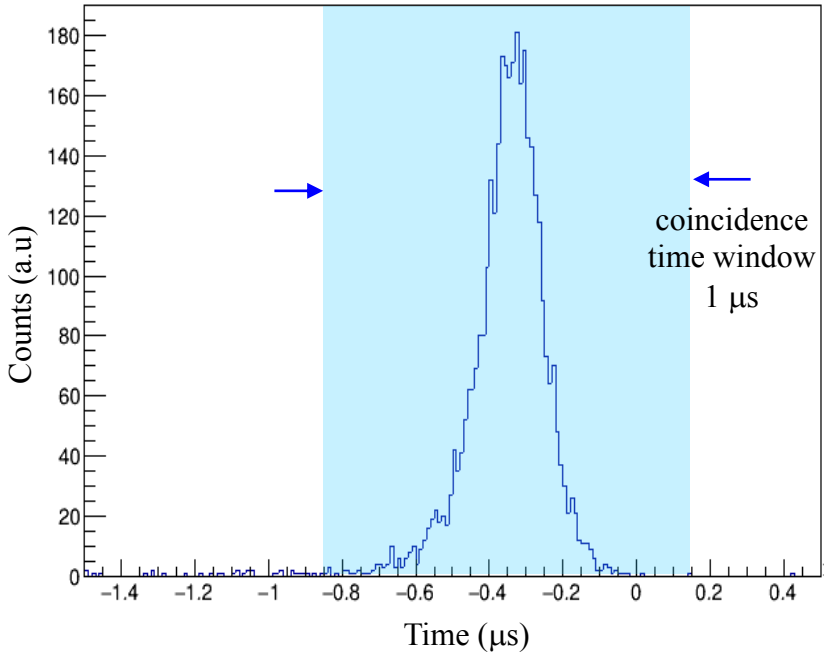

FIG. 3.2 Time difference between events of the SC-HPGe and the MSPGC measured in the Long run. The coincidence time window was set to 1 μs.

3.3 β-γ analysis of ^{195}Os and result

3.3.1 γ-ray energy spectra in coincidence with the MSPGC events

The γ-ray energy spectra in coincidence with the MSPGC events with hit pattern "$M \geq 1$" for the Long run is shown in FIG. 3.3.1. The absolute detection efficiency of the MSPGC hit pattern "$M \geq 1$" is as high as about 75% for β-rays from ^{195}Os. In the FIG. 3.3.1, 25 γ-ray peaks together with characteristic X-rays of osmium and iridium are found.

Table 3.3.1 summarizes the energies of the observed γ-ray and X-ray peaks compared with literature values. The observation of characteristic iridium X-rays indicates that the ^{195}Os isotopes were implanted to the aluminized Mylar tape and their β-decays induced the emission of the K X-rays of ^{195}Ir atoms by following the internal conversion in β-delayed transitions. The energies of 20 γ-ray peaks are consistent with the literature values of ^{194}Ir(n, γ)^{195}Ir reactions [51]. However, 5 γ-ray peaks have no corresponding energies in the literature.

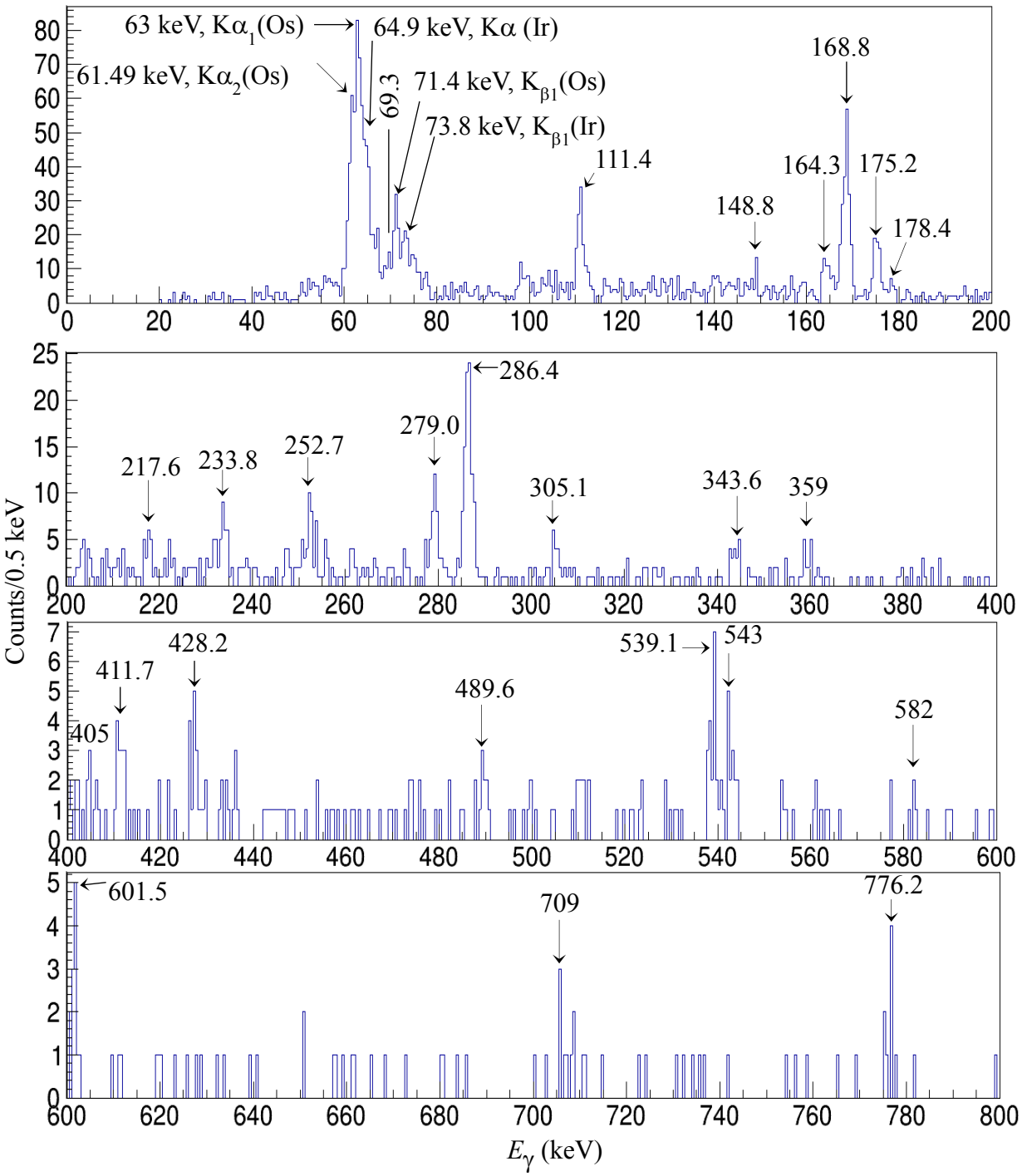

FIG. 3.3.1 γ-ray energy spectra in coincidence with the MSPGC events with hit pattern "$M \geq 1$" measured in the Long run.

Table 3.3.1 γ-ray and X-ray peaks observed in coincidence with the MSPGC events with hit pattern "$M \geq 1$".

E_γ (keV) Measured	E_γ (keV) Literature value	E_γ (keV) Measured	E_γ (keV) Literature value
61.6(1)	61.486 $K\alpha_2$ X-ray (Os) [21]	279.0(2)	Unknown
63.1(1)	63.000 $K\alpha_1$ X-ray (Os) [21]	286.4(1)	286.516(4) [50]
64.8(1)	64.896 Kα X-ray (Ir) [21]	305.1(3)	Unknown
71.3(1)	71.414 $K_{\beta1}$ X-ray (Os) [21]	343.6(3)	342.854(7) [50]
73.4(1)	73.560 $K_{\beta1}$ X-ray (Ir) [21]	347.3(5)	347.45(3) [50]
69.3(2)	69.181(1) [50]	359.4(4)	359.445(4) [50]
111.4(2)	111.300(2) [50]	405(1)	406.574(7) [50]
148.8(4)	Unknown	411.7(2)	412.033(6) [50]
164.3(2)	164.333(3) [50]	428.2(2)	429.629(7) [50]
168.8(2)	Unknown	489.6(3)	489.50(3) [50]
175.2(1)	175.222(2) [50]	539.1(3)	539.212(23) [50]
178.4(2)	178.529(4) [50]	543.1(3)	542.52(21) [50]
217.6(4)	217.340(4) [50]	583(2)	581.792(13) [50]
233.8(3)	233.512(4) [50]	601.1(4)	600.86(4) [50]
252.7(3)	252.685(4) [50]	776.2(4)	Unknown

3.3.2 Hit pattern analysis of γ-rays in coincidence with the MSPGC events

To identify the origin of the observed γ-rays, they are analyzed with different hit patterns of the MSPGC.

FIG. 3.3.2 (a) shows γ-ray energy spectra in coincidence with the hit pattern "$M = 1$" (red) and "$M = 2$" (blue). The characteristic X-rays of iridium and platinum are dominant for the hit pattern "$M = 2$" condition, indicating the major origins of β-decays of osmium and iridium. Two peaks with the energies of 98.5(2) and 130(1) keV are also observed, which are not identified for the hit pattern "$M \geq 1$" condition because of its higher background events. Those energies correspond to the literature values for the β-delayed γ-rays of ^{195}Ir, which is a daughter nucleus of implanted ^{195}Os nucleus.

The characteristic X-rays of osmium are clearly found with the "$M = 1$" condition, indicating a possibility of an isomeric decay of osmium. The γ-ray peaks with the energies of 111.0(1), 148.8(2), 168.8(2) and 279.0(2) keV dominant in the "$M = 1$" condition are also the candidates as γ-transitions from the isomeric state.

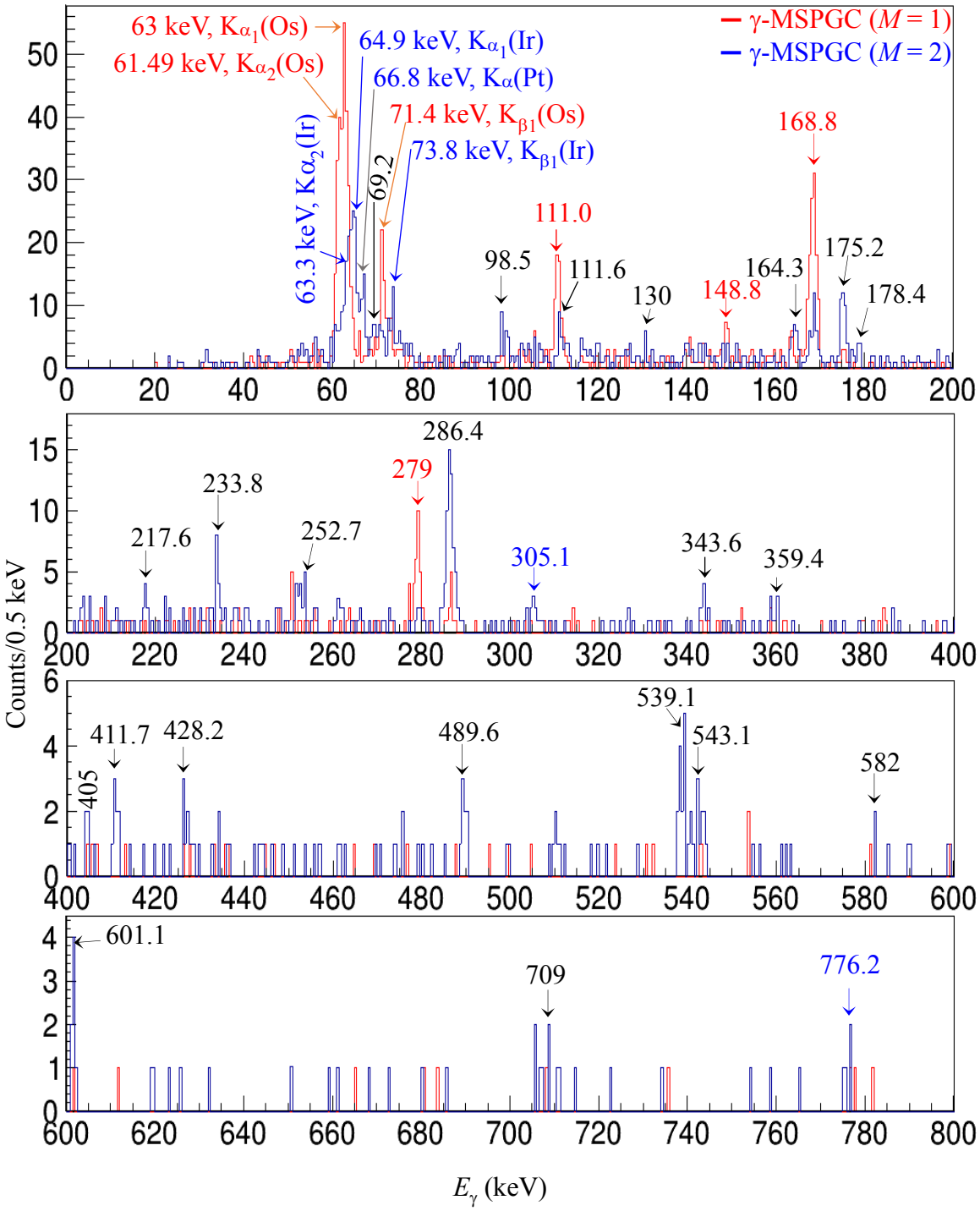

FIG. 3.3.2 (a) γ-ray energy spectra in coincidence with the MSPGC events with hit pattern "$M = 1$" (red) and "$M = 2$" (blue), respectively, measured in the Long run.

The peak with an energy of 111.4(2) keV found with the hit pattern "$M \geq 1$" is well resolved to two transitions with the energies of 111.0(1)- and 111.6(2)-keV from the comparison with different spectra obtained with the hit pattern "$M = 1$" and "$M = 2$", respectively, as shown in FIG.3.3.2 (b). Separated γ-transition with an energy of 111.6(2) keV with "$M = 2$" condition can be identified as the same transition of 111.3(2) keV reported in the ^{194}Ir(n, γ). On the other hand, 111.0(1)-keV γ-transition observed with "$M = 1$" condition would belong to the decay transitions from the isomeric state of ^{195}Os. Thus, totally 28 γ-ray peaks together with K X-rays of osmium, iridium and platinum were observed.

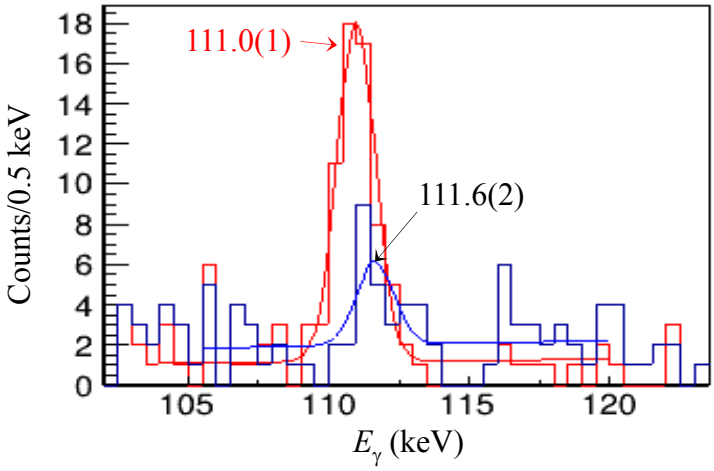

FIG. 3.3.2 (b) Extended view of γ-ray energy spectra around 111 keV in coincidence with the hit pattern "$M = 1$" (red) and "$M = 2$" (blue).

Among those 28 γ-transitions, the energies of 20 γ-transitions agree with literature values of ^{194}Ir(n, γ)^{195}Ir [51]. Those are supposed to be β-delayed γ-rays of ^{195}Os. The energies of other 2 γ-ray peaks are consistent with the literature values of β-delayed γ-transitions of ^{195}Ir ground state [50]. Another 6 γ-ray peaks with the energies of 111.0(1), 148.8(2), 168.8(2), 279.0(2), 305.1(3) and 776.2(4) keV have no corresponding literature values. Among those newly found γ-transitions, the first four are assumed to be associated with the isomeric decay of ^{195}Os, because their intensities become dominant for the case "$M = 1$" compared to the "$M = 2$". The last two are supposed to be β-delayed γ-rays of ^{195}Os, because their intensities become dominant for the case "$M = 2$" compared to the "$M = 1$". Table 3.3.2 summarizes all observed γ-ray and X-ray peaks and their possible origins.

Table 3.3.2 The summary of the observed X-ray and γ-ray peaks observed with the hit patterns "$M = 1$" and/or "$M = 2$".

E_γ (keV) Measured	E_γ (keV) Literature value	**Identification the origin of γ-transitions**
61.6(1)	61.486 [21]	$K\alpha_2$ X-ray (Os)
63.1(1)	63.000 [21]	$K\alpha_1$ X-ray (Os)
64.8(1)	64.896 [21]	Kα X-ray (Ir)
66.9(2)	66.831 [21]	Kα X-ray (Pt)
71.3(1)	71.414 [21]	$K_{\beta 1}$ X-ray (Os)
73.4(1)	73.560 [21]	$K_{\beta 1}$ X-ray (Ir)
69.3(2)	69.181(1) [51]	β-delayed γ-ray from ^{195}Os decay
98.5(2)	98.83(1) [50]	β-delayed γ-ray of ^{195}Ir ground state decay
111.0(1)	Newly found	γ-ray from ^{195}Os isomeric state decay
111.6(2)	111.300(2) [51]	β-delayed γ-ray from ^{195}Os decay
130(1)	129.71(4) [50]	β-delayed γ-ray of ^{195}Ir ground state decay
148.8(2)	Newly found	γ-ray from ^{195}Os isomeric state decay
164.3(2)	164.333(3) [51]	β-delayed γ-ray from ^{195}Os decay
168.8(2)	Newly found	γ-ray from ^{195}Os isomeric state decay
175.2(1)	175.222(2) [51]	β-delayed γ-ray from ^{195}Os decay
178.4(2)	178.529(4) [51]	β-delayed γ-ray from ^{195}Os decay
217.6(4)	217.340(4) [51]	β-delayed γ-ray from ^{195}Os decay
233.8(3)	233.512(4) [51]	β-delayed γ-ray from ^{195}Os decay
252.7(3)	252.685(4) [51]	β-delayed γ-ray from ^{195}Os decay
279.0(2)	Newly found	γ-ray from ^{195}Os isomeric state decay
286.4(1)	286.516(4) [51]	β-delayed γ-ray from ^{195}Os decay
305.1(3)	Newly found	β-delayed γ-ray from ^{195}Os decay
343.6(3)	342.854(7) [51]	β-delayed γ-ray from ^{195}Os decay
347.3(5)	347.45(3) [51]	β-delayed γ-ray from ^{195}Os decay
359.4(4)	359.445(4) [51]	β-delayed γ-ray from ^{195}Os decay
405(1)	406.574(7) [51]	β-delayed γ-ray from ^{195}Os decay
411.7(2)	412.033(6) [51]	β-delayed γ-ray from ^{195}Os decay
428.2(2)	429.629(7) [51]	β-delayed γ-ray from ^{195}Os decay
489.6(3)	489.50(3) [51]	β-delayed γ-ray from ^{195}Os decay
539.1(3)	539.212(23) [51]	β-delayed γ-ray from ^{195}Os decay
543.1(3)	542.52(21) [51]	β-delayed γ-ray from ^{195}Os decay
583(2)	581.792(13) [51]	β-delayed γ-ray from ^{195}Os decay
601.1(4)	600.86(4) [51]	β-delayed γ-ray from ^{195}Os decay
776.2(4)	Newly found	β-delayed γ-ray from ^{195}Os decay

The coincident event numbers of X-rays and γ-rays with the MSPGC under the different conditions could be changed due to different kind of trigger events of the MSPGC, i.e., β-rays, internal conversion electrons and X-rays. FIG. 3.3.2 (c) shows intensity ratios of X-rays and γ-rays for the hit pattern, "M = 2" to "$M \geq 1$". The K X-rays are shown by open stars for iridium (blue) and osmium (red), respectively. The γ-rays assumed to be originated to the β-decays of ^{195}Os and to the isomeric decays of ^{195}Os are indicated by blue and red circles, respectively. An averaged ratio for blue data points (Group A) is 0.58(6). This result agrees with an expected ratio of 0.64(7) from absolute β-ray detection efficiencies at $Q_\beta \approx 2$ MeV of the MSPGC as shown in FIG. 2.3.1 (c), indicating they are associated with β-decays. An averaged intensity ratio for red data points (Group B) is 0.17(3), which is smaller than the value for Group A, indicating that they are originated from different kinds of detected events of the MSPGC. When X-rays and/or internal conversion electrons (ICE's) hit the MSPGC, their detection efficiencies under the "M = 2" hit pattern become relatively low due to their low energies compared to the energetic β-rays. It supports that these newly observed γ-rays of Group B (111.0, 148.8, 168.8 and 279.0 keV) are considered to be originated from the isomeric state of ^{195}Os.

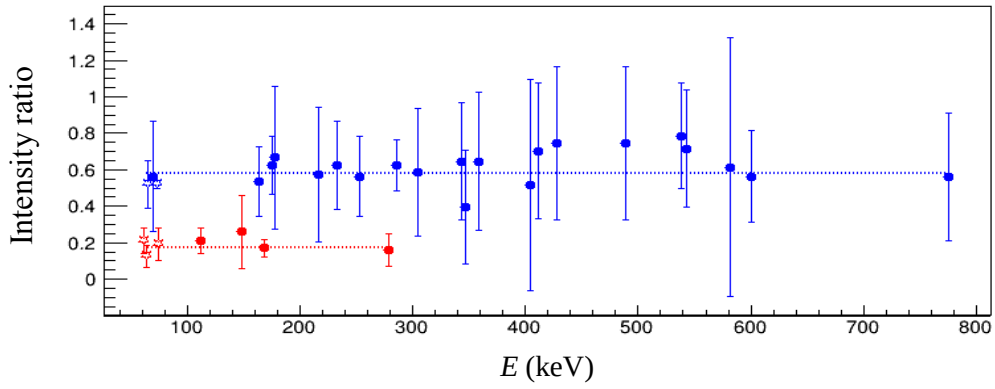

FIG. 3.3.2 (c) Intensity ratios of X-rays and γ-rays in coincidence with the hit pattern "M = 2" to the "$M \geq 1$". The K X-rays are shown by open stars for iridium (blue) and osmium (red), respectively. The γ-rays assumed to be originated to the β-decays of ^{195}Os and to the isomeric decays of ^{195}Os are indicated by blue and red circles, respectively.

3.3.3 Lifetime analysis of γ-transitions

Origins of γ-transitions can be confirmed by analyzing their lifetimes. A distribution of timing signals of each γ-transition from the beam-on timing can be fitted by the growth- and decay-curves with an appropriate lifetime relevant to this transition. FIG. 3.3.3 (a) and (b) show the time spectra for the K X-rays of iridium, 64.8 and 73.4 keV, and 18 γ-ray transitions which are supposed to be β-delayed γ-transitions of ^{195}Os. The hit pattern "$M = 2$" events were used for K X-rays of iridium and 111.6-keV γ-rays, and the hit pattern "$M \geq 1$" events were used for others to get higher statistics. The red lines indicate the fitted results of growth and decay curves. The employed fitting function *f(t)* is,

$$f(t) = \begin{cases} I\left(1 - e^{-\lambda t}\right) + C & (t < T_s) \\ I\left(1 - e^{-\lambda T_s}\right)e^{-\lambda t} + C & (t > T_s) \end{cases}$$

where T_s is a start timing of the beam-off period, I and C are free parameters related to the implantation rate of ^{195}Os and the background rate in the coincident time spectrum of MSPGC and the SC-HPGe, respectively, and λ is the decay constant defined as

$$\lambda = \frac{\log_e(2)}{T_{1/2}},$$

where $T_{1/2}$ is the half-life, which is a free parameter in the fitting. The fitting results for K X-rays of iridium and 18 γ-transitions including newly found 305- and 776-keV transitions are shown in FIG. 3.3.3 (a) and 3.3.3 (b). The obtained half-lives are summarized in FIG. 3.3.3 (c) as a function of X-ray and γ-ray energies. Blue marks indicate K X-rays of iridium and γ-transitions of 305.1(3) and 776.2(4) keV, and black marks indicate other γ-transitions. All of them agree with the literature value of the half-life of the ^{195}Os ground state, 6.5(11) minutes [28] (shadowed area), within the errors of one standard deviation. The lifetime analyses for 4 γ-transitions with the energies of 405(1), 489.6(3), 582.5(8) and 347.3(5) keV has not been performed, because they have too low statistics to fit the experimental data. However, results of their hit pattern analyses and agreements of the energies with the literature values indicate that they are originated from the β-delayed γ-transitions of ^{195}Os ground state. Thus, the origin of those 22 γ-ray peaks is assigned to the ^{195}Os ground state β-decay.

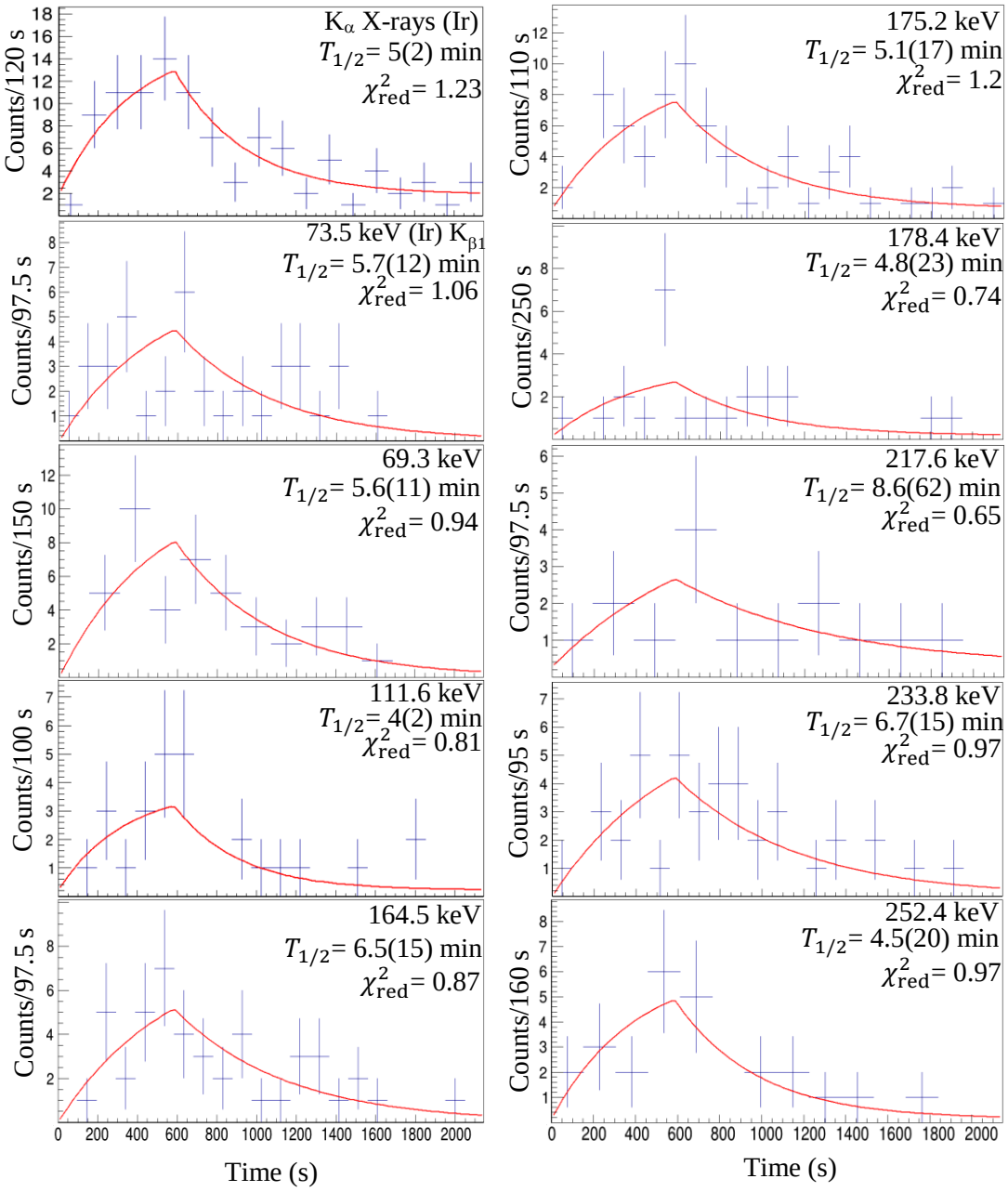

FIG. 3.3.3 (a) Time spectra for K X-rays of iridium, 64.8 and 73.4 keV, 8 γ-transitions measured in the Long run. The hit pattern "$M = 2$" events are used for K X-rays and 111.6 keV γ-rays, and the hit pattern "$M \geq 1$" events are used for others.

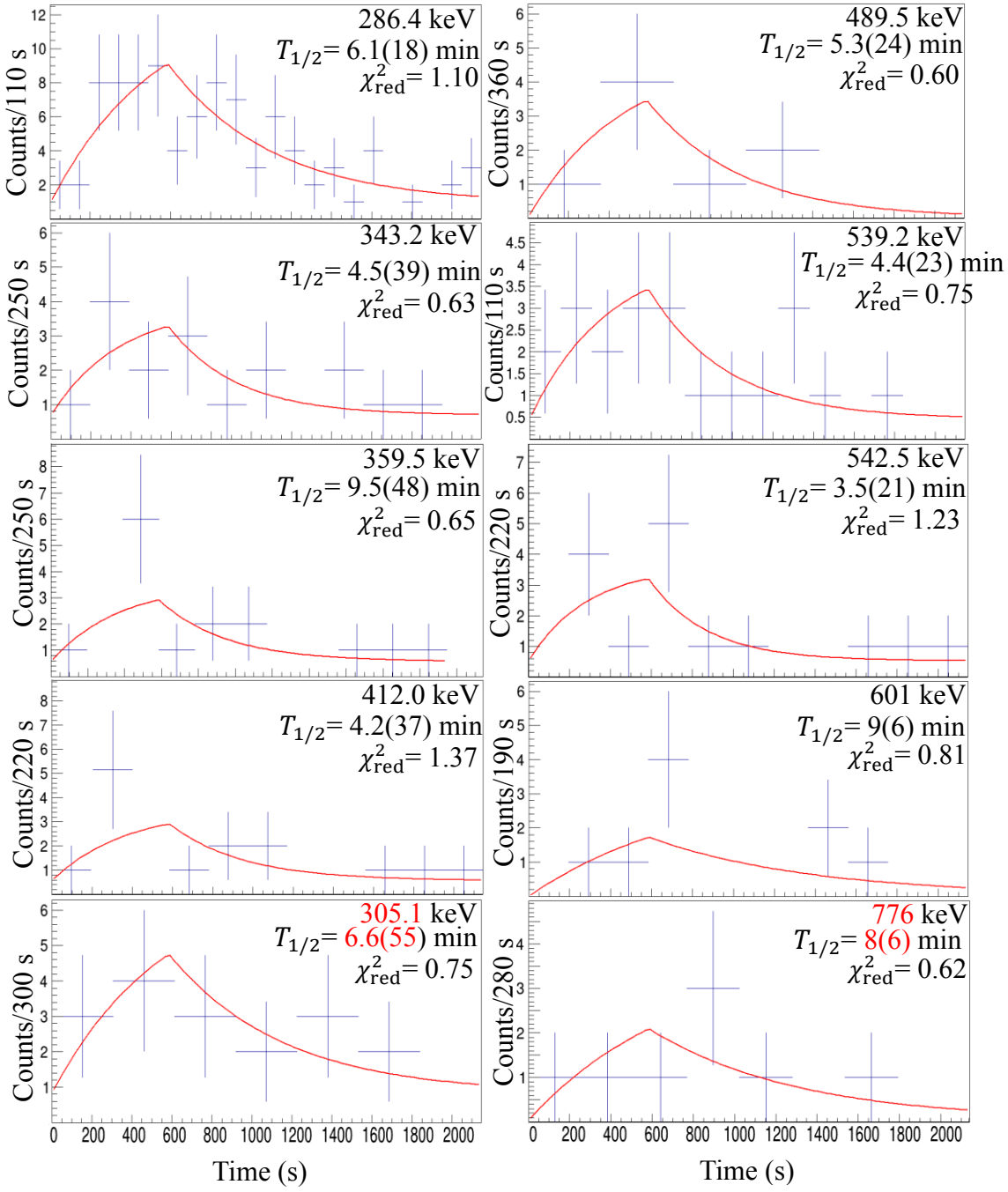

FIG. 3.3.3 (b) Time spectra of 10 γ-transitions measured in the Long run. The hit pattern "$M \geq 1$" events are used. Transitions indicated with energies (keV) in red colors are newly observed in the measurement.

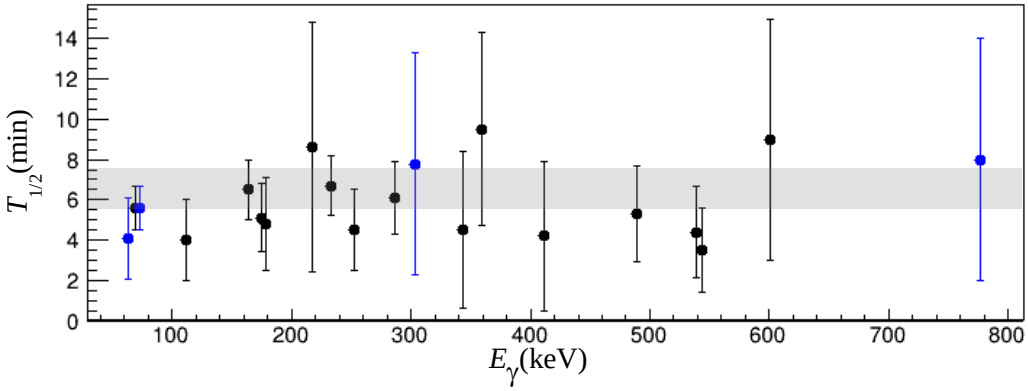

FIG. 3.3.3 (c) Summary of obtained half-lives from FIG. 3.3.3 (a) and (b) as a function of X-ray and γ-ray energies. Blue marks indicate K X-rays of iridium and γ-transitions of 305.1(3) and 776.2(4) keV, and black marks indicate other γ-transitions. Shadowed area indicates the literature value of the half-life of ^{195}Os ground state (6.5 (11) min) [28].

To confirm the origin of other γ-rays, the time distributions of K X-rays of osmium (61.6, 63.1 and 71.4 keV) and 4 γ-transitions (111.0, 148.8, 168.8 and 279.0 keV) were analyzed. Those were measured in the Short run. Since 61.6 and 63.1 keV cannot be separated by the SC-HPGe detectors, single spectrum with an energy gate covering both energies was used for the analysis. FIG. 3.3.3 (d) shows their time spectra with the hit pattern "M = 1" events. The red lines indicate the growth and decay curves obtained by fitting the experimental data in the same procedure of the previous analysis.

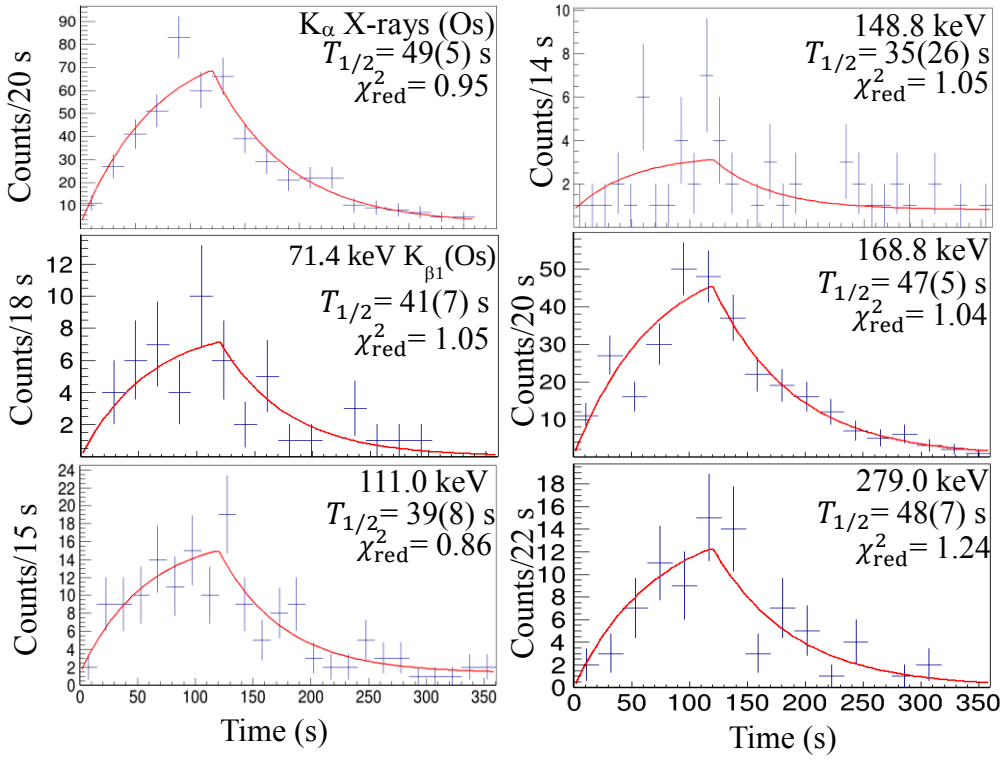

FIG. 3.3.3 (d) Time spectra of osmium K X-rays and 4 γ-transitions measured in the Short run. The hit pattern "M = 1" events are used.

The obtained half-lives are summarized in FIG. 3.3.3 (e) as a function of X-ray and γ-ray energies. They agree with each other within their errors and 4 γ-transitions are identified as transitions decaying from isomeric state of ^{195}Os. The half-life of the isomeric state of ^{195}Os was evaluated by the fitting of a summed spectrum of all timing events of K X-rays and 4 γ-transitions, which is shown in FIG. 3.3.3 (f), resulting to the half-life of 47(3) s.

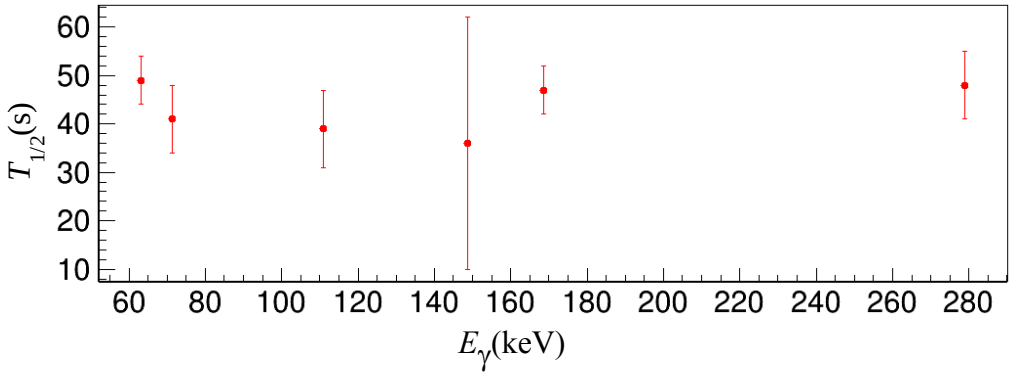

FIG. 3.3.3 (e) Summary of obtained half-lives from FIG. 3.3.3 (d) as a function of X-ray and γ-ray energies.

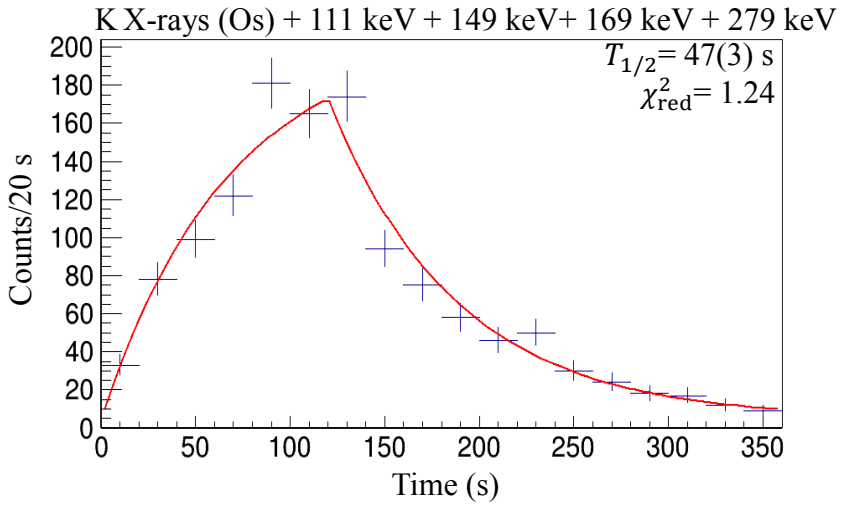

FIG. 3.3.3 (f) The time spectrum summed over the events of K X-rays of osmium and 4 γ-transitions measured in the Short run. The hit pattern "M = 1" events are used.

As for the two remaining γ-transitions with the energies of 98.5(2) and 130(1) keV, and the K X-rays of platinum, which are assumed to be originated from the β-decays of ^{195}Ir, we tried the similar lifetime analysis. FIG. 3.3.3 (g) shows the time spectra for the 98.5-keV γ-rays and the platinum K X-rays with the fitting curves. The resulting half-lives are 1.2(21) hours and 0.5(23) hours for

the X-rays and the γ-rays respectively. Although these values are consistent to the literature value of the half-life, 2.29(17) hours [50], their error are too large to definitely conclude their origins. The further analysis for 130(1)-keV γ-rays was not performed due to the poor statistics.

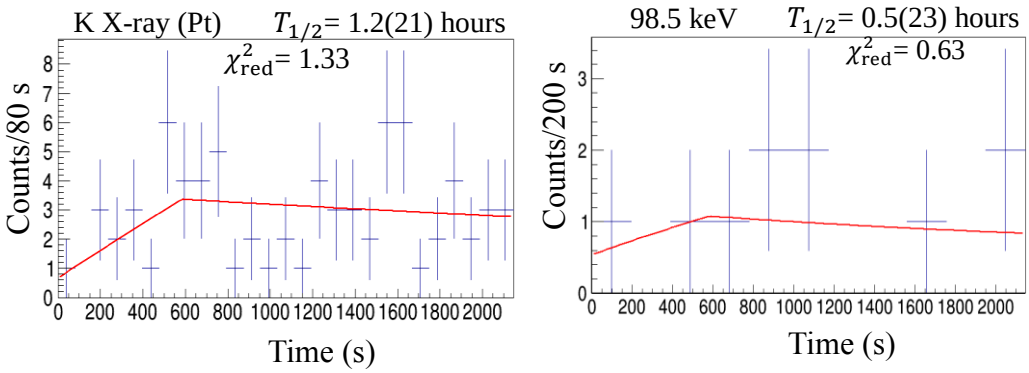

FIG. 3.3.3 (g) Time spectra for the K X-ray of platinum and 98.5 keV γ-transition. The hit pattern "$M = 2$" events measured in the Long run are used.

3.3.4 β-decay scheme of ^{195}Os ground state

From the lifetime evaluation, newly observed γ-rays with the energies of 305.1(3) and 776.2(4) keV were confirmed as β-delayed γ-rays of ^{195}Os ground state. To assign these γ-transitions into the previously reported energy level scheme of ^{195}Ir, the γ-γ coincidence analysis has been performed. FIG. 3.3.4 (a) shows the γ-γ coincidence spectra gated by 305-, 234- and 164-keV γ-rays. Gated by 305-keV γ-rays, γ-ray peaks are found at the energies of 234 and 164 keV. Gated by 234-keV γ-rays, a γ-ray peak is found at the energy of 305 keV. Gated by 164-keV γ-rays, γ-ray peaks are found at the energy of 305 keV and 69 keV. It is known that the γ-transition with the energy of 69 keV corresponds to the γ-decays from the first excited state to the ground state of ^{195}Ir, and it follows the γ-transitions with the energy of 164 keV. Table 3.3.4 (a) summarizes the γ-γ coincidence analysis for 305 keV γ-rays, where coincident γ-rays are marked by ticks. Thus, the 305-keV γ-transition can be assigned between the excited levels at the energies of 539.2 and 233.5 keV of ^{195}Ir as shown in the FIG. 3.3.4 (c) [50].

Table 3.3.4 (a) List of β-delayed γ-ray coincidences for the newly observed 305.1- keV γ-rays and relevant γ-rays. Coincidences of γ-rays are marked by ticks.

Energy (keV)	**305.1**	**233.8**	**164.3**	**69.1**
305.1	gate	✓	✓	
233.8	✓	gate		
164.3	✓		gate	✓

FIG. 3.3.4 (b) shows the γ-γ coincidence spectrum gated by 776-keV γ-rays. No coincident γ-ray peaks are found in the spectrum. It is known that there is an excited level with the energy of 776 keV on ^{195}Ir. The 776 keV γ-transition would be assigned to the direct transition from the 776-keV excited state to the ground state of ^{195}Ir as shown in FIG. 3.3.4 (c).

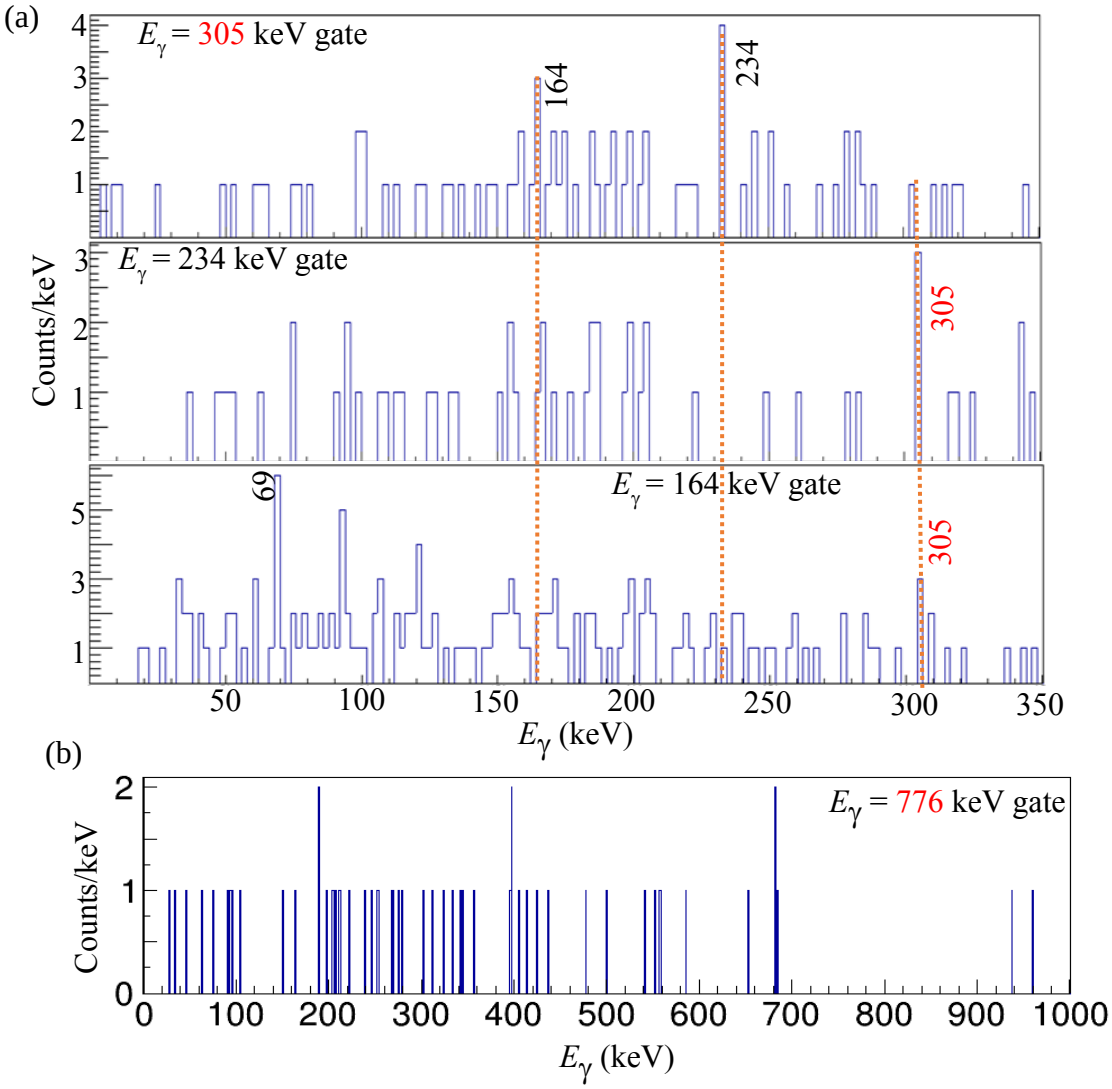

FIG. 3.3.4 (a) γ-γ coincidence spectra gated by 305-, 234- and 164-keV γ-rays and (b) γ-γ coincidence spectrum gated by 776-keV γ-rays.

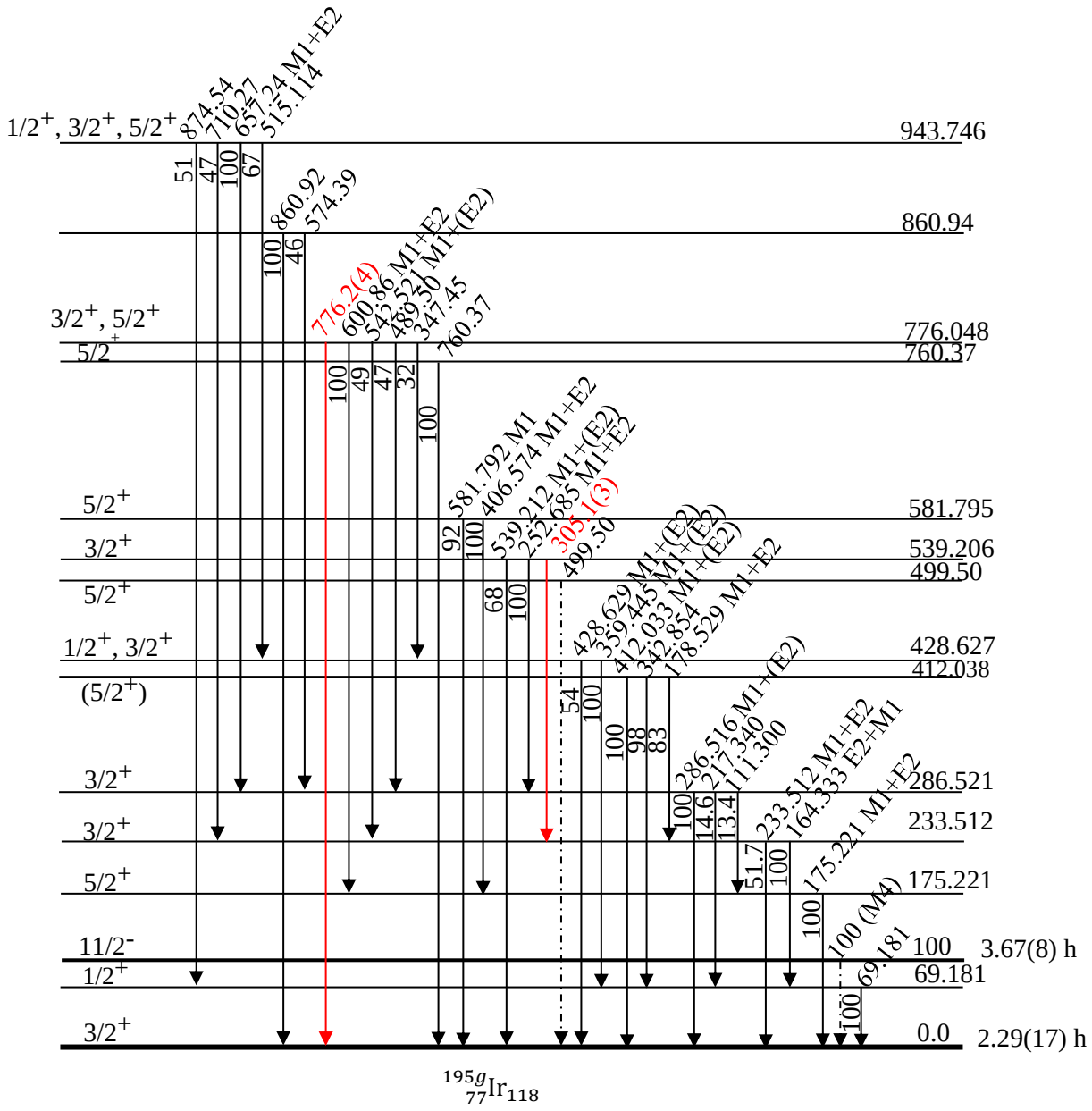

FIG. 3.3.4 (c) Energy levels and γ-decay scheme of ^{195}Ir with newly observed 305.1- and 776.2-keV γ-transitions.

The relative intensities for γ-transitions from each excited level of ^{195}Ir were evaluated with the MSPGC hit pattern "M = 2" by considering energy dependence of γ-ray detection efficiencies. The intensity for the most intense γ-transition is normalized to 100 for each excited level as summarized in Table 3.3.4 (b). Among 20 known γ-transitions of ^{195}Ir, 18 γ-ray intensities give a good agreement with the literature values within the error of one standard deviation [50, 51]. 2 γ-ray intensities for 539.1(3) and 543.1(3) keV are deviated from the literature values by twice of standard deviations.

Table 3.3.4 (b) Summary of β-delayed γ-rays in coincident with the MSPGC (hit pattern "M = 2"). The relative intensities for γ-transitions from each excited level of ^{195}Ir measured in the previous measurement [51, 50] are cited.

Energy level of ^{195}Ir (keV)	E_γ (KeV)	Relative intensities from each level	
		Measured	Literature value [50]
69.181(1)	69.3(2)	100	100
175.222(2)	175.2(1)	100	100
233.512(4)	164.3(2)	100	100
	233.8(3)	85(30)	51.7(25)
286.516(4)	111.6(2)	13(4)	13.4(12)
	217.6(4)	11(6)	14.6(12)
	286.4(1)	100	100
412.038(6)	178.4(2)	96(46)	83(6)
	343.6(3)	107(43)	98(4)
	411.7(3)	100	100
428.629(7)	359.4(4)	100	100
	428.2(1)	50(31)	54(2)
539.212(23)	252.7(3)	100	100
	539.1(3)	140(40)	68(11)
	305.1(3)	53(27)	-
581.792(13)	405(1)	100	100
	582.5(8)	76(70)	92(17)
776.053(14)	347.3(5)	9.3(93)	32(4)
	489.6(3)	69(29)	47(4)
	543.1(3)	107(38)	49(6)
	601.1(4)	100	100
	776.2(4)	51(27)	-

3.3.5 Coincidence analysis of γ-rays associated with the isomeric decay of ^{195}Os

The γ-γ coincidence analysis was performed for 4 γ-transitions with energies of 111.0(1), 148.8(2), 168.8(2) and 279.0(2) keV, associated with the isomeric decay of ^{195}Os. FIG. 3.3.5 (a) shows the γ-γ coincidence spectra gated by 169.0-, 111.0-, 149- and 279-keV γ-rays. All spectra show peaks of 63.0 keV $K_{\alpha 1}$ and 71.4 keV $K_{\beta 1}$ X-rays of osmium, giving the evidence that these four γ-transitions belong to ^{195}Os. Gated by 169.0-keV γ-rays, γ-ray peaks are found at the energies of 111.0 and 149 keV. Gated by 111.0-keV γ-rays, 169.0-and 149.0-keV γ-ray peaks are found. Gated by 149.0-keV γ-rays, γ-ray peaks are found at the energies of 111.0, 169.0, and 279.0 keV. Gated by 279-keV γ-rays, a γ-ray peak is found at the energy of 149 keV. Table 3.3.5 summarizes the γ-γ coincidence analysis, where coincident γ-rays are marked by ticks. Based on those coincidence information, FIG. 3.3.5 (b) was constructed as a possible level scheme of ^{195}Os populated by γ-transitions from the isomeric state. An excited energy of the isomeric state would be 428.8(3) keV, if no transitions exist between 149-keV state and the ground state.

Table 3.3.5 List of γ-ray coincidences among 169.0-, 111.0-, 149.0- and 279.0-keV γ-rays. Coincidence of γ-rays are marked by ticks.

Energy (keV)	**169.0**	**111.0**	**149.0**	**279.0**
169.0	gate	✓	✓	
111.0	✓	gate	✓	
149.0	✓	✓	gate	✓
279.0			✓	gate

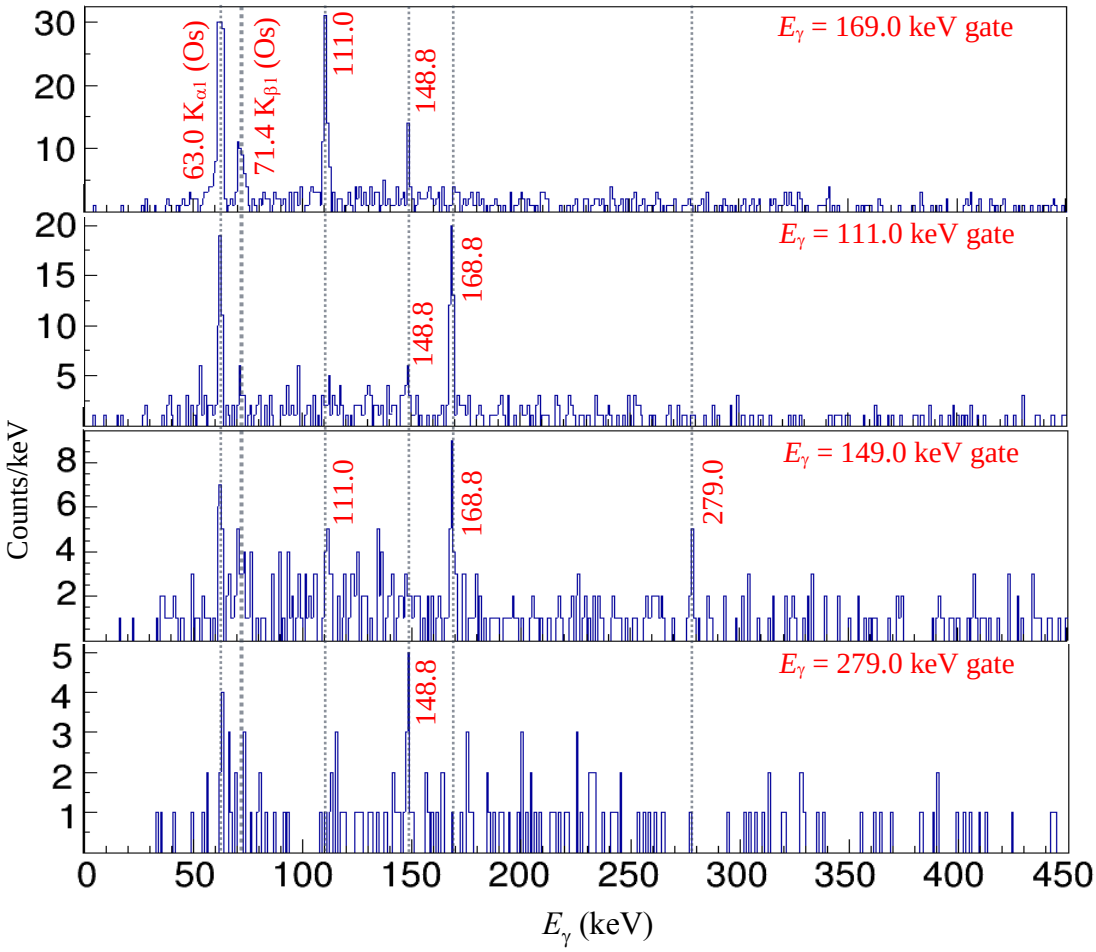

FIG. 3.3.5 (a) γ-γ coincidence spectra gated by 169.0-, 111.0-, 149.0- and 279.0-keV γ-rays.

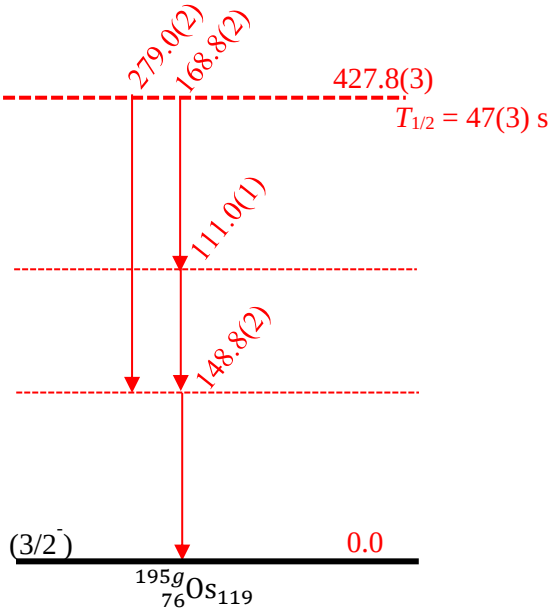

FIG. 3.3.5 (b) A possible level scheme of ^{195}Os.

4 Discussion

4.1 β-decay branching ratios of ^{195}Os ground state

The β-decay branching ratio for the i^{th} state of the daughter nucleus is a ratio of the number of β-decays to populate the i^{th} state to the total number of β-decays. The number of β-decays to populate the i^{th} state can be evaluated as a difference of the number of decays from the i^{th} state to the lower-energy states and the number of decays from the higher-energy states to the i^{th} state via γ-transitions or internal conversions, if the i^{th} state is not the ground state. FIG. 4.1 indicates the schematic view of the ^{195}Os β-decay scheme. In the β-γ coincidence measurements, the number of decays by γ-transitions and internal conversions from the i^{th} state to the j^{th} state, N_{ij}, is evaluated as,

$$N_{ij} = \frac{1}{\varepsilon_{\beta_i} \times \varepsilon_{\gamma_{ij}}} \times N_{\gamma_{ij}}^{\det}\left(1 + \alpha_{ij}\right),$$

where ε_{β_i} is β-ray detection efficiency for the β-decay to populate the i^{th} state, $\varepsilon_{\gamma_{ij}}$ is γ-ray detection efficiency for the γ-transition from the i^{th} state to the j^{th} state, $N_{\gamma_{ij}}^{\det}$ is number of detected events of the γ-transitions from the i^{th} state to the j^{th} state in the measurement, and α_{ij} is internal conversion coefficient for the transition from the i^{th} state to the j^{th} state. The total number of β-decays in the measurement, N_{β_i}, is

$$N_{\beta_i} = \sum_i \frac{1}{\varepsilon_{\beta_i}} \times N_{\beta_i}^{\det},$$

where $N_{\beta_i}^{\det}$ is the number of detected events of β-decays which populate the i^{th} state. Thus the β-decay branching ratio for the i^{th} state, I_{β_i}, is expressed as,

$$I_{\beta_i} = \frac{\sum_j \frac{1}{\varepsilon_{\beta_i} \times \varepsilon_{\gamma_{ij}}} \times N_{\gamma_{ij}}^{\det}\left(1 + \alpha_{ij}\right) - \sum_k \frac{1}{\varepsilon_{\beta_k} \times \varepsilon_{\gamma_{ki}}} \times N_{\gamma_{ki}}^{\det}\left(1 + \alpha_{ki}\right)}{\sum_i \frac{1}{\varepsilon_{\beta_i}} \times N_{\beta_i}^{\det}}. \quad \ldots.(4.1)$$

The Q-value of the β-decay, Q_β, from the ground state of ^{195}Os to the ground state of ^{195}Ir is 2180(6) keV. As the maximum energy of the excited states of ^{195}Ir populated in the measurement is 776 keV, Q_β ranges from 1404 keV to 2180 keV depending on the populated excited states of ^{195}Ir. The β-ray detection efficiency of the MSPGC is varied from 0.46(4) to 0.50(4) for the hit pattern "$M = 2$" in this range of Q_β as shown in FIG. 2.3.1 (a). Because the variation of the efficiency is small, the efficiency can be treated to be a constant value ε_β within estimated errors,

$\varepsilon_{\beta_i} \approx \varepsilon_\beta$ for any i.

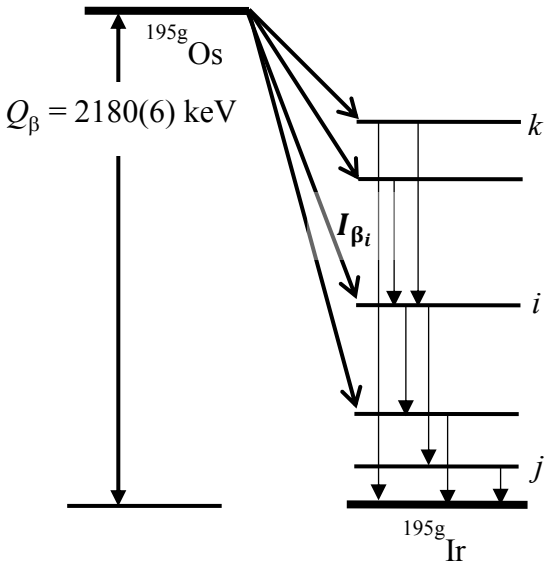

FIG. 4.1 Schematic view of ^{195}Os β-decay scheme.

Now the equation (4.1) is reduced to,

$$I_{\beta_i} \approx \frac{\sum_j \frac{1}{\varepsilon_{\gamma_{ij}}} \times N_{\gamma_{ij}}^{\det}\left(1+\alpha_{ij}\right) - \sum_k \frac{1}{\varepsilon_{\gamma_{ki}}} \times N_{\gamma_{ki}}^{\det}(1+\alpha_{ki})}{\sum_i N_{\beta_i}^{\det}} \ldots\ldots (4.2)$$

$$= \frac{\sum_j \frac{1}{\varepsilon_{\gamma_{ij}}} \times N_{t_{ij}}^{\det} - \sum_k \frac{1}{\varepsilon_{\gamma_{ki}}} \times N_{t_{ki}}^{\det}}{N_\beta^{\det}} \ldots\ldots\ldots (4.3)$$

where $N_\beta^{\det} = \sum_i N_{\beta_i}^{\det}$ and $N_{t_{ij}}^{\det} = N_{\gamma_{ij}}^{\det}\left(1+\alpha_{ij}\right)$. $N_\beta^{\det}$ indicates a total number of detected events of β-decays. In the following sections, $N_{t_{ij}}^{\det}$ and $N_\beta^{\det}$ are evaluated.

4.1.1 Evaluation of $N_{t_{ij}}^{\det}$

For the evaluation of $N_{t_{ij}}^{\det}$, the information of the conversion coefficients is necessary. Table 4.1.1 summarizes 22 β-delayed transitions with the energies (E_i and E_f) and spin-parities (J_i^π and J_f^π) of the initial and final states, γ-ray energies (E_γ), numbers of detected γ-rays ($N_\gamma^{\det}$), multipolarities of the

transitions, mixing ratios (δ), conversion coefficients (α) and N_t^{det}. Eight transitions with the energies of 69.3, 111.3, 217.6, 305.1, 343.6, 347.3, 489.6 and 776.2 keV have no literature values of the conversion coefficients. They have been calculated if the multipolarities of the transitions are known [52] and the values are presented in square brackets []. The transition with the energy of 343 keV is described by the same parities and the spin difference of two between the initial and the final states, resulting in a dominant transition of E2. Other transitions are the same parities and the spin differences less or equal to one between the initial and the final states, resulting in the dominant mixed transitions of M1 and E2. Table 4.1.1 shows the conversion coefficients evaluated for two extreme cases of the pure M1 and the pure E2 transitions for them, and their values of N_t^{det} were obtained separately in both cases (left column of N_t^{det} in Table 4.1.1). Except for the transition with the energy of 69.3 keV, those values of N_t^{det} agree each other within their errors. We adopted single values of N_t^{det} and its standard deviation calculated by the following formula,

$$N_t^{det} = \frac{N_{max}^{det} + N_{min}^{det}}{2}, \sigma = \frac{N_{max}^{det} - N_{min}^{det}}{2},$$

where

$$N_{max}^{det} = \begin{cases} N_{M1}^{det} + \sigma_{M1} \left(N_{M1}^{det} + \sigma_{M1} \geq N_{E2}^{det} + \sigma_{E2} \right) \\ N_{E2}^{det} + \sigma_{E2} \left(N_{M1}^{det} + \sigma_{M1} < N_{E2}^{det} + \sigma_{E2} \right) \end{cases}$$

and

$$N_{min}^{det} = \begin{cases} N_{M1}^{det} - \sigma_{M1} \left(N_{M1}^{det} - \sigma_{M1} \leq N_{E2}^{det} - \sigma_{E2} \right) \\ N_{E2}^{det} - \sigma_{E2} \left(N_{M1}^{det} - \sigma_{M1} > N_{E2}^{det} - \sigma_{E2} \right) \end{cases}$$

In the above formulae, N_{M1}^{det} (N_{E2}^{det}) and σ_{M1} (σ_{E2}) indicate the evaluated $N_t^{det}$and its standard deviation for the case of M1 (E2) transition, respectively (right column of Table 4.1.1). This method gives minimum errors which are enough large to cover the lower and upper edges of limitation in both pure M1 and E2 transitions in terms of their standard deviations. For the 69.3-keV transition, both values of N_t^{det} in two extreme cases do not overlap each other within their standard deviations. We consider those values separately as the maximum and minimum for the possible range of its value.

Table 4.1.1 Summary of β-delayed γ-rays in coincidence with the MSPGC hit pattern "*M* = 2". Energies of initial and final state ($\boldsymbol{E_i}$ and $\boldsymbol{E_f}$), spin-parities of initial and final state $\boldsymbol{J_i^\pi}$ and $\boldsymbol{J_f^\pi}$), measured γ-ray energies ($\boldsymbol{E_\gamma}$), numbers of detected γ-rays ($\boldsymbol{N_\gamma^{det}}$), the multipolarities of the transitions, mixing ratios ($\boldsymbol{\delta}$), the conversion coefficients ($\boldsymbol{\alpha}$) and the evaluated $\boldsymbol{N_t^{det}}$are indicated.

E_i (keV)	J_i^π	E_f (keV)	J_f^π	E_γ (keV)	N_γ^{det}	Multi-polarity	δ	α**	$N_t^{det} = N_\gamma^{det}(1+\alpha)$	
										Pure M1&E2 combined
69.18(1)	$1/2^+$	0.0	$3/2^+$	69.3(2)	16(6)	[M1]*		[3.17(15)]	70(25)	
						[E2]*		[22.4(17)]	400(140)	
175.22(2)	$5/2^+$	0.0	$3/2^+$	175.2(1)	35(6)	M1+E2	0.47(3)	1.117(21)	70(13)	
233.512(4)	$3/2^+$	69.18(1)	$1/2^+$	164.3(2)	19(5)	E2+M1	1.6(3)	0.91(8)	36(10)	
		0.0	$3/2^+$	233.8(3)	15(5)	M1+E2	0.26(55)	0.54(12)	23(8)	
286.516(4)	$3/2^+$	175.22(2)	$5/2^+$	111.6(2)	14(4)	[M1]*		[4.43(13)]	40(16)	37(19)
						[E2]*		[2.92(12)]	30(12)	
		69.18(1)	$1/2^+$	217.6(4)	6(3)	[M1]*		[0.675(13)]	10(5)	10(6)
						[E2]*		[0.259(6)]	8(4)	
		0.0	$3/2^+$	286.4(1)	52(8)	M1+(E2)	0.43(5)	0.286(8)	70(10)	
412.038(6)	$(5/2)^+$	233.512(4)	3/2+	178.4(2)	9(4)	M1+E2	0.47(+25-33)	1.06(11)	19(8)	
		69.18(1)	$1/2^+$	343.6(3)	8(3)	[E2]*		[0.0637(11)]	9(3)	
		0.0	$3/2^+$	411.7(3)	7(3)	M1+(E2)	0.22(58)	0.12(3)	8(3)	
428.6(7)	$1/2^+$, $3/2^+$	69.18(1)	$1/2^+$	359.4(4)	7(3)	M1+(E2)	< 0.39	0.165(8)	8(4)	
		0.0	$3/2^+$	428.2(1)	7(3)	M1+(E2)	< 0.72	0.095(13)	8(3)	
539.21(2)	$3/2^+$	286.516(4)	$3/2^+$	252.7(3)	14(4)	M1+E2	1.5(33)	0.25(19)	18(6)	
		0.0	$3/2^+$	539.1(3)	15(4)	M1+(E2)	< 0.56	0.054(5)	16(4)	
		233.512(4)	[$3/2^+$]	[305.1(3)]	7(4)	[M1]*		[0.269(5)]	9(5)	9(5)
						[E2]*		[0.0903(16)]	8(4)	
581.79(12)	$5/2^+$	175.22(2)	$5/2^+$	405(1)	3(2)	M1		0.1241	3(2)	
		0.0	$3/2^+$	582.5(8)	2(1)	M1		0.0484	2(1)	
776.048 (14)	$3/2^+$, $5/2^+$	428.6(7)	$1/2^+$, $3/2^+$	347.3(5)	1(1)	[M1]*		[0.188(3)]	1(1)	1(1)
						[E2]*		[0.0617(10)]	1(1)	
		286.516(4)	$3/2^+$	489.6(3)	7(3)	[M1]*		[0.0758(12)]	8(3)	8(4)
						[E2]*		[0.0250(4)]	7(3)	
		233.512(4)	$3/2^+$	543.1(3)	10(5)	M1+(E2)	< 0.51	0.054(4)	11(5)	
		175.22(2)	$5/2^+$	601.1(4)	9(3)	M1+E2	0.62(66)	0.036(12)	9(3)	
		0.0	[$3/2^+$]	[776.2(4)]	4(2)	[M1]*		[0.0231(4)]	4(2)	4(2)
						[E2]*		[0.00875(13)]	4(2)	
			* for pure M1 and E2 transition ** [ ] indicates an estimated value based on Ref. [52]							

4.1.2 Evaluation of N_{β}^{det}

From the analyses described in the Section 3.3, we observed the isomeric state of ^{195}Os (^{195m}Os), which deexcites to the ground state of Os (^{195g}Os). Both ^{195m}Os and ^{195g}Os are produced and extracted at the KISS and are implanted to the aluminized Mylar tape. FIG. 4.1.2 (a) shows a schematic view of the decay sequence from the implanted ^{195}Os. ^{195m}Os decays to ^{195g}Os through the cascade transitions as shown in FIG. 3.3.5 (b) with the half-life of 47(3) s. ^{195g}Os decays to ^{195}Ir with the half-life of 6.5(11) minutes and the ground state of ^{195}Ir (^{195g}Ir) is populated after several transitions. ^{195g}Ir is also radioactive and decays to the stable nucleus ^{195}Pt with a half-life 2.29(17) hours.

To evaluate N_{β}^{det}, such decay sequence has to be considered in the pulsed-beam measurements. FIG. 4.1.2 (b) shows the time spectrum of the events detected by the MSPGC with the hit pattern "M = 2" in the Long run. It is considered to be contributed by the conversion electrons associated with the ^{195m}Os decay, the β-rays from the ^{195g}Os and ^{195g}Ir, and the background events.

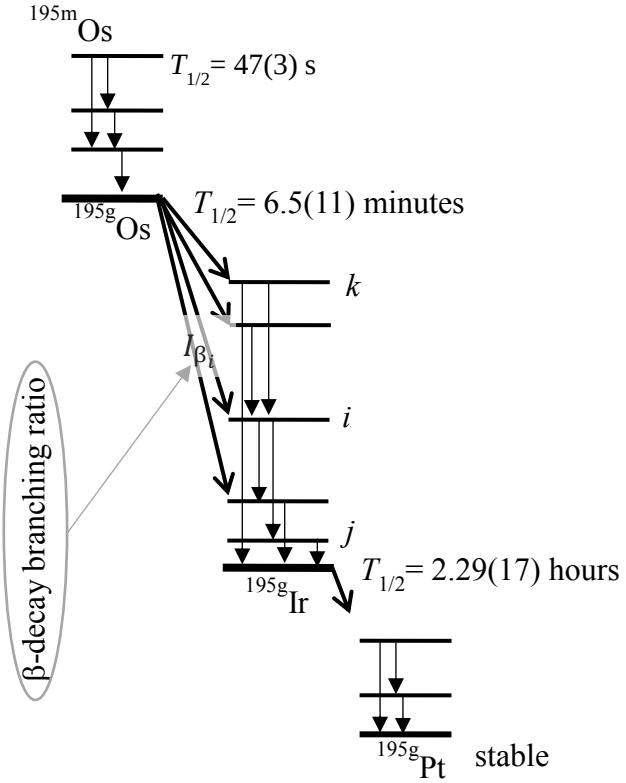

FIG. 4.1.2 (a) Schematic view of decay sequence from ^{195}Os.

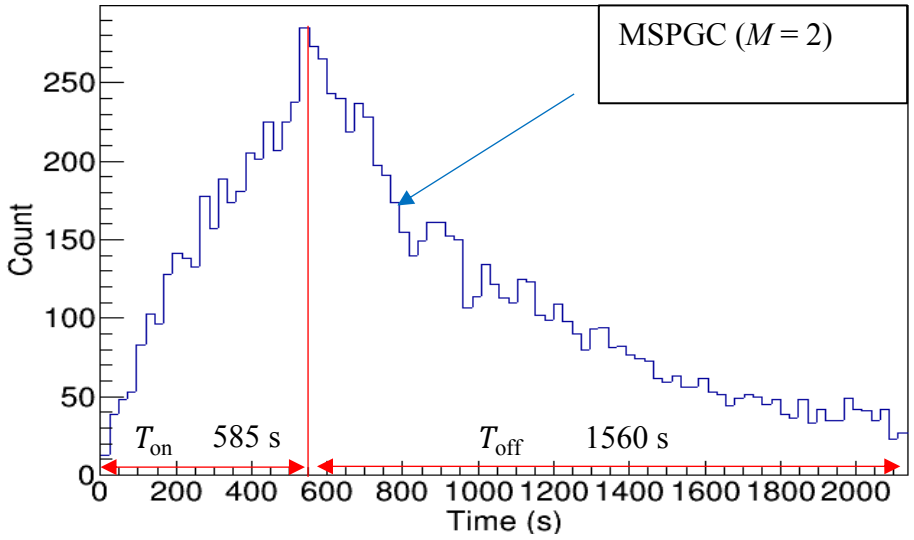

FIG. 4.1.2 (b) Time spectrum of the events detected by the MSPGC with hit pattern "$M = 2$" in the Long run measurement.

Considering those contributions, the time spectrum is fitted by the function of the calculated detection rate, $f(t)$,

$$f(t) = C_{\mathrm{N}} \times [\varepsilon_{\mathrm{m}} R_{\mathrm{m}}(t) + \varepsilon_{\mathrm{Os}} R_{\mathrm{Os}}(t) + \varepsilon_{\mathrm{Ir}} R_{\mathrm{Ir}}(t) + R_{\mathrm{B.G}}], \quad \ldots\ldots\ldots\ldots \quad (4.4)$$

where t is a time from the beam-on, C_{N} is a number of cycles in the measurement, $R_{\mathrm{m}}(t)$, $R_{\mathrm{Os}}(t)$ and $R_{\mathrm{Ir}}(t)$ are the radiation rates of $^{195\mathrm{m}}$Os decay, the $^{195\mathrm{g}}$Os decay and $^{195\mathrm{g}}$Ir decay at the time t, respectively. $R_{\mathrm{B.G}}$ is a constant background rate, $\varepsilon_{\mathrm{Os}}$ and $\varepsilon_{\mathrm{Ir}}$ are the β-ray detection efficiencies of $^{195\mathrm{g}}$Os and $^{195\mathrm{g}}$Ir decay, respectively, and ε_{m} is a number of detected events per one decay of $^{195\mathrm{m}}$Os. $R_{\mathrm{m}}(t)$, $R_{\mathrm{Os}}(t)$ and $R_{\mathrm{Ir}}(t)$ are expressed as,

$$R_{\mathrm{m}}(t) = \lambda_{\mathrm{m}} N_{\mathrm{m}}(t),\ R_{\mathrm{Os}}(t) = \lambda_{\mathrm{Os}} N_{\mathrm{Os}}(t) \text{ and } R_{\mathrm{Ir}}(t) = \lambda_{\mathrm{Ir}} N_{\mathrm{Ir}}(t),$$

where $N_{\mathrm{m}}(t)$, $N_{\mathrm{Os}}(t)$ and $N_{\mathrm{Ir}}(t)$ are numbers of the $^{195\mathrm{m}}$Os, $^{195\mathrm{g}}$Os and $^{195\mathrm{g}}$Ir nuclei on the tape at the time t, respectively, and λ_{m}, λ_{Os} and λ_{Ir} are decay constants of $^{195\mathrm{m}}$Os, $^{195\mathrm{g}}$Os and $^{195\mathrm{g}}$Ir decays, respectively, which are expressed as,

$$\lambda_{\mathrm{m}} = \frac{\log_{\mathrm{e}}(2)}{T_{1/2}^{\mathrm{m}}},\ \lambda_{\mathrm{Os}} = \frac{\log_{\mathrm{e}}(2)}{T_{1/2}^{\mathrm{Os}}} \text{ and } \lambda_{\mathrm{Ir}} = \frac{\log_{\mathrm{e}}(2)}{T_{1/2}^{\mathrm{Ir}}},$$

where $T_{1/2}^{\mathrm{m}}$, $T_{1/2}^{\mathrm{Os}}$ and $T_{1/2}^{\mathrm{Ir}}$ are the half-lives of the $^{195\mathrm{m}}$Os, $^{195\mathrm{g}}$Os and $^{195\mathrm{g}}$Ir, respectively.

Now, we introduce I_{m} and I_{Os} for the implantation rates of $^{195\mathrm{m}}$Os and $^{195\mathrm{g}}$Os to the tape, respectively, and the following differential equations are obtained.

$$\left.\begin{array}{ll}
\frac{dN_{\mathrm{m}}(t)}{dt} = \begin{cases} -\lambda_{\mathrm{m}} N_{\mathrm{m}}(t) + I_{\mathrm{m}} & (0 \le t \le T_{\mathrm{on}}) \\ -\lambda_{\mathrm{m}} N_{\mathrm{m}}(t) & (T_{\mathrm{on}} \le t \le T_{\mathrm{on}} + T_{\mathrm{off}}) \end{cases} \\
\frac{dN_{\mathrm{Os}}(t)}{dt} = \begin{cases} -\lambda_{\mathrm{Os}} N_{\mathrm{Os}}(t) + \lambda_{\mathrm{m}} N_{\mathrm{m}}(t) + I_{\mathrm{Os}} & (0 \le t \le T_{\mathrm{on}}) \\ -\lambda_{\mathrm{Os}} N_{\mathrm{Os}}(t) + \lambda_{\mathrm{m}} N_{\mathrm{m}}(t) & (T_{\mathrm{on}} \le t \le T_{\mathrm{on}} + T_{\mathrm{off}}) \end{cases} \\
\frac{dN_{\mathrm{Ir}}(t)}{dt} = \begin{cases} -\lambda_{\mathrm{Ir}} N_{\mathrm{Ir}}(t) + \lambda_{\mathrm{Os}} N_{\mathrm{Os}}(t) & (0 \le t \le T_{\mathrm{on}}) \\ -\lambda_{\mathrm{Ir}} N_{\mathrm{Ir}}(t) + \lambda_{\mathrm{Os}} N_{\mathrm{Os}}(t) & (T_{\mathrm{on}} \le t \le T_{\mathrm{on}} + T_{\mathrm{off}}) \end{cases}
\end{array}\right\}, .. (4.5)$$

where T_{on} and T_{off} are beam-on and beam-off period, respectively. $f(t)$ is obtained by solving those differential equations. The fitting time spectrum is expressed as,

$$N_i^{\mathrm{cal}} = C_{\mathrm{N}} \times \int_{t_i^{\mathrm{l}}}^{t_i^{\mathrm{u}}} f(t)\, dt \ldots\ldots (4.6)$$

where N_i^{cal} is the content at the i^{th} bin of the fitting time spectrum, and t_i^{l} and t_i^{u} are the lower and the upper edges of the i^{th} bin, respectively. The detailed expression of N_i^{cal} is shown in Appendix A1.

The measured time spectrum is fitted with equation (4.6) by applying a minimum chi-square method. There are totally 10 parameters, C_{N}, ε_{m}, $\varepsilon_{\mathrm{Os}}$, $\varepsilon_{\mathrm{Ir}}$, $R_{\mathrm{B.G}}$, $T_{1/2}^{\mathrm{m}}$, $T_{1/2}^{\mathrm{Os}}$, $T_{1/2}^{\mathrm{Ir}}$, I_{m} and I_{Os}. C_{N} is 2 for the Long run. The $\varepsilon_{\mathrm{Os}}$, $\varepsilon_{\mathrm{Ir}}$, $T_{1/2}^{\mathrm{m}}$ and $T_{1/2}^{\mathrm{Ir}}$ are kept to be fixed values. The $\varepsilon_{\mathrm{Os}}$ and $\varepsilon_{\mathrm{Ir}}$ are 0.51 for $Q_{\beta}(\mathrm{Os})$ = 2180(6) keV and 0.41 for $Q_{\beta}(\mathrm{Ir})$ = 1101.6(13) keV, respectively, the $T_{1/2}^{\mathrm{m}}$ is 47(3) s and $T_{1/2}^{\mathrm{Ir}}$ is 2.29(17) hours [50]. Four parameters, ε_{m}, $R_{\mathrm{B.G}}$, $T_{1/2}^{\mathrm{Os}}$ and I_{Os} and a parameter $I_{\mathrm{R}} \equiv \frac{I_{\mathrm{m}}}{I_{\mathrm{Os}}}$ instead of I_{m} are treated as free parameters.

FIG. 4.1.2 (c) shows the fitting results. The red, green and blue lines indicate the contributions of $^{195\mathrm{g}}$Os, $^{195\mathrm{m}}$Os and $^{195\mathrm{g}}$Ir decay, respectively. The background events are indicated by the dotted black line. The solid black lines indicate the sum of all contributions. Table 4.1.2 summarizes the obtained fitting parameters. The reduced chi-square, $\chi^2_{\mathrm{red.}}$, of the fitting is 1.03, indicating the goodness of the fitting.

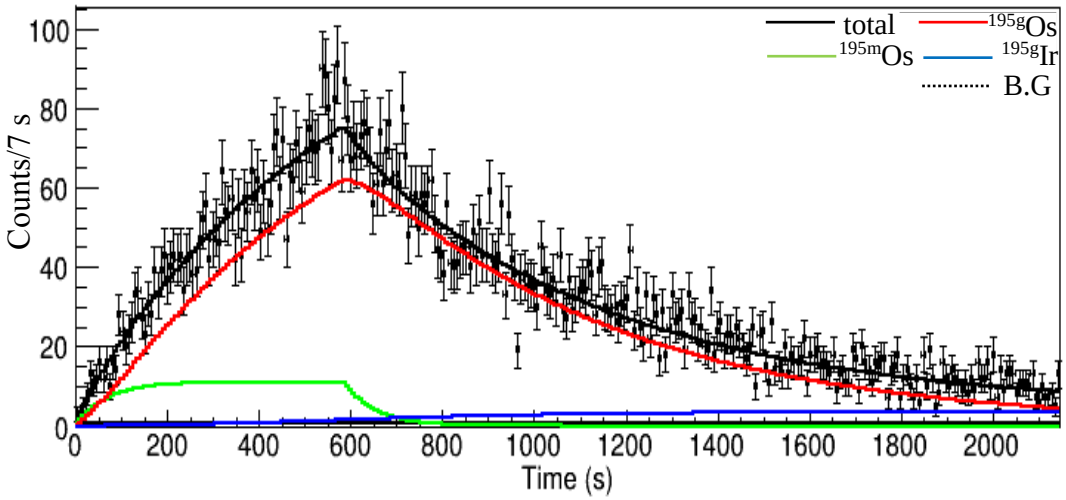

FIG. 4.1.2 (c) Time spectrum for the number of events detected by the MSPGC with the hit pattern "$M = 2$" in the Long run measurement. Black line indicating the fitting result, which consists of four contributions from ^{195m}Os decays (green line), ^{195g}Os decays (red line), ^{195g}Ir decays (blue line) and the constant background (dotted black line).

Table 4.1.2 Summary of fitting result by chi-square minimization.

Parameter	Fitting result
$\boldsymbol{I_{Os}}$	6.3(8) cps
$\boldsymbol{I_{R}}$	1.2(3)
$\boldsymbol{\varepsilon_{m}}$	0.10(2)
$\boldsymbol{T_{1/2}^{Os}}$	6.5(4) minutes
$\boldsymbol{R_{B.G}}$	0.06(4) cps

The fitting gives the half-life of ^{195g}Os, $T_{1/2}^{Os}$, which agrees with the literature value of 6.5(11) minutes [28] with improved precession.

Finally, N_{β}^{det} is calculated as,

$$N_{\beta}^{det} = C_N \times \int_0^{T_{on}+T_{off}} \varepsilon_{Os} R_{Os}(t)\, dt = 8012(1060) \text{ counts}$$

4.1.3 Evaluation of β-decay branching ratios of ^{195}Os ground state decay

The β-decay branching ratios of ^{195g}Os to the excited states of ^{195}Ir are calculated by the formula (4.3). Introducing N_i^{out} and N_i^{in} as,

$$N_i^{\text{out}} = \sum_j \frac{1}{\varepsilon_{\gamma_{ij}}} \times N_{\text{t}_{ij}}^{\text{det}} \text{ and } N_i^{\text{in}} = \sum_k \frac{1}{\varepsilon_{\gamma_{ki}}} \times N_{\text{t}_{ki}}^{\text{det}},$$

respectively, I_{β_i} is expressed as,

$$I_{\beta_i} = \frac{N_i^{\text{out}} - N_i^{\text{in}}}{N_\beta^{\text{det}}}.$$

Table 4.1.3 summarizes the values of N^{out}, N^{in} and I_β for each state of ^{195}Ir. The β-decay branching ratio to the ground state, I_{β_0}, is calculated by the following identical equation,

$$I_{\beta_0} = 1 - \sum_{i \neq 0} I_{\beta_i}.$$

We consider pure M1 and E2 cases separately for the transition from the 69.3(2)-keV state to the ground state. Therefore, different values of I_β were evaluated.

Table 4.1.3 Summary of N^{out}, N^{in} and I_β for each state of ^{195}Ir with the energy of E_x.

E_x (keV)	N^{out}	N^{in}	$N^{\text{out}} - N^{\text{in}}$	I_β(%)
776.048(1)	285(64)	0	285(64)	3.6(9)
581.795(13)	39(21)	0	39(21)	0.5(3)
539.212(23)	322(114)	0	322(114)	4.0(15)
428.672(7)	114(38)	9(9)	105(39)	1.3(5)
412.038(6)	253(70)	0	253(70)	3.2(10)
286.516(4)	795(159)	180(103)	615(189)	7.7(26)
233.512(4)	387(96)	269(84)	118(128)	1.5(16)
175.222(2)	477(100)	354(127)	123(161)	1.5(20)
69.181(1)	700(250)*	436(92)	264(266)*	3.3(33)*~32(16)**
	3000(1200)**		2564(1203)**	
0				45(17)** ~ 73(5)*

*for pure M1 transition; ** for pure E2 transition.

4.1.4 Evaluation of log *ft*

The log *ft* value is useful to study the property of each β-decay channel. It is defined as $\log_{10}(f t_{1/2})$, where *f* is the Fermi integral and $t_{1/2}$ is a partial half-life of each β-decay channel. The log *ft* value is decomposed as,

$$\log_{10}(f t_{1/2}) = \log_{10}(f) + \log_{10}(t_{1/2}), \quad \text{.....(4.6)}$$

and $\log_{10}(f)$ is obtained from the literature [53].

The partial half-life is calculated by

$$t_{1/2} = \frac{T_{\frac{1}{2}}}{I_\beta}, \quad \text{.....(4.7)}$$

where $T_{\frac{1}{2}}$ is the β-decay half-life of ^{195g}Os and I_β is the β-decay branching ratio to the corresponding state of ^{195}Ir. The uncertainty of the partial half-life, $\delta t_{1/2}$, is calculated as,

$$\delta t_{1/2} = \sqrt{(\frac{1}{I_\beta}\delta T_{1/2})^2 + (\frac{T_{1/2}}{I_\beta{}^2}\delta I_\beta)^2}, \quad \text{.....(4.8)}$$

where $\delta T_{1/2}$ and δI_β are uncertainties of β-decay half-life the and β-decay branching ratio, respectively.

FIG. 4.1.4 shows the β-decay scheme of ^{195g}Os including the obtained log *ft* values. The evaluated log *ft* values range from 5.98(4) to 7.63(26) and all of them are within the range of values for the first-forbidden (FF) non-unique transition (spin changes = 0, ± 1, parity changes = yes) [58]. It indicates possible candidate of the spin parity of ^{195g}Os is $3/2^-$ based on reported spin-parities of β-decay final states ($1/2^+, 3/2^+, 5/2^+$). There is no experimental result for the spin-parity of ^{195g}Os, however it was assumed to be $3/2^-$ from the systematics of odd mass nuclei of osmium [20, 50, 60]. It agrees with our result from argument of log *ft* values.

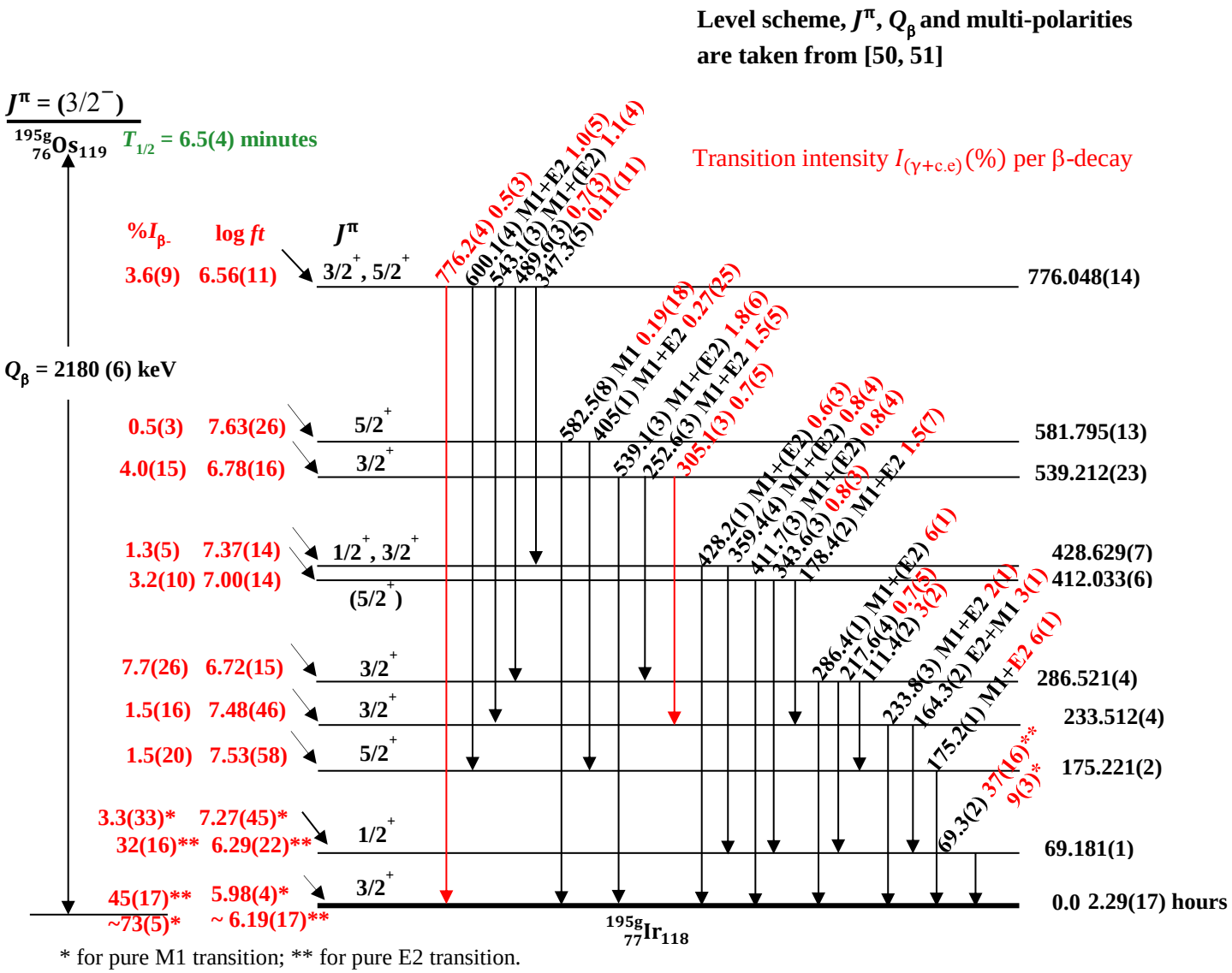

* for pure M1 transition; ** for pure E2 transition.

FIG. 4.1.4 β-decay scheme of ^{195g}Os.

4.2 Statistical study for 98-keV and 130-keV γ-rays

The γ-rays with the energies of 98 keV and 130 keV found in FIG. 3.3.2 (a) are assumed to be originated from β-delayed γ-transitions of ^{195}Ir, which is the daughter nucleus of ^{195}Os. However, the lifetime analysis could not provide the definite conclusion because of its long half-life compared to the measured cycle time as shown in Section 3.3.3. The γ-γ coincidence analysis cannot be applied to them due to their low statistics. Here we have studied the consistency in terms of statistics using the number of β-decays of ^{195}Ir, which is obtained from the fitting results discussed in Section 4.1.

FIG. 4.2 shows the β-decay scheme of ^{195}Ir ground state [50]. The intensities of the 98.83(1)-keV and 129.71(4)-keV γ-transitions are known as 0.099(27) and 0.014(5) per β-decay, respectively. The numbers of detected γ-rays can be evaluated by multiplying the γ-transition intensities and γ-ray detection efficiencies to the number of detected β-rays from the ^{195g}Ir β-decays during the measurement. It is evaluated as,

$$C_{\mathrm{N}} \times \int_0^{T_{\mathrm{on}}+T_{\mathrm{off}}} \varepsilon_{\mathrm{Ir}}\, R_{\mathrm{Ir}}(t)\, dt = 719(130) \text{ counts.}$$

Table 4.2 summarizes a comparison between the calculated number of γ-ray detection (N_γ^{cal}) and number of detected γ-rays in the measurement (N_γ^{det}) for the 98.5(2)-keV and 130(1)-keV γ-transitions. They agree with each other within the errors of one standard deviation for both γ-transitions. On the other hand, 30.88(4)- and 211.3(1)-keV transitions in FIG. 4.3 could not be identified in our measurement because of their low statistics due to low detection efficiency for 30.88(4)-keV and low γ-transition intensity for 211.3(1)-keV. The study of the 98.5(2)-keV and 130(1)-keV γ-rays in terms of statistics supports that they belong to the β-delayed γ-transitions of ^{195g}Ir.

Table 4.2 Comparison of the number of detected γ-rays (N_γ^{det}) and the calculated numbers of γ-ray detection (N_γ^{cal}) for 98.5- and 130-keV γ-transitions.

E_γ (keV)	N_γ^{det}	N_γ^{cal}
98.5(2)	15(5)	11(4)
130(1)	5(3)	2(1)

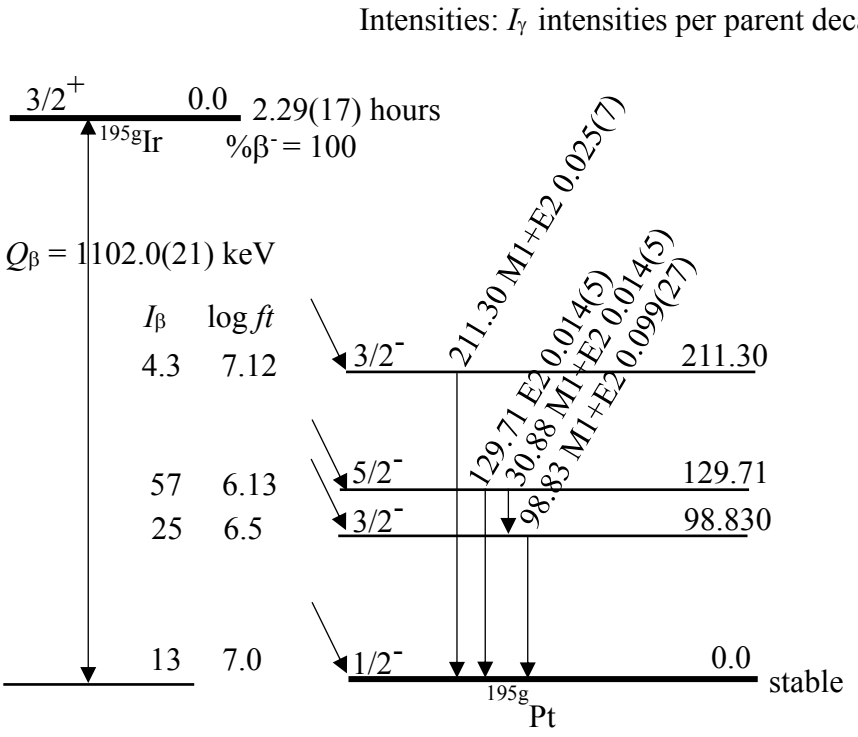

FIG. 4.2 β-decay scheme of ^{195g}Ir [50].

4.3 Half-life systematics of Os isotopes

FIG 4.3 shows the comparison of half-lives of Os isotopes among experimental data and theoretical predictions. The red circles indicate the experimental data measured at the KISS [49], together with presently obtained one of ^{195g}Os. The black circles indicate other experimental data [14]. The half-life of ^{195g}Os measured in this work, 6.5(4) minutes, agrees with previously measured value, 6.5(11) minutes. Two experimental values of half-lives of ^{196}Os are also in good agreement with each other. However, there is a discrepancy between two experimental data for ^{197}Os [49].

FIG. 4.3 also shows three theoretical predictions: the generalized energy density-functional method with continuum quasiparticle random-phase approximation (DF3) model [13], the gross theory with KTUY mass model [10] and the finite-range droplet model (FRDM) [11]. The measured half-lives of ^{195g}Os, ^{199g}Os and ^{200g}Os are reproduced by the DF3 model. The FRDM gives the closest value for the ^{196g}Os compared to the other theoretical models. For the two different experimental half-lives of ^{197g}Os, one is reproduced by the

FRDM and the other is reproduced by the KTUY model. The experimental value of ^{198g}Os is reproduced by the KTUY model.

Thus, the systematic trend of the Os β-decay half-lives is not reproduced by any single model. The experimental data of the β-decay half-lives of the Os isotopes would help to improve the theoretical evaluations of FF transitions around N = 126 nuclei.

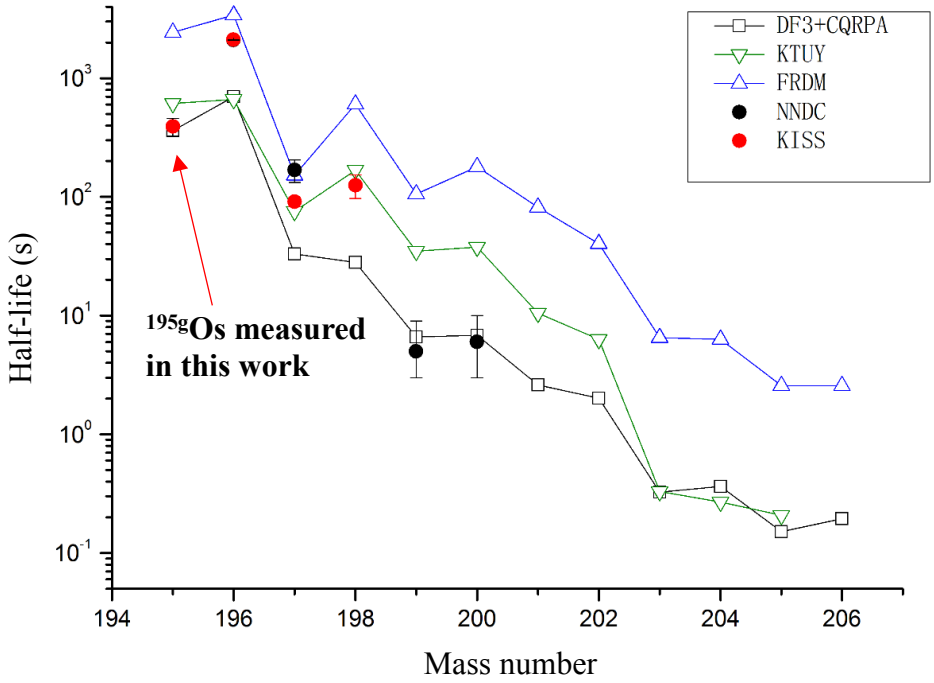

FIG. 4.3 Comparison of half-lives of Os isotopes among experimental data and theoretical predictions.

4.4 Nuclear structure of ^{195}Os

FIG. 4.4 shows the Nilsson diagram for neutrons of ^{195}Os calculated by [60]. All deformation parameters except for quadrupole deformation are assumed to be zero. The solid and dotted lines indicate the even- and odd-parity single particle states, respectively. When the nucleus deforms, the $\nu 13/2^+$ and $\nu 3/2^-$ states are expected to be close in energy. Weakly deformed oblate shapes are predicted for $^{197\text{-}199}$Os by theoretical calculations [61], and the ground state of ^{195}Os with the neutron number of 119 is assumed to have the spin-parity of $3/2^-$, which is consistent with our experiment results. A low-lying $13/2^+$ isomer is expected at more deformed oblate shape. M. W. Reed *at el.* reported

experimental results using the ESR at GSI for such possible isomeric state at the energy of 454(10) keV [20]. They suggested the half-life longer than 9 minutes for the isomeric state of $^{196}Os^{76+}$ from two events; one ion decayed to the ground state and the other was lost from the storage ring. Our experimental results suggest the isomeric state at the energy of 427.8(3) keV with the half-life of 47(3) s in the direct measurements of cascaded γ-rays in coincidence with X-rays detected by the MSPGC. Therefore our measured half-life is plausible for the isomeric state of neutral ^{195}Os atom. More experimental studies to identify the spin-parity of the isomeric state is desired for further investigation of the nuclear structure of ^{195}Os.

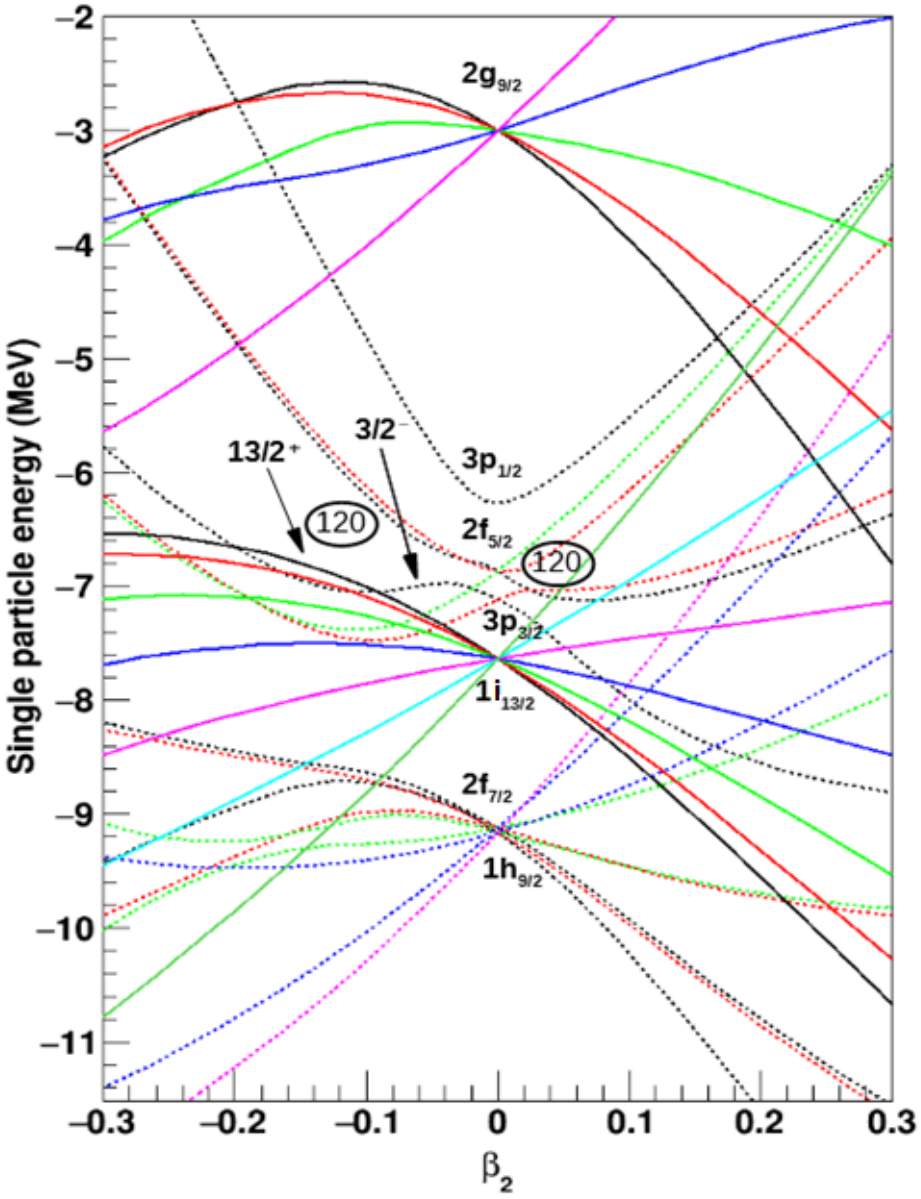

FIG. 4.4 Nilsson diagram for neutrons of ^{195}Os calculated by [60]. The solid and dotted lines indicate the even and odd parity states, respectively.

5 Summary

The ^{195}Os was produced through multi-nucleon transfer (MNT) reactions of the ^{136}Xe beam (9.4 MeV/nucleon) and the ^{198}Pt target (12.5 mg/cm^2) at the KEK isotope separation system (KISS). The element of osmium is selected by the laser resonance ionization and its mass number is separated by analyzing the dipole magnetic field. The radioactive isotope of ^{195}Os was transported to the β-γ detection station and was implanted into the aluminized Mylar tape. We used the pulsed beam of ^{195}Os for the measurement of lifetime and to remove the residual activities.

We observed X-ray peaks of osmium, iridium and platinum together with 28 γ-ray peaks. The energies of 20 γ-transitions agree with the literature values reported in the ^{194}Ir(n, γ)^{195}Ir experiments. The energies of 2 γ-ray peaks (98.5(2) and 130(1) keV) agree with the literature values of β-delayed γ-transitions of ^{195g}Ir. Another 6 γ-ray peaks are newly found γ-transitions. Two γ-ray peaks with the energies of 305.1(3) and 776.2(4) keV are identified as β-delayed γ-rays of ^{195}Os by their lifetime and γ-γ coincidence analysis. They were assigned in the previously reported level scheme of ^{195}Ir. Four γ-ray transitions with the energies of 111.0(1), 148.8(2), 168.8(2) and 279.0(1) keV were found to be associated with an isomeric state decay of ^{195}Os by their lifetime and γ-γ coincidence analyses. The evaluated half-life of this unknown isomeric state is 47(3) s, and a possible level scheme of ^{195}Os was proposed.

The β-decay scheme of ^{195}Os was studied. We evaluated the half-life of ^{195g}Os to be 6.5(4) minutes, which agrees with the previous literature value 6.5(11) minutes with the improved precision. The β-decay branching ratios of ^{195g}Os were evaluated and the log *ft* values of β-decay channels were obtained. Those log *ft* values range from 5.98(4) to 7.63(26), indicating all β-decay channels are the first-forbidden non-unique transitions. It is suggested that the spin-parity of ^{195g}Os would be $3/2^-$. It is consistent with prediction from the systematics.

The measured β-decay lifetime of ^{195g}Os were compared with several theoretical predictions. It is reproduced by the DF3 model [11]. However, the systematic trend of half-lives for osmium isotopes does not agree with any single models. The experimental data of the β-decay half-lives of the Os isotopes would help to improve the theoretical evaluations of FF transitions around N = 126 nuclei.

Appendix

A1 Fitting time spectrum in Section 4.1.2

The solution of the differential equations (4.5) is

$$\left.\begin{aligned} N_{\mathrm{m}}(t) &= \begin{cases} A_m^{on} e^{-\lambda_m t} + B_m^{on}, & (0 \le t \le T_{\mathrm{on}}) \\ A_m^{off} e^{-\lambda_m (t - T_{\mathrm{on}})} + B_m^{off}, & (T_{\mathrm{on}} \le t \le T_{\mathrm{on}} + T_{\mathrm{off}}) \end{cases} \\ N_{\mathrm{Os}}(t) &= \begin{cases} A_{Os}^{on} e^{-\lambda_m t} + B_{Os}^{on} e^{-\lambda_{Os} t} + C_{Os}^{on}, & (0 \le t \le T_{\mathrm{on}}) \\ A_{Os}^{off} e^{-\lambda_m (t - T_{on})} + B_{Os}^{off} e^{-\lambda_{Os} (t - T_{on})} + C_{Os}^{off}, & (T_{\mathrm{on}} \le t \le T_{\mathrm{on}} + T_{\mathrm{off}}) \end{cases} \\ N_{\mathrm{Ir}}(t) &= \begin{cases} A_{Ir}^{on} e^{-\lambda_m t} + B_{Ir}^{on} e^{-\lambda_{Os} t} + C_{Ir}^{on} e^{-\lambda_{Ir} t} + D_{Ir}^{on}, & (0 \le t \le T_{\mathrm{on}}) \\ A_{Ir}^{off} e^{-\lambda_m (t - T_{on})} + B_{Ir}^{off} e^{-\lambda_{Os} (t - T_{on})} + C_{Ir}^{off} e^{-\lambda_{Ir} (t - T_{on})} + D_{Ir}^{off}, & (T_{\mathrm{on}} \le t \le T_{\mathrm{on}} + T_{\mathrm{off}}) \end{cases} \end{aligned}\right\}, .. (4.6)$$

where

$A_m^{on} = -\frac{I_m}{\lambda_m}$; $B_m^{on} = \frac{I_m}{\lambda_m}$; $A_m^{off} = \frac{I_m}{\lambda_m}\left(1 - e^{-\lambda_m T_{\mathrm{on}}}\right)$; $B_m^{off} = 0$;
$A_{Os}^{on} = \frac{I_m}{\lambda_m - \lambda_{Os}}$; $A_{Os}^{off} = \frac{I_m}{(\lambda_{Os} - \lambda_m)}\left(1 - e^{-\lambda_m T_{\mathrm{on}}}\right)$; $B_{Os}^{on} = \frac{I_m}{\lambda_{Os} - \lambda_m} - \frac{I_m + I_{Os}}{\lambda_{Os}}$;
$B_{Os}^{off} = \left[\frac{I_m}{(\lambda_{Os} - \lambda_m)} - \frac{(I_m + I_{Os})}{\lambda_{Os}}\right][e^{-\lambda_{Os} T_{on}} - 1]$; $C_{Os}^{on} = \frac{I_m + I_{Os}}{\lambda_{Os}}$; $C_{Os}^{off} = 0$;
$A_{Ir}^{on} = \frac{\lambda_{Os} I_m}{(\lambda_{Ir} - \lambda_m)(\lambda_m - \lambda_{Os})}$; $A_{Ir}^{off} = \frac{\lambda_{Os} I_m\left(1 - e^{-\lambda_m T_{\mathrm{on}}}\right)}{(\lambda_{Ir} - \lambda_m)(\lambda_{Os} - \lambda_m)}$; $B_{Ir}^{on} = \frac{\lambda_{Os} I_m}{(\lambda_{Ir} - \lambda_{Os})(\lambda_{Os} - \lambda_m)} - \frac{(I_m + I_{Os})}{(\lambda_{Ir} - \lambda_{Os})}$; $B_{Ir}^{off} = \left[\frac{\lambda_{Os} I_m}{(\lambda_{Ir} - \lambda_{Os})(\lambda_{Os} - \lambda_m)} - \frac{(I_m + I_{Os})}{(\lambda_{Ir} - \lambda_{Os})}\right][e^{-\lambda_{Os} T_{\mathrm{on}}} - 1]$;
$C_{Ir}^{on} = \frac{-\lambda_{Os} I_m}{(\lambda_{Ir} - \lambda_m)(\lambda_m - \lambda_{Os})} - \frac{\lambda_{Os} I_m}{(\lambda_{Ir} - \lambda_{Os})(\lambda_{Os} - \lambda_m)} + \frac{I_m + I_{Os}}{(\lambda_{Ir} - \lambda_{Os})} - \frac{I_m + I_{Os}}{\lambda_{Ir}}$;
$C_{Ir}^{off} = [e^{-\lambda_{Os} T_{\mathrm{on}}} - e^{-\lambda_{Ir} T_{\mathrm{on}}}]\left[\frac{\lambda_{Os} I_m}{(\lambda_{Ir} - \lambda_{Os})(\lambda_{Os} - \lambda_m)} - \frac{(I_m + I_{Os})}{(\lambda_{Ir} - \lambda_{Os})}\right] + (e^{-\lambda_{Ir} T_{on}} - 1) \times [\frac{\lambda_{Os} I_m}{(\lambda_{Ir} - \lambda_{Os})(\lambda_{Os} - \lambda_m)} - \frac{\lambda_{Os} I_m}{(\lambda_{Ir} - \lambda_m)(\lambda_m - \lambda_{Os})} - \frac{(I_m + I_{Os})}{(\lambda_{Ir} - \lambda_{Os})} - \frac{(I_m + I_{Os})}{\lambda_{Ir}}]$;
$D_{Ir}^{on} = \frac{I_m + I_{Os}}{\lambda_{Ir}}$; $D_{Ir}^{off} = 0$.

N_i^{cal} in equation (4.6) is decomposed as,

$$\begin{aligned} N_i^{cal} &= C_N \times \int_{t_i^{\mathrm{l}}}^{t_i^{\mathrm{u}}} f(t)\, dt \\ &= N_{m_i}^{cal} + N_{Os_i}^{cal} + N_{Ir_i}^{cal} + N_{B.G_i}^{cal}, \end{aligned}$$

where

$$\begin{aligned} N_{m_i}^{cal} &= C_N \times \int_{t_i^{\mathrm{l}}}^{t_i^{\mathrm{u}}} \varepsilon_m \lambda_m N_m(t)\, dt, \\ N_{Os_i}^{cal} &= C_N \times \int_{t_i^{\mathrm{l}}}^{t_i^{\mathrm{u}}} \varepsilon_{Os} \lambda_{Os} N_{Os}(t)\, dt, \\ N_{Ir_i}^{cal} &= C_N \times \int_{t_i^{\mathrm{l}}}^{t_i^{\mathrm{u}}} \varepsilon_{Ir} \lambda_{Ir} N_{Ir}(t)\, dt, \\ N_{B.G_i}^{cal} &= C_N \times R_{B.G}. \end{aligned}$$

$N_{m_i}^{cal}$, $N_{Os_i}^{cal}$ and $N_{Ir_i}^{cal}$ are calculated as,

$$N_{m_i}^{cal} = C_N \times \begin{cases} \frac{\varepsilon_m I_R I_{Os}}{\lambda_m}(1 - e^{\lambda_m \Delta t_{bin}})e^{-\lambda_m \Delta t_{bin}\, i} + \varepsilon_m I_R I_{Os} \Delta t_{bin}\,, \\ (0 \le t_i^u \le T_{on}); \\ \frac{\varepsilon_m I_R I_{Os}}{\lambda_m}(1 - e^{-\lambda_m T_{on}})(e^{\lambda_m \Delta t_{bin}} - 1)e^{-\lambda_m(\Delta t_{bin}\, i - T_{on})}\,, \\ \left(T_{on} \le t_i^l \le T_{on} + T_{off}\right); \\ \varepsilon_m I_R I_{Os}(T_{on} - \Delta t_{bin}(i-1)) + \frac{\varepsilon_m I_R I_{Os}}{\lambda_m}\left(1 - e^{-\lambda_m T_{on}}\right)[1 - e^{-\lambda_m(\Delta t_{bin} i - T_{on})}], \quad \left(t_i^l \le T_{on} \le t_i^u\right); \end{cases} \quad \ldots(4.7)$$

$$N_{Os_i}^{cal} = C_N \times \begin{cases} \frac{\lambda_{Os}\varepsilon_{Os} I_R I_{Os}}{\lambda_m(\lambda_{Os} - \lambda_m)}(e^{-\lambda_m \Delta t_{bin} i}(1 - e^{\lambda_m \Delta t_{bin}})) + \varepsilon_{Os}[\frac{(I_R+1)I_{Os}}{\lambda_{Os}} - \frac{I_R I_{Os}}{(\lambda_{Os} - \lambda_m)}] \\ (1 - e^{\lambda_{Os}\Delta t_{bin}})e^{-\lambda_{Os}\Delta t_{bin} i} + (I_R I_{os} + I_{Os})\Delta t_{bin}\, \varepsilon_{Os}\,, (0 \le \\ t_i^u \le T_{on}); \\ \frac{\lambda_{Os}\varepsilon_{Os}}{(\lambda_m - \lambda_{Os})}\frac{I_{os} I_R}{\lambda_m}(1 - e^{-\lambda_m T_{on}})(e^{-\lambda_m(\Delta t_{bin} i - T_{on})}(1 - e^{\lambda_m \Delta t_{bin}})) + \\ \varepsilon_{Os}[\frac{\lambda_m}{(\lambda_{Os} - \lambda_m)}\frac{I_{os} I_R}{\lambda_m}(1 - e^{-\lambda_m T_{on}}) - \frac{I_{Os} I_R}{\lambda_m - \lambda_{Os}}\left(e^{-\lambda_m T_{on}}\right) + \\ \left[\frac{I_{Os} I_R}{\lambda_{Os} - \lambda_m} - \frac{I_{Os} I_R + I_{Os}}{\lambda_{Os}}\right]\left(e^{-\lambda_{Os} T_{on}}\right) + \frac{I_{Os} I_R + I_{Os}}{\lambda_{Os}}] (1 - \\ e^{\lambda_{Os}\Delta t_{bin}})e^{-\lambda_{Os}(\Delta t_{bin} i - T_{on})}, \quad \left(T_{on} \le t_i^l \le T_{on} + T_{off}\right); \\ \frac{\lambda_{Os}\varepsilon_{Os} I_R I_{os}}{\lambda_m(\lambda_{Os} - \lambda_m)}(e^{-\lambda_m T_{on}} - e^{-\lambda_m \Delta t_{bin}(i-1)}) + \varepsilon_{Os}[\frac{(I_R I_{os} + I_{Os})}{\lambda_{Os}} - \\ \frac{I_R I_{Os}}{(\lambda_{Os} - \lambda_m)}] (e^{-\lambda_{Os} T_{on}} - e^{-\lambda_{Os}\Delta t_{bin}(i-1)}) + (I_R I_{os} + I_{Os})\varepsilon_{Os}[T_{on} - \\ \Delta t_{bin}(i-1)] + \frac{\lambda_{Os}\varepsilon_{Os}}{(\lambda_m - \lambda_{Os})}\frac{I_{os} I_R}{\lambda_m}(1 - e^{-\lambda_m T_{on}})\left(e^{-\lambda_m(\Delta t_{bin} i - T_{on})} - 1\right) + \\ \varepsilon_{Os}[\frac{\lambda_m}{(\lambda_{Os} - \lambda_m)}\frac{I_{os} I_R}{\lambda_m}(1 - e^{-\lambda_m T_{on}}) - \frac{I_{Os} I_R}{\lambda_m - \lambda_{Os}}\left(e^{-\lambda_m T_{on}}\right) + \\ \left[\frac{I_{Os} I_R}{\lambda_{Os} - \lambda_m} - \frac{I_{Os} I_R + I_{Os}}{\lambda_{Os}}\right]\left(e^{-\lambda_{Os} T_{on}}\right) + \frac{I_{Os} I_R + I_{Os}}{\lambda_{Os}}\,](e^{-\lambda_{Os}(\Delta t_{bin} i - T_{on})} - 1), \\ \left(t_i^l \le T_{on} \le t_i^u\right); \end{cases} \quad \ldots(4.8)$$

$$N_{Ir_i}^{cal} = C_N \times \begin{cases} \frac{\lambda_{Os} I_R I_{Os} \varepsilon_{Ir} \lambda_{Ir}}{\lambda_m(\lambda_m-\lambda_{Ir})(\lambda_m-\lambda_{Os})}\left(e^{-\lambda_m \Delta t_{bin}\, i}(1-e^{\lambda_m \Delta t_{bin}})\right) + \frac{\varepsilon_{Ir}\lambda_{Ir}}{\lambda_{Os}}\left[\frac{(I_R I_{Os}+I_{Os})}{(\lambda_{Ir}-\lambda_{Os})} - \frac{\lambda_{Os} I_R I_{Os}}{(\lambda_{Ir}-\lambda_{Os})(\lambda_{Os}-\lambda_m)}\right](1-e^{\lambda_{Os}\Delta t_{bin}})e^{-\lambda_{Os}\Delta t_{bin} i} + \varepsilon_{Ir}\left[\frac{\lambda_{Os} I_R I_{Os}}{(\lambda_{Ir}-\lambda_m)(\lambda_m-\lambda_{Os})} + \frac{\lambda_{Os} I_R I_{Os}}{(\lambda_{Ir}-\lambda_{Os})(\lambda_{Os}-\lambda_m)} - \frac{(I_R I_{Os}+I_{Os})}{(\lambda_{Ir}-\lambda_{Os})} + \frac{(I_R I_{Os}+I_{Os})}{\lambda_{Ir}}\right](1-e^{\lambda_{Ir}\Delta t_{bin}})e^{-\lambda_{Ir}\Delta t_{bin} i} + (I_R I_{Os} + I_{Os})\varepsilon_{Ir}\,\Delta t_{bin}, \quad (0 \le t_i^u \le T_{on}); \\ \left(\frac{\lambda_{Os}\varepsilon_{Ir}\lambda_{Ir}\left(\frac{I_R I_{os}\left(1-e^{(-\lambda_m T_{on})}\right)}{\lambda_m}\right)\left(e^{(-\lambda_m(\Delta t_{bin}\, i-T_{on}))} - e^{(-\lambda_m(\Delta t_{bin}(i-1)-T_{on}))}\right)}{(\lambda_m-\lambda_{Ir})(\lambda_{Os}-\lambda_m)}\right) + \frac{1}{\lambda_{Os}-\lambda_m}\varepsilon_{Ir}\lambda_{Ir}\left(\left(\left(\frac{I_{Os} I_R e^{(-\lambda_m T_{on})}}{\lambda_m-\lambda_{Os}} + \left(\frac{I_{Os} I_R}{\lambda_{Os}-\lambda_m} - \frac{I_{Os} I_R + I_{Os}}{\lambda_{Os}}\right)e^{(-\lambda_{Os} T_{on})} + \frac{I_{Os} I_R + I_{Os}}{\lambda_{Os}}\right) - \left(\frac{I_{os} I_R\left(1-e^{(-\lambda_m T_{on})}\right)}{\lambda_{Os}-\lambda_m}\right)\right) \\ \times \frac{\lambda_{Os}\varepsilon_{Ir}\lambda_{Ir}\left(\frac{I_R I_{os}\left(1-e^{(-\lambda_m T_{on})}\right)}{\lambda_m}\right)\left(e^{(-\lambda_m(\Delta t_{bin}\, i-T_{on}))} - e^{(-\lambda_m(\Delta t_{bin}(i-1)-T_{on}))}\right)}{(\lambda_m-\lambda_{Ir})(\lambda_{Os}-\lambda_m)} \times \\ \left(e^{(-\lambda_{Os}\Delta t_{bin}\, i)}e^{(\lambda_{Os} T_0)}\left(1-e^{(-\lambda_{Os}\Delta t_{bin})}\right)\right) + \left(-\varepsilon_{Ir}\left(e^{(-\lambda_{Ir}(\Delta t_{bin} i-T_{on}))} - e^{(-\lambda_{Ir}(\Delta t_{bin}(i-1)-T_{on}))}\right)\right)\left(\left(\left(\frac{\lambda_{Os} I_{Os} I_R\left(1-e^{(-\lambda_m T_{on})}\right)}{((\lambda_{Ir}-\lambda_m)(\lambda_m-\lambda_{Os})}\right)\right) + \left(\left(\left(\frac{\lambda_{Os} I_{Os} I_R}{(\lambda_{Ir}-\lambda_{Os})(\lambda_{Os}-\lambda_m)}\right) - \left(\frac{I_{Os} I_R + I_{Os}}{\lambda_{Ir}-\lambda_{Os}}\right)e^{(-\lambda_{Os} T_{on})}\right) + \left(\left(\left(-\frac{\lambda_{Os} I_{Os} I_R}{(\lambda_{Ir}-\lambda_m)(\lambda_m-\lambda_{Os})}\right) - \left(\frac{\lambda_{Os} I_{Os} I_R}{(\lambda_{Ir}-\lambda_{Os})(\lambda_{Os}-\lambda_m)}\right) + \left(\frac{I_{Os} I_R + I_{Os}}{\lambda_{Ir}-\lambda_{Os}}\right) - \left(\frac{I_{Os} I_R + I_{Os}}{\lambda_{Ir}}\right)\right)e^{(-\lambda_{Ir} T_{on})}\right) + \frac{I_{Os} I_R + I_{Os}}{\lambda_{Ir}}\right) - \left(\frac{\lambda_{Os}\left(I_{Os} I_R\left(1-e^{(-\lambda_m T_{on})}\right)\right)}{(\lambda_{Ir}-\lambda_m)(\lambda_{Os}-\lambda_m)}\right) - \left(\left(\frac{\lambda_{Os}}{\lambda_{Ir}-\lambda_{Os}} \times \left(\left(\left(\frac{I_{Os} I_R e^{(-\lambda_m T_{on})}}{\lambda_m-\lambda_{Os}} + \left(\frac{I_{Os} I_R}{\lambda_{Os}-\lambda_m} - \frac{I_{Os} I_R + I_{Os}}{\lambda_{Os}}\right)e^{(-\lambda_{Os} T_{on})} + \frac{I_{Os} I_R + I_{Os}}{\lambda_{Os}}\right) - \left(\frac{\left(I_{Os} I_R\left(1-e^{(-\lambda_m T_{on})}\right)\right)}{\lambda_{Os}-\lambda_m}\right)\right)\right)\right)\right), \left(T_{on} \le t_i^l \le T_{on} + T_{off}\right); \\ \frac{\lambda_{Os} I_R I_{Os} \varepsilon_{Ir} \lambda_{Ir}}{\lambda_m(\lambda_m-\lambda_{Ir})(\lambda_m-\lambda_{Os})}\left(e^{-\lambda_m T_{on}} - e^{-\lambda_m \Delta t_{bin}(i-1)}\right) + \frac{\varepsilon_{Ir}\lambda_{Ir}}{\lambda_{Os}}\left(\frac{(I_R I_{Os}+I_{Os})}{(\lambda_{Ir}-\lambda_{Os})} - \frac{\lambda_{Os} I_R I_{Os}}{(\lambda_{Ir}-\lambda_{Os})(\lambda_{Os}-\lambda_m)}\right)\left(e^{-\lambda_{Os} T_{on}} - e^{-\lambda_{Os}\Delta t_{bin}(i-1)}\right) + \varepsilon_{Ir}\left(\frac{\lambda_{Os} I_R I_{Os}}{(\lambda_{Ir}-\lambda_m)(\lambda_m-\lambda_{Os})} + \frac{\lambda_{Os} I_R I_{Os}}{(\lambda_{Ir}-\lambda_{Os})(\lambda_{Os}-\lambda_m)} - \frac{(I_R I_{Os}+I_{Os})}{(\lambda_{Ir}-\lambda_{Os})} + \frac{(I_R I_{Os}+I_{Os})}{\lambda_{Ir}}\right)\left(e^{-\lambda_{Ir} T_{on}} - e^{-\lambda_{Ir}\Delta t_{bin}(i-1)}\right) + (I_R I_{Os} + I_{Os})(T_{on} - \Delta t_{bin}(i-1)\varepsilon_{Ir} + \end{cases} \quad \ldots(4.9)$$

$$\left\{\begin{array}{l}\frac{\varepsilon_{Ir}\lambda_{Ir}\lambda_{Os}I_R I_{Os}(e^{(-\lambda_m(\Delta t_{bin}i-T_{on}))}-1)(1-e^{(-\lambda_m T_{on})})}{\lambda_m(\lambda_m-\lambda_{Ir})(\lambda_{Os}-\lambda_m)}+\varepsilon_{Ir}\lambda_{Ir}(e^{(-\lambda_{Os}(\Delta t_{bin}i-T_{on}))}- \\ 1)(((I_R I_{Os}(e^{(-\lambda_m T_{on})}/(\lambda_m-\lambda_{Os})+(I_R I_{Os}/(\lambda_{Os}-\lambda_m)-(I_R I_{Os}+ \\ I_{Os})/\lambda_{Os})\,e^{(-\lambda_m T_{on})}+(I_R I_{Os}+I_{Os})/\lambda_{Os}))-(\lambda_m((I_R I_{Os}(1- \\ e^{(-\lambda_m T_{on})})/\lambda_m))/(\lambda_{Os}-\lambda_m)))/(\lambda_{Os}-\lambda_{Ir})-\varepsilon_{Ir}(e^{(-\lambda_{Ir}(\Delta t_{bin}i-T_{on}))}- \\ 1)(((\lambda_{Os}I_R I_{Os}e^{(-\lambda_m T_{on})}/((\lambda_{Ir}-\lambda_m)(\lambda_m-\lambda_{Os})))+\ (((\lambda_{Os}I_R I_{Os}/(\lambda_{Ir}- \\ \lambda_{Os})(\lambda_{Os}-\lambda_m))-((I_R I_{Os}+I_{Os})/(\lambda_{Ir}-\lambda_{Os})))e^{(-\lambda_{Os}T_{on})})+ \\ (((-\lambda_{Os}I_R I_{Os}/(\lambda_{Ir}-\lambda_m)(\lambda_m-\lambda_{Os}))-(\lambda_{Os}I_R I_{Os}/(\lambda_{Ir}-\lambda_{Os})(\lambda_{Os}- \\ \lambda_m))+((I_R I_{Os}+I_{Os})/(\lambda_{Ir}-\lambda_{Os}))-((I_R I_{Os}+I_{Os})/\lambda_{Ir}))e^{(-\lambda_{Ir}T_{on})})+ \\ (I_R I_{Os}+I_{Os})/\lambda_{Ir})-(\lambda_{Os}\lambda_m((I_R I_{Os}(1-e^{(-\lambda_m T_{on})})/\lambda_m))/(\lambda_{Ir}- \\ \lambda_m)(\lambda_{Os}-\lambda_m))-(\lambda_{Os}/(\lambda_{Ir}-\lambda_{Os})(((I_R I_{Os}e^{(-\lambda_m T_{on})}/(\lambda_m-\lambda_{Os})+ \\ (I_R I_{Os}/(\lambda_{Os}-\lambda_m)-(I_R I_{Os}+I_{Os})/\lambda_{Os})e^{(-\lambda_{Os}T_{on})}+(I_R I_{Os}+ \\ I_{Os})/\lambda_{Os}))-(\lambda_m)((I_R I_{Os}(1-e^{(-\lambda_m T_{on})}))/\lambda_m))/(\lambda_{Os}-\lambda_m)))),\ \ \left(t_i^l \le \right. \\ \left. T_{on} \le t_i^u\right);\end{array}\right.$$

References

[1] E. M. Burbidge et al., *Rev. Mod. Phys.,* **29** (1957) 547

[2] B. Pfeiffer et al., *Nucl. Phys.,* **A 693** (2001) 282

[3] K.-L. Kratz et al., *Astrophys. J.,* **403** (1993) 216

[4] J. J. Cowan et al., *Phys. Today*, (2004) 47

[5] J. M. Pearson et al., *Phys. Lett.*, **B 387** (1996) 455

[6] P. Möller et al., *At. Data Nucl. Data Tables,* **109-10** (2016) 1

[7] H. Grawe et al., *Rep. Prog. Phys.,* **70** (2007) 1525

[8] P. A. Seeger et al., *Astrophys. J. suppl.,* **11** (1965) 121

[9] I. N. Borzov, *Nucl. Phys.,* **A 777** (2006) 645

[10] H. Koura et al., *Prog. Theor. Phys.*, **113** (2005) 305

[11] P. Möller et al., *Phys. Rev.,* **C 67** (2003) 055802

[12] T. Suzuki et al., *Phys. Rev.,* **C 85** (2012) 015802

[13] I. N. Borzov, *Phys. At. Nucl.,* **74** (2011) 1435

[14] https://www.nndc.bnl.gov/

[15] M. Mumpower et al., *AIP ADVANCES,* **4** (2014) 041009

[16] G. B. Baro et al., *Z. Naturforsch.,* **A 12** (1957) 520

[17] J. J. Valiente-Dobon et al., *Phys. Rev.,* **C 69** (2004) 024316

[18] M. Caamano et al., *Eur. Phys. J.,* **A 23** (2005) 201

[19] S. J. Steer et al., *Phys. Rev.,* **C 84** (2011) 044313

[20] M. W. Reed et al., *Phys. Rev.,* **C 86** (2012) 054321

[21] R. B. Firestone and V. S. Shirley, *Table of Isotopes 8th ed.*, John Wiley and Sons, Inc. New York (1996)

[22] E. Browne and R. B. Firestone, *Table of Radioactive Isotopes,* John Wiley and Sons, Inc. New York (1986)

[23] C. Zhou, *Nucl. Data Sheets,* **86** (1999) 645

[24] J. W. Arblaster, *Platinum Met. Rev.,* **48** (2004) 173

[25] R. Robinson and M. Thoennessen, *At. Data Nucl. Data Tables,* **98** (2012) 911

[26] G. Audi et al., *Chinese Phys.*, **C 36** (2012) 1157

[27] K. Takahashi et al., *At. Data Nucl. Data Tables,* **12** (1973) 101

[28] M. Birch et al., *Phys. Rev.*, **C 88** (2013) 067301

[29] J. F. W. Jansen et al., *Z. Phys.,* **261** (1973) 95

[30] T. Kubo, *Nucl. Instrum. and Meth.*, **B 204** (2003) 97

[31] H. Geissel et al., *Nucl. Instrum. and Meth.,* **B 70** (1992) 286

[32] Y. X. Watanabe et al., *Phys. Rev. Lett.,* **115** (2015)172503

[33] T. Kurtukian-Nieto et al., *Phys. Rev.,* **C 89** (2014) 024616

[34] A. Winther, *Nucl. Phys.*, **A 572** (1994)191

[35] A. Winther, *Nucl. Phys.*, **A 594** (1995) 203

[36] http:/www.to.infn.it/~nanni/grazing/

[37] Y. Hirayama et al., *Nucl. Instrum. and Meth.*, **B 412** (2017) 11

[38] D. Kaji and K. Morimoto, *Nucl. Phys.*, **A 792** (2015) 11

[39] Y. Hirayama et al., *Nucl. Instrum. Meth.,* **B 353** (2015) 4

[40] H. Haba et al., *J. Nucl. Radiochem. Sci.,* **8** (2007) 55

[41] Y. Hirayama et al., *J. Phys. B: At. Mol. Opt. Opt. Phys.*, **50** (2017) 215203

[42] P. Colarusso et al., *Phys. Rev.,* **A 55** (1997) 1526

[43] P. Quinet et al., *Astron. Astrophys.,* **448** (2006) 1207

[44] M. Mukai et al., *Nucl. Instrum. and Meth.*, **A 884** (2018) 1

[45] J.-P. Martin et al., *IEEE Trans. Nucl. Sci.*, **55** (2008) 84

[46] U. Rizwan et al., *Nucl. Instrum. and Meth.*, **A 820** (2016) 126

[47] P. K. Joshi et al., *Nucl. Instrum. and Meth.,* **A 399** (1997) 51

[48] S. Hurtado et al., *Nucl. Instrum. and Meth.*, **A 594** (2008) 362

[49] Y. Hirayama et al., *Phys. Rev.,* **C 98** (2018) 014321

[50] H. Xiaolong and K. Mengxiao, *Nucl. Data Sheets,* **121** (2014) 395

[51] G. G. Colvin et al., *Nucl. Phys.,* **A 465** (1987) 240

[52] T. Kibédi et al., *Nucl. Instrum. and Meth.*, **A 589** (2008) 202

[53] N. B. Gove and M. J. Martin, *Nucl. Data Tables*, **10** (1971) 205

[54] Zs. Podolyák et al., *J. of Phys: Conf. Ser.*, **381** (2012) 012052

[55] C. Wheldon et al., *Phys. Rev.*, **C 63** (2000) 011304

[56] O. L. Caballero et al., *arXiv:1405.0210[nucl-th]*

[57] https://midas.triumf.ca/MidasWiki/index.php/Midas_documentation

[58] K. Heyde, *Basic Ideas and Concepts in Nuclear Physics, 2nd ed.*, (1994) 139

[59] https://root.cern.ch/sites/d35c7d8c.web.cern.ch/files/minuit.pdf

[60] S. Cwiok et al., *Comput Phys. Commun.* **46** (1987) 376

[61] L. M. Robledo et al., *J. Phys. G: Nucl. Part. Phys.* **36** (2009) 115104

Acknowledgements

I humbly render my heartfelt gratitude to Prof. Hiroari Miyatake, Dr. Yutaka Watanabe, Dr. Yoshikazu Hirayama and Prof. Akira Ozawa for their constant guidance and supervision throughout the work. Their continuous discussions, instructive suggestions and supports helps me to proceed this work. They teach me many treatments of experimental techniques, physics, writing the documents and making the presentations.

I am sincerely grateful to Dr. Yutaka Watanabe. This document would not have been possible without his assistance. I learned many treatments in the data acquisition systems, data analysis, making the analysis program, writing the documents and so on. He taught me each branch of my research work. His significant investments of time and efforts helps me to procced this work. Thanks for answering, often repeatedly many basic questions. Thanks again to Dr. Yoshikazu Hirayama for allowing me to use the experimental data.

I am also grateful to Prof. Michiharu Wada, Dr. Peter Schury, Dr. Tetsuaki Moriguchi, Dr. Kimikazu Sasa, Dr. Jinhyung Park and Dr. Junyoung Moon for their continuous help and valuable advice.

I would like to express my special thanks to Dr. Momo Mukai and Dr. Sota Kimura. They helped not only in academically but also personally.

I would like to offer my best thanks to Machiko Izawa for her continuous support. I would like to thank Dr. Hiroshi Watanabe, Mr. Yutaka Kakiguchi and Mr. Michihiro Oyaizu for their support.

I am also thankful to all staffs of KEK, RIKEN and past and present staffs and students belonging to the low-energy nuclear physics in University of Tsukuba.

I am deeply grateful to my former supervisor prof. Suranjan Kumar Das for his continuous suggestions and valuable advice. I would like to offer my best thanks to prof. Kamrul Alam Khan, prof. Dipika Rani Sarker, prof. Parimal Bala, Prof. Ain-Ul Huda, prof. Nure Alam Abdullah, Dr. Golam Mustafa for their instructive suggestions.

I also grateful to my parents and all other family members. Their support and blessing have made it possible to carry out this research work to completion.

I would like to express my special thanks to Japan Government to provide me Japanese Government (MEXT) scholarship.